The Florida State University
DigiNole Commons

Electronic Theses, Treatises and Dissertations

The Graduate School

8-6-2010

Energy Transfer in Bio-molecules - Mechanism, Validity and Applicability of Nano-metal Surface Energy Transfer

Mani Prabha Singh
Florida State University

Follow this and additional works at: http://diginole.lib.fsu.edu/etd

Recommended Citation

Singh, Mani Prabha, "Energy Transfer in Bio-molecules - Mechanism, Validity and Applicability of Nano-metal Surface Energy Transfer" (2010). *Electronic Theses, Treatises and Dissertations.* Paper 1705.

This Dissertation - Open Access is brought to you for free and open access by the The Graduate School at DigiNole Commons. It has been accepted for inclusion in Electronic Theses, Treatises and Dissertations by an authorized administrator of DigiNole Commons. For more information, please contact lib-ir@fsu.edu.

THE FLORIDA STATE UNIVERSITY

COLLEGE OF ARTS AND SCIENCES

ENERGY TRANSFER IN BIO-MOLECULES - MECHANISM, VALIDITY AND APPLICABILITY OF NANO-METAL SURFACE ENERGY TRANSFER

By

MANI PRABHA SINGH

A Dissertation submitted to the
Department of Chemistry and Biochemistry
in partial fulfillment of the
requirements for the degree of
Doctor of Philosophy

Degree Awarded:
Fall Semester, 2010

The members of the committee approve the dissertation of Mani Prabha Singh defended on August 06, 2010.

Prof. G.F. Strouse
Professor Directing Thesis

Prof. P.B. Chase
University Representative

Prof. A.E. Steigman
Committee Member

Prof. T.M. Logan
Committee Member

Approved:

Prof. J.B. Schlenoff, Chair, Department of Chemistry and Biochemistry

The Graduate School has verified and approved the above-named committee members.

For Mom and Dad

ACKNOWLEDGMENTS

I would like to thank my advisor Prof. G.F. Strouse without whom this would not have been possible. His invaluable guidance and knowledge is what has made this possible. If it wasn't for his patience and support I would not have been able to start or successfully complete this. I am also thankful to my committee members who were extremely cooperative.

My family has played a pivotal role in making me the person that I am today. Everything and anything that I will ever accomplish or achieve is because of them and for them. I am most grateful to my parents who always gave me the freedom to do what I wanted and the support whenever I faltered. My brother Ashish and sister Jyotsna have given me enough reasons to smile and laugh whenever the going got tough. I do not know how I would have done any of this without them. I am grateful to Ravi Singh for the good times and the patience with which he always listens.

Many of my friends have been very supportive all these years, especially Mridusmita Saikia, who is family away from home. I am most thankful to Parisa Mahjoor for always being there for me. I would not have made it through without those fun and relieveing, long chats. Punam Thakur is one person whom I truly admire for her perseverance. I am thankful to Nandita, Shruti, Smriti, Rupsa and Vani for being so very patient with me all the time. You girls are just amazing. I have had some my best times in Tallahassee with you all. I am grateful to Sonalika Vaidya for being there all these years.

I would like to thank the previous Strouse group members, especially Aaron Washington for always lending me a patient ear whenever I needed one. I miss not having you around and of course the dumplings and mojitos. I am grateful to Travis Jennings for very patiently teaching me everything. I am thankful to Donny Magana who never got tired of answering my questions. I am grateful to Weiwei, Qilin and Megan Foley for keeping the office always lively. I am also thankful to all the other Strouse group members, both past and present for their help and support.

I am also grateful to the staff at the Department of Chemistry and Biochemistry for all their patience and help.

- Mani

TABLE OF CONTENTS

LIST OF TABLES

LIST OF FIGURES

LIST OF SYMBOLS

A - scattering process dependent fitting parameter
$\overline{A}$ - absorptivity of mirror
$\mathbf{A}(\lambda)$ - field enhancement factor
C_6 - hexa-alkyl spacer
d - thickness of the film
E - quenching efficiency of energy transfer
E_g - energy gap between d and sp dispersion curves
$\mathbf{F}$ - Surface/Volume dependent damping term
$J(\lambda)$ - overlap integral
$\mathbf{K}$ - oscillator strength of interband transitions
k_{ET} - rate of energy transfer
k_F - Fermi wave vector for the metal
k_{nr} - rate of non-radiative decay of a fluorophore
k_r - rate of radiative decay of a fluorophore
L - modified separation distance in ds-DNA helix
l_∞, l - mean free path of electron in bulk metal
N_A - Avogadro's number
N_c - number of atoms in the core of a cluster
N_s - number of atoms on the surface of a cluster
ΔN - Number of bases separating two points on a ds-DNA
n - Energy transfer fitting parameter
$\overline{n}$ - complex refractive index of a metal, $\overline{n} = n_r + ik$
n_m - refractive index of medium
R - distance of separation between donor and acceptor
R_0 - critical distance of energy transfer
r - radius of a metal sphere
r_s - electron gas density parameter of the metal
V_0 - volume of the metal sphere
α - dipole orientation term in Kuhn theory
$\epsilon(\omega)$ - complex dielectric function of the metal, $\epsilon(\omega) = \epsilon_1(\omega) + i\epsilon_2(\omega)$
$\epsilon_1(\omega)$ - real component of the dielectric
$\epsilon_2(\omega)$ - imaginary component of the dielectric
$\epsilon(\omega, r)$ - size and frequency dependent complex dielectric function

ϵ^D, ϵ^{intra} - Conduction band (Drude-like) contributions to the dielectric function
ϵ^{IB}, ϵ^{inter} - Interband contributions to the dielectric function
ϵ_m - dielectric constant of the medium
Φ_{dye} - quantum yield of the dye
$\Gamma(r)$ - size dependent damping term for metal nanoparticles
$\Gamma(\rho)$ - width of lifetime distribution
Γ_∞ - Bulk damping term for a metal
γ_{ee} - interband damping rate
γ_{eff} - damping rate for the plasmon
η - enhancement factor
κ - orientation term in FRET
λ - wavelength of light
λ_{abs} - wavelength of absorption maximum of fluorophore
λ_{ex} - wavelength of excitation for a fluorophore
λ_{LSPR} - wavelenght of LSPR for metal nanoparticles
μ - dipole moment of a molecule
σ_{ext} - extinction cross section of a metal spehere
σ_{abs} - absorption cross section
σ_{sca} - scattering cross section
τ_{dye}, τ_0 - native lifetime of the dye
υ_F - Fermi velocity for the metal
ω - angular frequency of light
ω_{dye} - angular frequency of dye emission
ω_F - Fermi frequency of the metal
ω_p - plasma frequency of the metal
$\omega_{p,eff}$ - effective plasma frequency
ξ - cylinder base vector

LIST OF ABBREVIATIONS

A - acceptor
Au NM - Gold nanometal
Au NP - Gold nanoparticle
AF350 - AlexaFluor 350
AF488 - AlexaFluor 488
AF555 - AlexaFluor 555
AF594 - AlexaFluor 594
AF647 - AlexaFluor 647
AF700 - AlexaFluor 700
AF750 - AlexaFluor 750
BSPP - Bis(p-sulfonatophenyl)phenylphosphine
BRET - Bioluminescence Resonance Energy Transfer
bp - base pair
CB - Conduction band
CCB - Cascade Blue
CPS - Chance Prock Silbey
CRET - Chemiluminescence Resonance Energy Transfer
Cy3 - Cyanine3
Cy5 - Cyanine5
D - donor
DMPET - Dipole to Metal Particle Energy Transfer
DNA - Deoxyribonucleic acid
DTT - Dithiothreitol
ds - double strand
EPR - Electron Paramagnetic Resonance
FAM - Fluorescien
FRET - Fluorescence/Forster Resonance Energy Transfer
G-N - Gersten-Nitzan
IR - Infra red
LRET - Luminescence Resonance Energy Transfer
LSPR - Localized Surface Plasmon Resonance
MEM-NLLS - Maximum Entropy Method-Non linear Least Squares
MNP - Metal Nanoparticle
NMR - Nuclear Magnetic Resonance

NSET	-	Nanometal Surface Energy Transfer
PAGE	-	Polyacrylamide Gel Electrophoresis
PL	-	Photoluminescence
QD	-	Quantum dot
QD520	-	Quantum dot 520
RET	-	Resoance Energy Transfer
RNA	-	Ribonucleic Acid
SERS	-	Surface Enhanced Raman Spectroscopy
SET	-	Surface Energy Transfer
SNP	-	Single-nucleotide polymorphism
SPR	-	Surface Plasmon Resonance
sp-FRET	-	single particle Resonance Energy Transfer
ss	-	single strand
UV	-	Ultra-violet
VB	-	Valence Band

ABSTRACT

Metal nanoparticles are an important tool in energy transfer assays. The aim of this dissertation is to look deeply into the properties of small gold nanoparticles (Au NP) and how they can affect the experimental observables in energy transfer assays. Absorption, photoluminescence and time-resolved experiments were performed on Au NP-dye pairs separated by dsDNA spacers to deduce the distance dependent quenching behavior for 2 nm Au NP (Chapter 2). A range of dyes were studied with different emission frequencies to set the energetic limits to the quenching behavior of Au NP. The effect of intraband and interband electrons on the quenching behavior of Au NP is different as the intraband quenching follows a $1/R^4$ behavior while the interband quenching is largely unaffected with distance (Chapter 3, 4). The role of NP size is important as the intraband term is highly size dependent and also because of the enhancement effects caused by larger sizes of metal nanoparticles (Chapter 5). The NSET tool is applied for accurately measuring the intercalation of an organic dye into a dsDNA helix as a function of the linker length and salt concentration (Chapter 6).

CHAPTER 1

INTRODUCTION

Energy transfer is a powerful photophysical tool which is based on the phenomenon of radiationless transfer of energy from an excited donor (D) to a proximal acceptor (A)[1, 2, 3, 4]. The nature and the efficiency of this transfer is dependent on the optical properties of the donor, acceptor and the surrounding medium. Energy transfer was first described as a dipole-dipole interaction between a fluorescent donor and an acceptor by T. Forster in 1948[5]. Numerous techniques such as FRET (Fluorescence Resonance Energy Transfer)[5, 6], LRET (Luminescence Resonance Energy Transfer)[7, 8, 9], CRET (Chemiluminescence Resonance Energy Transfer)[10], BRET (Bioluminescence Resonance Energy Transfer)[11, 12], sp-FRET (single particle FRET)[13, 14], NSET (Nanometal Surface Energy Transfer)[15, 16, 17] etc. have been developed in the last few decades which apply the basic principles of energy transfer. Energy transfer techniques rely on the measurement of the intensity quenching and/or the lifetime quenching of the donor. It is very extensively used as a photophysical tool in biology to monitor various *in vitro* and *in vivo* processes such as DNA hybridization and sequencing, protein conformation, diffusion dynamics, intracellular receptor ligand binding and cellular membrane dynamics[1, 2, 11, 18, 19, 20, 21]. The highly sensitive nature of these techniques to changes in distance has led to the use of the term *spectroscopic/optical ruler*[3]. Initial energy transfer studies were carried out using simple dyes as donors and acceptors. The donor dye exhibited emission at a wavelength shorter than the extinction of the donor and the energy transfer was efficient only when the donor emission had a significant overlap with the acceptor extinction. This overlap conditon limited the applicability of the technique as it hindered the choice of donors and acceptors, however this limitation was overcome by the development of the new fluorophores including quantum dots (QDs)[21, 22, 23, 24, 25, 26] and metal nanoparticles (MNPs) as quenchers[15, 16, 20, 27, 28, 29, 30, 31, 32, 33, 34, 35, 36, 37, 38, 39, 40, 41].

The development of quantum dots revolutionized the application of fluorescence based techniques due to their extremely tunable and size dependent optical properties spanning from UV to near IR region with high quantum yields[25, 26]. QDs not only show a higher degree of photostability, resistance to degradation and photobleaching than organic dyes but also offer a large surface area which can be easily modified as desired to serve the needs of any experiment. They can very easily be termed as the second generation of fluorophores with highly desirable properties and tunabilty. The first report about QDs participating in efficient energy transfer was reported in late 90's and their applications have been on a constant rise[42, 43, 44] since then. Their use in energy transfer assays has been limited mainly as donors due to their absorption profiles extending into the UV[45]. There have been a few reports where they have been used as acceptors however the number is very limted[46, 47]. Energy transfer assays using QDs are mostly FRET based[2] and have found applications in a number of bio-inspired assays, such as but not limited to conformational structure of proteins, in dye based photochromic switch, peptide and nucleic acid based biosensors, in molecular beacons, for FRET based photodynamic therapy to cure tumors, single molecule FRET and monitoring protein interactions and dynamics near cellular membranes. Apart from their applications in energy transfer assays they have also been used as visualization agents for *in vitro* and *in vivo* studies to track the fate of small molecules inside a cell, typically as gene delivery agents, for drug delivery and target sepcific tumors[25, 26].

Metal nanoparticles, on the other hand, have been known to human civilization for centuries with earliest applications in staining glass. Their role as efficient optical quenchers was observed as early as 1970s[48]. Noble metal nanoparticles, especially gold NPs, have been extremely popular in biological applications due to their highly reproducible and controlled synthetic methodologies, ease of functionalization, stability at room temperature as well as physiological temperatures and also high levels of biocompatibility[49]. They are employed in biotechnology and biodiagnostics typically as visualization agents in cryo-electron micrography, as drug delivery agents , in gene therapy , in biosensors and in photodynamic therapy[49, 51, 52, 53, 54, 55]. They have also attracted a lot of attention in energy transfer assays due to their ability to quench a wide variety of fluorophores including organic dyes as well as semiconductor quantum dots[17, 27, 28]. Metal nanoparticles are a very interesting candidate in energy transfer assays because they can either quench or enhance the fluorescence of a fluorophore depending on their size and shape and the separation distance between the fluorophore and MNP[17, 56, 57, 58]. Large spherical nanoparticles (r $> 40nm$) and non-spherical particles are known to enhance the yield of a fluorophore[56, 59] when placed very close to the particle while smaller particles quench the fluorophore[15, 16, 17, 28, 37, 60, 61]. Prior to this, the quenching behavior of metal films had already been experimentally observed and theoretically explained. The energy transfer from a fluorophore to a metal nanoparticle or a thin film is more complicated than a simple dipole-dipole approximation due to the drastic changes in the properties of the metal at such small sizes and/or thickness[62, 63, 64]. The quenching behavior has been explained by a variety to groups[48, 59, 65, 66, 67] and the explanations date back to early 1980s where the metal could be either treated as an infinte plane[48, 65, 67] or a shaped structure depending on its morphology[59]. The earliest reports dealt with the quenching behavior of a metal film and the observation was explained by Chance, Prock and Silbey[65] and later modified by Persson and Lang[67]. The quenching behavior by a metal surface under approxiamtions of a perfect mirror behavior were explained by Kuhn[48, 66] and later modified by Chance, Prock and Silbey. Significant effort has been made to treat the MNP quenching under FRET approximations however many groups have repeatedly reported the behavior of a small Au NP as that of an infinite plane[15, 17, 28, 29, 30, 31, 32, 33, 34, 35, 36, 37, 38, 39, 40, 41].

In this chapter, the properties of metal clusters are discussed in detail in Sec. 1.1. The effect of reducing size from bulk to very small clusters on the optical properties is explained. Sec. 1.2 briefly explains the important energy transfer mechanisms *viz.* FRET, G-N (Gersten-Nitzan), CPS-Kuhn and NSET that have been applied to explain the quenching behavior of a metal nanoparticle for a fluorophore. GN theory has also been applied to explain the enhancement which is briefly discussed. In Sec 1.3 the structure of DNA helix is discussed as it is a very widely used biomolecule in energy transfer assays for structure and distance determination. Sec 1.4 gives an overview of the chapters in this dissertation.

1.1 Properties of Metal Nanoparticles

Metals are classically defined as good conductors of heat and electricity. In their bulk form all metals are shiny and do not show any specific colors except for gold and copper. The properties of any material change drastically as the size is decreased, for example the semiconductor particles in the nanometer range show distinct absorption and emission properties analogous to molecular dyes, while metal nanoparticles show vibrant colors in aqueous solutions, highly improved catalytic activity among other things. The change in the properties of materials with size is a result of the change in the band structure of the bulk material. In the bulk form, metals either have partially filled conduction band (CB) or a very small energy band gap between the valence (VB) and conduction band as shown in Figure 1.1. As a result of this the electrons in bulk metal are free, requiring very little energy to move and thus imparting the good conducting properties. In semiconductors and insulators the band gap between the VB and CB is larger than that in metals and hence they show little or no conductivity at room temperature depending on the energy gap.

Properties of metal clusters are different from the parent bulk material (Figure 1.1). The change in their properties can be classifed as: (i) intrinsic effects which concern the changes in the volume and surface properties and (ii) extrinsic effects which are size dependent responses to an external field irrespective of the intrinsic effects[62, 64]. Intrinsic effects will cause changes in the properties such as the ionization potential, chemical reactivity, crystallographic structure; whereas the extrinsic size effects will affect the collective electronic and lattice excitations. One of the striking properties of the clusters is that they have an increased number of atoms on the surface than the core such that the ratio of number of surface atoms (N_s) to the

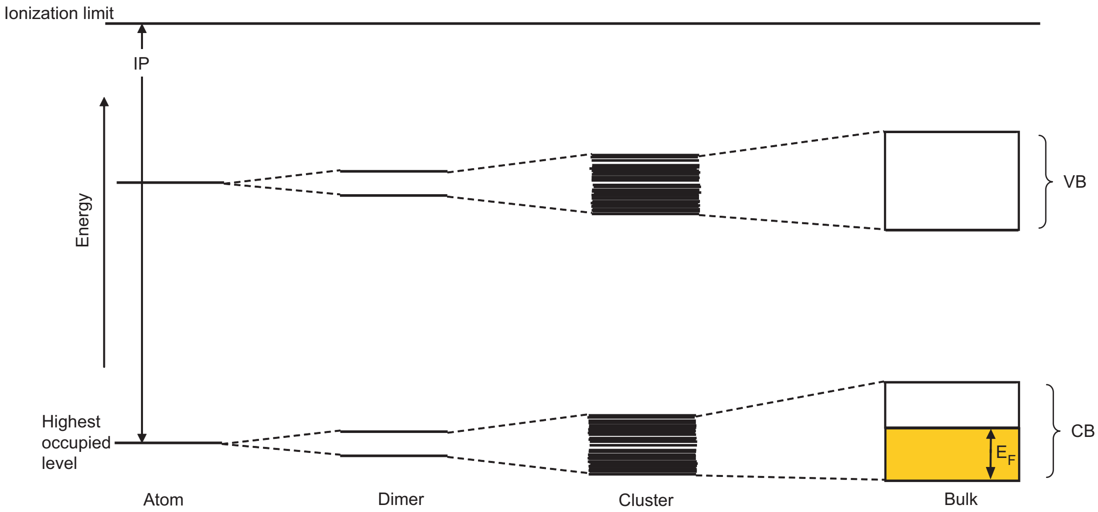

Figure 1.1: Schematic showing the formation of a continuous band structure in metals as the nomber of atoms is increased. Metals have a partially filled conduction band which allows the electron to move freely thus giving metals their properties of conduction.

number of atoms in the core (N_c) increases as the size of the clusters decreases. A cluster exhibits bulk like properties when the $N_s/N_c << 1$. As the ratio becomes bigger with decreasing size of the cluster, the differentiation between core and surface vanishes and all the electrons in the cluster start to behave uniformly[62, 68]. These size effects cause drastic changes in the optical properties of the metal. The bulk metal which exhibits a very unassuming constantly rising extinction with increasing energies develops a structured spectrum when reduced to a cluster of few nanometers in size. For example, the colloids of gold (Au) clusters are a vibrant red color and show a sharp peak at 525 nm, which is absent in the case of bulk metal. Similarly silver (Ag) clusters show an extinction maximum at 400 nm whereas bulk Ag absorption has no such feature.

The optical response of a metal cluster can be explained by taking into account the dielectric property of the cluster, $\epsilon(\omega) = \epsilon_1(\omega) + i\epsilon_2(\omega)$ and the dielectric constant of the surrounding medium ϵ_m. When the value of $\epsilon_1(\omega) = -2\epsilon_m$, the collective oscillation of the electrons is at resonance with the external field of the incident light[62, 64, 63, 69]. As this resonance condition is fulfilled the extinction of the cluster rises sharply and a peak is observed at that wavelength. For different metals, the resonance condition is fulfilled at different wavelengths (for Au at 525nm, Ag at 400nm) and is called the localized surface plasmon resonance (LSPR). The position of the LSPR is dependent on the size of the particle such that an increasing size of the particle shifts the SPR by a few nanometers[51, 63, 69]. It is the presence of the surface plasmon behavior that gives gold colloids their vibrant red color and the silver colloids their yellow color. Complete theoretical treatment to explain the interaction

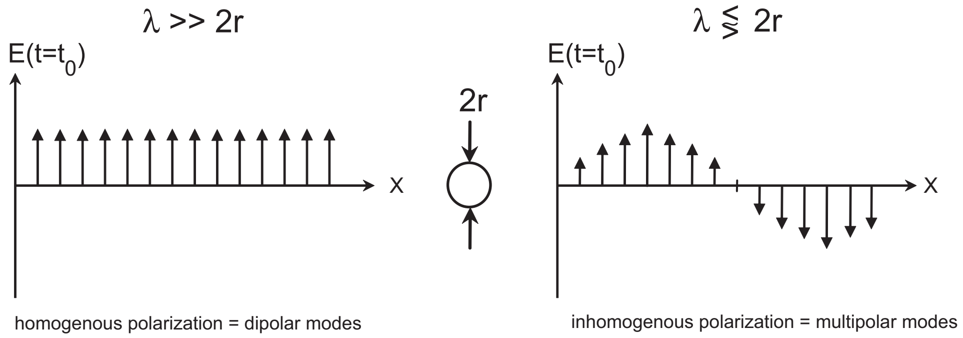

Figure 1.2: A comparison between a the polarization in a small metal nanoaprticle ($\lambda >> 2r$) and when the particle diameter is comparable or larger than the wavelength of light. In a small particle, the electromagnetic field causes a homogenous polarization and only the dipolar modes are excited. At large sizes the interacting field causes a lag in the particle leading to inhomogenous polarization. As a result, the smaller particles only show the dipolar modes while higher order modes along with dipolar modes are seen in larger particles.

of light with metal clusters was first provided by Mie in 1908 by solving Maxwell's equations for the incident light[62, 63]. For a spherical particle, the solution of the Mie theory gives the extinction cross section, σ_{ext} for a particle of radius r as

$$\sigma_{ext} = 9\frac{\omega}{c}\epsilon_m^{3/2}V_0\frac{\epsilon_2(\omega)}{[\epsilon_1(\omega)+2\epsilon_m]^2+\epsilon_2(\omega)^2} \tag{1.1}$$

where, $V_0 = (4\pi/3)r^3$ is the volume of the particle, $\epsilon_1(\omega)$ and $\epsilon_2(\omega)$ are the real and imaginary components of the dielectric function of the metal and ϵ_m is the real dielectric of the medium. This extinction cross section is due to dipolar modes only and hence applicable to very small particles whose diameter is much smaller than the wavelength of the interacting light (λ)[62]. In the case of small particles the incident field is able to uniformly polarize the charges on the surface and hence only dipolar modes are observed (Figure 1.2). As the size of the particle is increased, the time dependent incident field causes a phase lag in the particles leading to inhomogenous polarization in the particle (Figure 1.2). This leads to higher order multipolar excitations[62]. The multipolar modes are higher in energy than the dipolar mode and observable in spherical particles when the diameter is comparable or larger than the wavelength of incident field and also in shaped particles such as rods (with high aspect ratios)[70]. For Au nanorods, along with the LSPR peak at 525 nm, another peak at lower energies (800-900 nm) is seen which corresponds to the resonant oscillation of electrons along the long axis of the particles. This is called the longitudinal mode and its intensity is dependent on the aspect ratio of the nanorod. The resonant oscillation along the short axis is called the transverse mode and is dependent upon the radius (Figure 1.3).

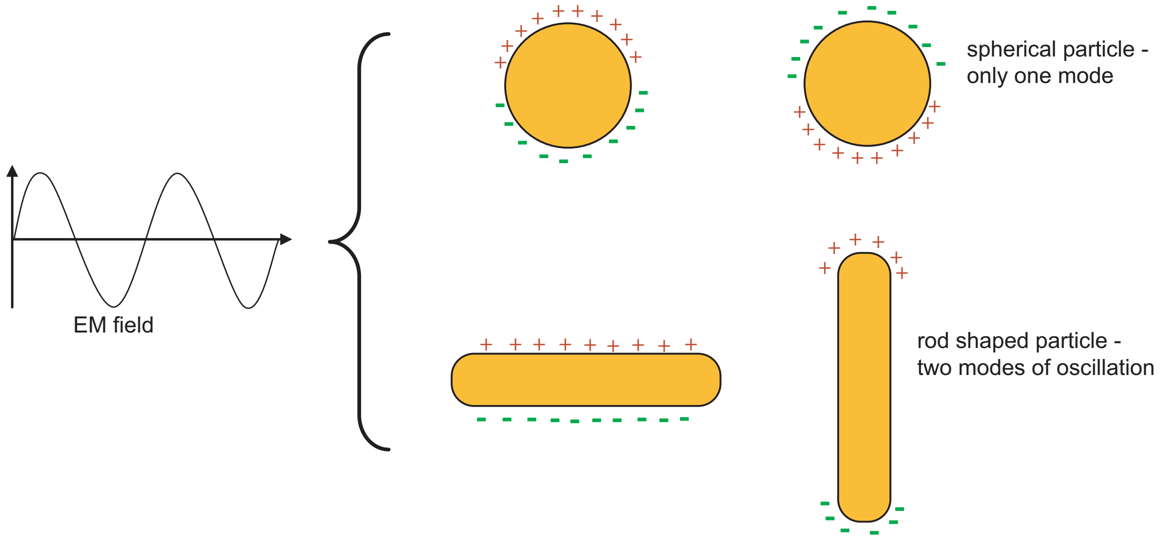

Figure 1.3: Spherical particles which have a center of symmetry show only one mode of dipolar oscillation of electrons while nanorods with two axes show transverse and longitudinal dipolear modes corresponding to the resonant oscillation of electrons along the short and log axes respectively.

The extinction spectrum of a nanoparticle can be broken down to absorption (σ_{abs}) and scattering (σ_{sca}) contributions[56, 62, 71]. The real part of the refractive index makes up the scattering spectrum while the imaginary part contributres to the absorption. The total Mie extinction cross-section can now be written as,

$$\sigma_{ext} = \sigma_{sca} + \sigma_{abs} \tag{1.2}$$

Both, σ_{abs} and σ_{sca} play an important role in explaining the behavior of a flurophore when placed close to a metal nanoparticle[56]. Metal nanoparticles have been known to either quench or enhance the fluorescence of a fluorophore. There have been several theories which have been employed to describe the experimental observations, some of which are described in the next section. It has also been suggested that both quenching and enhancement may be two simultaneously competing processes, each being a function of nanoparticle size, its polarizability and properties of the fluorophore. The absorption cross section (σ_{abs}) causes quenching while the scattering cross section (σ_{sca}) is responsible for enhancement. The scattering cross section is highly size dependent as shown in Figure 1.4 and more intense in the low energy region while absorption is intense in the blue region. For Au nanoparticles, the scattering is negligible for particles with radius $<$40 nm[56] (Figure 1.4).

As mentioned, the optical properties are a function of the dielectric function and as evident from the Equation 1.1 that the extinction cross section will be a fucntion

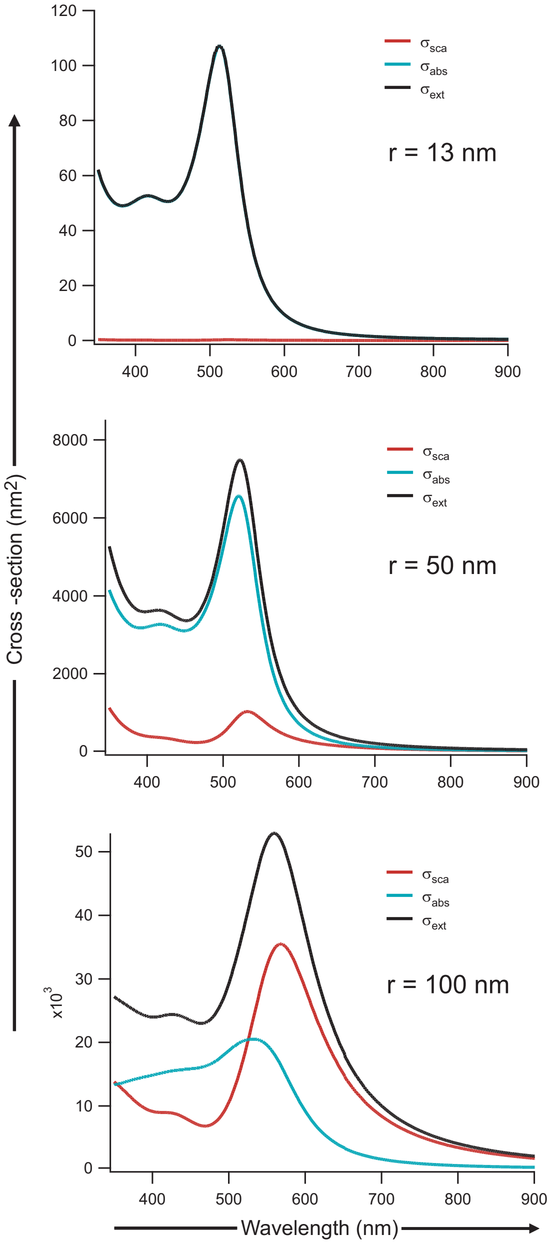

Figure 1.4: The extinction properties (σ_{ext}) of spherical nanoparticles are a combination from the scattering (σ_{sca}) and the absorption (σ_{abs}). The scattering component becomes more prominent as the size of the particle is increased. A gold particle with $r = 100$ nm has σ_{sca} much bigger than that of a particle with $r = 13$ nm.

of $\epsilon(\omega)$. When the size of a nanoparticle is reduced such that it is a cluster of just a few atoms, the optical constants which otherwise only have a energy dependence develop a size dependence as well, such that $\epsilon(\omega) \rightarrow \epsilon(\omega, r)$. One of the classical models to treat the size dependence is by taking into account the change in the mean free path of the electron with decreasing size[63]. For a bulk material ($r \rightarrow \infty$), the relaxation/damping constant Γ_∞ for the electrons is related to the bulk mean free path (l_∞) such that,

$$\Gamma_\infty = \upsilon_F / l_\infty \tag{1.3}$$

where υ_F is the Fermi velocity of the metal. The size dependent relaxation, $\Gamma(r)$ is related to the bulk relaxation by the following relation

$$\Gamma(r) = \Gamma_\infty + A\frac{\upsilon_F}{r} \tag{1.4}$$

where the value of A depends on the nature of scattering processes and can vary from 0.1-4.0[62, 63]. For spherical particles assumed to behave under the Maxwell theory and exhibiting isotropic scattering, $A = 1$ whereas $A \leq 4$ for particles exhibiting grain boundary scattering. In some cases it has been reported that it can be a function of chemical composition especially for adsorbed or matrix-embedded clusters[62].

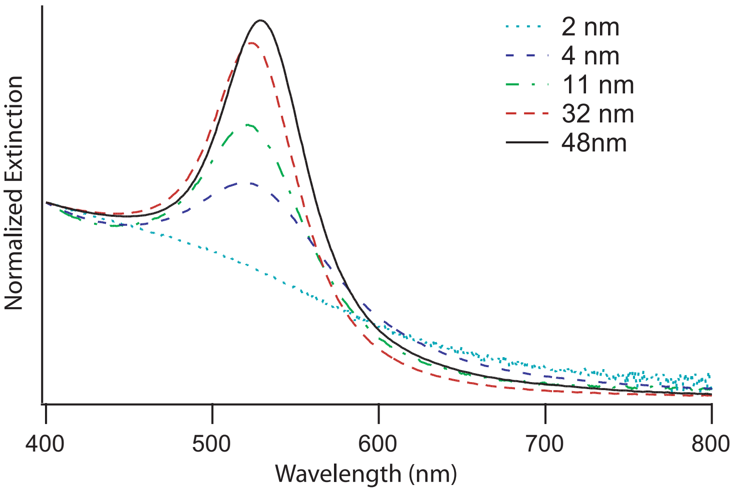

Figure 1.5: The size dependence of the extrinction spectra of cluster is very prominent as the size is reduced to a few nanometers. The figure shows the experimentally measured extinction of spherical Au NPs of diameter 2 nm, 4 nm, 11 nm, 32 nm and 48 nm.

Traditionally metals were treated under the Drude approximation where all the properties are due to the transitions of the conduction electrons only while all inner lying electrons are ignored[62, 64, 72]. The Drude approxiamtion may still hold true for some of the alkali metals, however this approximation breaks down for noble metals whose inner lying d electrons contribute to their optical properties. In this case, the total dielectric function can be written as,

$$\epsilon(\omega) = \epsilon^{D} + \epsilon^{IB} \tag{1.5}$$

where, ϵ^{D} is the Drude contribution due to the conduction electrons and ϵ^{IB} is the interband contribution due to the inner lying electrons.

The interband transitions are largely assumed to be size independent[62, 63] unless the cluster is composed of only a few atoms at which point the band structure diminishes and the cluster behaves as a molecule. The Drude transitions are size dependent and related to the modified relaxation constant $\Gamma(r)$. The total size dependent dielectric function can be written as,

$$\epsilon(\omega, r) = (\epsilon_1^{D} + \epsilon_1^{IB}) + i(\epsilon_2^{D} + \epsilon_2^{IB}) \tag{1.6}$$

The size dependent real ($\epsilon_1^{D}(\omega, r)$) and the imaginary ($\epsilon_2^{D}(\omega, r)$) Drude contributions are a function of the plasma frequency, ω_p:

$$\epsilon_1^{D}(\omega, r) = 1 - \frac{\omega_p^2}{\omega^2 + \omega_s^2} \tag{1.7}$$

$$\epsilon_2^{D}(\omega, r) = \frac{\omega_p^2 \omega_s}{\omega(\omega^2 + \omega_s^2)} \tag{1.8}$$

where, $\omega_s = A\frac{v_F}{r}$ is the size dependent relaxation correction term[63]. The effect of changes in the dielectric properties with decreasing size is so drastic that the LSPR peak for Au clusters $r < 2$ nm is completely damped and the extinction coefficient is reduced as shown in Figure 1.5.

1.2 Theory of Energy Transfer

Energy transfer is defined as a radiationless transfer of energy from a donor to an acceptor [1, 2, 3, 4]. The donor is a fluorophore and the acceptor could be another flurophore of lower energy, a dark quencher, a metal film or a metal nanoparticle. It is an important tool and has found applications in medical diagnostics, DNA analysis, optical imaging, structure determination, gene therapy, drug delivery and optical imaging[1, 2, 3, 11, 20, 28]. The rate of energy transfer (k_T) between a donor and acceptor is dependent on their optical properties, the distance of separation[3] (R),

$$k_T = \frac{1}{\tau_{dye}} \left(\frac{R_0}{R}\right)^n \tag{1.9}$$

where τ_{dye} is the native lifetime of the donor in the absence of acceptor, R_0 is the distance at which efficiency of energy transfer is 50%, also called the critical distance and n is a fitting parameter. Both R_0 and n are highly dependent on the nature of the donor and acceptor with n being a function of the dimensions of the donor and acceptor wheres R_0 directly relates to the photophysical constants for the donor and acceptor. It is evident from the Equation 1.9, k_T is distance dependent and hence has found widespread application in structural biology to measure distances in biomolecules, monitor structural/conformational changes. There have been several theories which have attempted to explain the nature of energy transfer under different conditions for the D-A pair such as FRET[5], G-N theory[59], CPS-Kuhn[66] model and NSET[16] being some of the important ones. These energy transfer mechanisms have been summarized in Figure 1.6 and a brief discription of these theories, their assumptions and limiting conditions are provided in the following paragraphs.

1.2.1 Forster Resonance Energy Transfer (FRET)

The theory of energy transfer was first developed by T. Forster in 1948 where the transfer of energy from a higher energy organic dye (D) to a lower energy dye (A) was explained and termed Fluorescence/Forster Resonance Energy Transfer (FRET) even though no photon energy is transferred in the process. It has been suggested that Resonance Energy Transfer (RET) is a more appropriate term. There are several other energy transfer processes such as LRET, BRET, CRET, sp-FRET, etc[11]. which have been explained under the FRET formalism. In FRET, the interaction between D and A is explained by treating them as zero-dimensional single point dipoles under the weak coupling limit. Distances ranging from 20-90Å are conveniently measured in FRET experiments which are comparable to the size of most of the biomolecules. The fitting parameter $n = 6$ in FRET and the 50% energy transfer distance (R_0^{FRET}) for FRET is given by[3],

$$R_0^{FRET} = \left[\frac{9000(ln10)\kappa^2\Phi_{dye}}{128\pi^5 N_A n^4} J(\lambda)\right]^{1/6} \tag{1.10}$$

where κ is the orientation factor, Φ_{dye} is the quantum yield of the donor, N_A is Avogadro's number, n is the refractive index of the medium, and $J(\lambda)$ is the overlap integral. The overlap integral $J(\lambda)$ is a measure of the extent of overlap between the donor emission spectrum and the extinction spectrum of the acceptor. A high value for $J(\lambda)$ ensures a high R_0^{FRET} and hence longer measurable distances. The orientation term κ describes the relative orientation of the donor and the acceptor with respect to the each other such that $\kappa = cos\theta_T - 3cos\theta_d cos\theta_a$ where θ_T is the angle between the emission transition dipole of the donor and the absorption transition dipole of the acceptor, θ_d and θ_a are the angles between these dipoles and the vector joining the donor and the acceptor. The value of κ can vary from 0 (dipoles perpendicular to each other) to 4 (dipoles oriented parallel to each other) depending on the relative orientation of the donor and the acceptor. Most of the FRET experiments are conducted in solution where the dipoles are randomly oriented, therefore $\kappa = 2/3$ is the generally agreed upon and commonly used value in FRET experiments[3]. Fluorescence anisotropy experiments can help eliminate the uncertainties in the value of

κ and give a more accurate estimate of the measured distances. The value of R_0^{FRET} for the most commonly available donor-acceptor pairs varies from 10-60Å [3]. The FRET formalism has also been applied to the quenching of flourophores and semiconductor quantum dots by small metal nanoparticles. However, the assumption of a small metal nanoparticle to behave as a single point dipole is debatable due to the presence of conduction electrons and different molecular orbital diagram[17, 62].

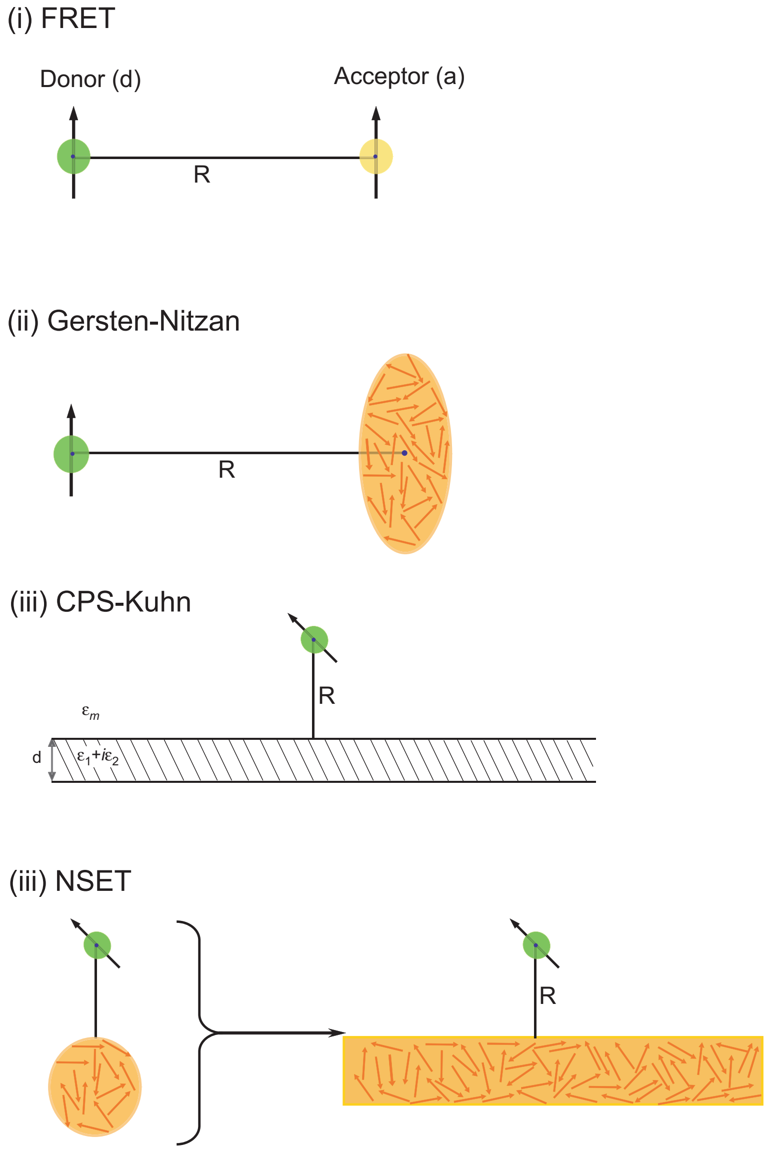

Figure 1.6: A comparison of the (i)FRET, (ii)G-N, (iii)CPS-Kuhn and (iv)NSET models.

1.2.2 Gersten-Nitzan (G-N) model

Metal nanoparticles, due to their large extinction coefficient can very well act as energy collector (quencher) and also as a field amplifier (enhancer) for a fluorescing molecule. This is the basis of the Gersten-Nitzan theory which was proposed in 1981, to explain the phenomenon of surface enhanced fluorescence (SERS) observed when a fluorescing molecule was placed close to a metal nanoparticle, on rough metal surfaces or on metal island films[59]. The phenomenon of SERS is assumed to be a result of the modified local electromagnetic field around the fluorophore due to the image, shape and plasmon resonance effects of the metal. The fluorophore is assumed to behave as a classical point dipole which is placed at a distance R from the center of a particle of radius r such that $r <<< \lambda$. The assumption of the particle being much smaller than the wavelength of light (λ) allows for the problem to be treated within the electrostatic theory. The assembly of the particle with the fluorophore placed in vicinity is treated as one complete system with a dipole moment which has contributions from both the metal and the fluorophore. This is considered to be more appropriate because of the generation of the induced dipole due to the electric field of the metal. The induced dipole causes an image enhancement effect which is prominent at distances closer to the surface. The field of the particle affects both the radiative decay, k_r and also causes the metal to act as an acceptor of energy. If the changes in the radiative rate (k_r) are ignored and only energy transfer, k_{ET} is the dominant process, then the 50% energy transfer distance (R_0^{GN}) can be written as[17, 59],

$$R_0^{GN} = \left[2.25 \cdot \frac{c^3}{\omega_{dye}^3} \cdot \Phi_{dye} \cdot r^3 \cdot \frac{(\epsilon_1 + 2)^2 + \epsilon_2^2}{|\epsilon_2|^2} \right]^{1/6} \tag{1.11}$$

where, ω_{dye} is the frequency of the donor dye, Φ_{dye} is the quantum yield of the donor, r is the radius of the metal nanoparticle, ϵ_1 and ϵ_2 are the real and imaginary components of the dielectric constant of the metal and c is the speed of light. This equation is derived under the assumption that there is no change in the radiative rate of the dye molecule in the presence of the metal NP and therefore no enhancement effects.

The enhancement effect under G-N theory can be expalined by first looking at the native quantum yield (Φ_{dye}) of a fluorophore. Φ_{dye} is the ratio of the light emitted by a molecule to the amount of light absorbed. It can also be written in terms of the radiative (k_r) and non-radiative (k_{nr}) decay rates for the molecule such that[73],

$$\Phi_{dye} = \frac{k_r}{k_r + k_{nr}} \tag{1.12}$$

and the native lifetime (τ_{dye}) is give as,

$$\tau_{dye} = \frac{1}{k_r + k_{nr}} \tag{1.13}$$

thus,

$$\Phi_{dye} = k_r \cdot \tau_{dye} \tag{1.14}$$

The presence of an acceptor adds another pathway for loss of energy such that the modified quantum yield ($\Phi^{'}_{dye}$) and lifetime ($\tau^{'}_{dye}$) are,

$$\Phi_{dye} = \frac{k_r}{k_r + k_{nr} + k_{ET}} \tag{1.15}$$

$$\tau_{dye} = \frac{1}{k_r + k_{nr} + k_{ET}} \tag{1.16}$$

$$\Phi^{'}_{dye} = k_r \cdot \tau^{'}_{dye} \tag{1.17}$$

When there is no change in the radiative rate (k_r), a decrease in the quantum yield and lifetime is observed. An enhancement is seen when the field of the particle affects the radiative rate. The non-radiative paths are a collection of the vibrational and rotational pathways which are independent of the presence of any acceptor and are hard to get rid of at ambient experimental temperature conditions. Under the assumptions of G-N theory, the enhancement can be calculated in terms of an enhancement factor (η) such that[58],

$$\eta = \mathbf{A}(\lambda) \cdot \frac{\Phi^{'}_{dye}}{\Phi_{dye}} - 1 \tag{1.18}$$

where $\mathbf{A}(\lambda)$ is the field enhancement factor related to the dielectric of the metal $\epsilon(\lambda)$ at the absorption wavelength of the metal, radius of the metal nanoparticle (r) and the distance (R) of the fluorophore from the center of the particle,

$$\mathbf{A}(\lambda) = 1 + 2 \cdot \left| \frac{\epsilon(\lambda) - 1}{\epsilon(\lambda) + 2} \right|^2 \cdot \left(\frac{r}{R} \right)^6 \tag{1.19}$$

The enhancement thus follows a $1/R^6$ behavior and is highly dependent on the size of the particle[56, 58].

1.2.3 CPS-Kuhn model

Much before the MNPs drew attention, thin metal films had already been studied and their effects on a proximal fluorophore had been postulated. One of the prominent theories is by Kuhn which was proposed in the year 1970[48]. The theory deals with the quenching of an emitting fluorophore when placed close to a thin metal film and is applicable when the thickness (d) of the film is less than the distance of the flurophore from its surface (R). The emitter is again treated as a simple harmonic oscillator and the metal film is assumed to be a perfect mirror with a reflectivity of unity. The emitting field from the donor induces oscillations in the acceptor and this induced field in the acceptor travels back to the donor and slows down the aceptor oscillator. Thus it can said that the quenching in Kuhn theory is a retardation effect on the emitter due to the acceptor. The theory also explains the quenching of a qdrupole emitter by a metal thin film acceptor. However, it was later found that the Kuhn's theory greatly over-estimated the extent of energy transfer and it was modified by Chance, Prock and Silbey such that the modified critical distance ($R_0^{CPS-Kuhn}$) is given as[17, 48, 66, 74],

$$R_0^{CPS-Kuhn} = \frac{\alpha\lambda}{n}(\overline{A}q)^{1/4}\left[\frac{n_r}{2n_m}\left(1+\frac{\epsilon_1^2}{\mid \epsilon_2 \mid^2}\right)\right]^{1/4} \tag{1.20}$$

where, $\overline{A}$ is the absorptivity of the mirror $\overline{A} = \frac{4\pi kd}{\lambda}$ and $\alpha = (\frac{1}{4\pi})(9)^{1/4}$ for a dipole oriented perpendicularly to the metal surface while it takes a value of $(\frac{1}{4\pi})(\frac{9}{2})^{1/4}$ when the dipole is aligned parallel to the metal surface, λ is the emission wavelength of the donor dipole; ϵ_1, ϵ_2, and n_r, k are the real and imaginary components of the dielectric constant and the refractive index of the metal respectively, n_m is the refractive index of the medium; and d is the thickness of the mirror. In CPS-Kuhn, it is assumed that the dielectric constants are not size-dependent. However, as shown by Kreibig[62], a modification to the CPS-Kuhn theory incorporating the size dependence of the dielectric constants can be accounted for by substituting a size dependent term for the dielectric constants[62, 64, 99].

1.2.4 Nanometal Surface Energy Transfer (NSET)

The Nanometal Surface Energy Transfer model is an extension of the theory proposed by Persson and Lang in the year 1981 where quenching behavior of a metal surface on an oscillating dipole was studied[67]. The metal is treated within the jellium approximation. The frequency of oscillation of the dipole (ω_{dye}) is smaller than the plasma frequency (ω_p) of the metal as only in this region the conduction electrons of the metal can respond adiabatically to the slowly varying external field and adjust to the instantaneous static configuration. The theory explains the effects of the metal surface on the emitter in the long distance range such that $d >> \omega_F/\omega_{dye}k_F$ where ω_F is the Fermi frequency and k_F is the Fermi wave-vector for the metal. The theory also assumes that the surface of the metal is going to affect the emitter differently than the volume, therefore the effects of surface and core electrons are considered separately. This makes the theory extremely applicable to the metal nanoparticle quenching as the surface and core electrons behave differently. The rate of surface quenching is a function of the electron gas density parameter (r_s) while the volume damping is a function of the bulk dielectric function arising from the scattering of the electrons against the phonons, impurities etc. The generalized damping can be written as,

$$k_{ET} = \frac{\mu^2}{4R^3\hbar}\cdot F \tag{1.21}$$

where, μ is the dipole moment of the emitter, R is the distance of the emitter from the metal surface and F is the surface or volume dependent quenching term such that,

$$F_{surface} = 1.2\frac{\omega_{dye}}{\omega_F} \cdot \frac{1}{k_F R} \tag{1.22}$$

and,

$$F_{volume} = 3\frac{\omega_{dye}}{\omega_F} \cdot \frac{1}{k_F l} \tag{1.23}$$

The volume quenching is thus a function of $1/R^3$ and the mean free path (l) for the metal while the surface quenching is a $1/R^4$ dependent phenomena. For very small particles where the surface and the volume are indistinguishable, only surface quenching is observed while for large particles which have a well formed surface and a distinguishable volume, surface quenching is observed at shorter distances while volume quenching plays a dominant role at longer distances. Also, for metals with extremely long mean free paths such as the noble metals, surface quenching is the dominant player at distances as long as 300 Å. With these approximations and results the critical distance R_0^{NSET} is calculated as[16, 65, 66, 67]

$$R_0^{NSET} = \left(0.225 \cdot \frac{\Phi_{dye}}{\omega_{dye}^2} \cdot \frac{1}{\omega_F k_F} \cdot c^3\right)^{1/4} \tag{1.24}$$

where, $k_F = 1.2 \times 10^8 cm^{-1}$ and $\omega_F = 8.4 \times 10^{15} rad/s$ are the constants for the metal acceptor derived from bulk gold; ω_{dye} and Φ_{dye} represent the angular frequency of donor emission and the quantum yield of the donor respectively and $c = 3.0 \times 10^8 m/s$ is the speed of light.

1.3 DNA structre

The double helical structure of DNA was first discovered by Watson and Crick by solving the X-ray diffraction pattern of DNA crystals[76]. In its biological form DNA is a very big molecule with a highly coiled structure, however for synthetic DNA it has been reported that DNA molecules with up to 100 base pairs (bp) have a linear geometry with only very low frequency oscillations[77, 78]. A linear DNA molecule is best described as a cylinder with the complementary strands coiled around it[76, 79]. The helical nature of the DNA leads to the formation of major and minor grooves within the DNA structure as shown in Figure 1.7b. The major groove is slightly deeper than the minor groove at 8.5 Å versus 7.5 Å [76]. Each of the grooves is lined by potential hydrogen bond donor and acceptor atoms allowing proteins to interact with and recognize specific DNA sequences and smaller molecules to inertcalate into the DNA helix in which case the distances must be reported with care. Binding into the major groove is more common for proteins whereas the small molecules tend to either bind into the minor groove or can intercalate into the DNA helix. Most of the DNA staining/visualizing dyes work by either intercalating into the DNA or by binding the minor groove of the DNA[80]. Intercalation is observed for cationic molecules having planar aromatic rings and creates strain into the helix as it requires adjacent base pairs to separate from one another to create the binding pocket for the ligand. Minor groove binding does not strain the DNA helix as much because the binding molecule usually has some degree of flexibility allowing its structure to twist accordingly to follow the groove. Members of the acridine family and commonly used DNA stain ethidium bromide are known DNA intercalators whereas netropsin and many of the cyanine dyes are minor groove binders.

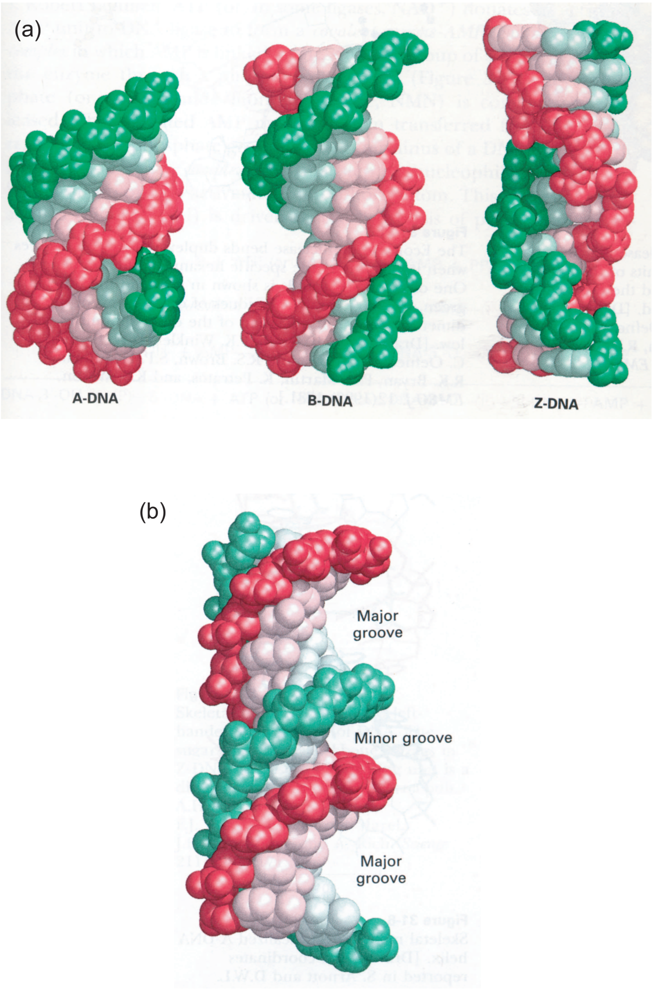

Figure 1.7: (a)A comparison between the A-, B- and Z-DNA structures. B-DNA is the most commonly found structure of DNA which can take the A- form under anhydous conditions. The Z-DNA structure is seen at very high salt concentration. (b)Structure of B-DNA highlighting the location od major and minor grooves in the double helix structure[76].

Most of the techniques available for measuring distances in DNA such as NMR, EPR etc., are restricted to very short distancs. Energy transfer techniques offer advantages for measuring longer distances and allow for observing the helical geometry in small DNA molecules. This was shown by Clegg *et. al.*[79] in 1993 where FRET was used to monitor the helical geometry of dsDNA. This study also helped propose a model to accurately predict the distances in a B-DNA double helix. Each base in DNA contributes 3.4 Å to the total length however the distance between the two ends is not a simple $3.4\Delta N$ due to the helical geometry, where ΔN is the base pair separation between the two points of interest. The distance approximation becomes more critical for structure determination studies. Presence of linkers binding the labels/moieties and their felixibility complicates the distance approximation. For energy transfer studies when a donor (D) and an acceptor (A) are linked to a double strand DNA with linkers of length r_d and r_a respectively separated by ΔN bases; the distance R between the D and the acceptor can then be accurately calculated by assuming the cylindrical model for the double strand DNA such that

$$R = [(3.4\Delta N + L) + \xi]^{1/2} \tag{1.25}$$

where, L is the increased separation distance between D and A due the helical nature of the DNA and ξ, the cylinder base vector is a function of the linker lengths (r_d, r_a) and the angle subtended by the linkers for a zero base pair separattion (θ) such that $\xi = r_a^2 + r_d^2 - 2r_ar_d[cos(\theta + 36\Delta N)]$. The values for the linker length (r_d, r_a) vary according to the choice of the linker and their flexibility. For a six carbon linker C_6 values from 0 Å up to 15 Å have been reported for the completely folded back and totally extended conformations respectively[79]. This, however, is a simplistic model which does not account for interactions that can occur between the labels and the DNA molecule.

The Clegg model is applicable to B-DNA which is the most commonly found sturcture for DNA. Other forms of DNA such as A-DNA and Z-DNA are also known (Figure 1.7a). The A helical structure is seen for DNA crystals when the relative humidity goes below 75% however its not restricted to only dehydrated DNA. Some double stranded RNA such as hairpins and RNA-DNA hybrids have also shown to adopt the A helix. The minor groove nearly vanishes in the A form with fewer water molecules binding the phosphate backbone. The Z-DNA is a left handed helix unlike A and B which are both right handed.

1.4 Summary of Chapters

This dissertation is directed towards understanding the quenching behavior of gold nanoparticles towards the excited state of organic dyes. The quenching mechanism of NSET is probed and limiting conditons are postulated. In Chapter 2 the initial observation of quenching by a 2 nm Au nanoparticle and the applicability of NSET is described. The spectroscopic range for NSET is established in Chapter 3 where the importance of the LSPR (localized surface plasmon resonance) of Au NP is also investigated. Chapter 4 looks at the quenching behavior of organic dyes which have their emission frequencies blue (higher energy) to the LSPR peak of the nanoparticle. The wavelength region blue to LSPR is important as the interband transitons become more important. Chapter 5 investigates the role of size of Au nanoaprticle on the nature of the interaction between the Au NP and organic dyes. Chapter 6 applies the NSET model to monitor the intercalation of a cyanine dye into ds-DNA. The interaction of the dye with the DNA is experimentally investigated as a function of the position of the DNA along the DNA backbone, length of the linker and salt concentration.

CHAPTER 2

NSET VS DISTANCE TO D=1.5 NANOPARTICLES

2.1 Introduction

Application of optical molecular rulers to questions in biochemistry, bio-diagnostics, and bimolecular imaging allows routine measurement of dynamic distance changes in molecules. We recently demonstrated the applicability of a long range molecular ruler consisting of an organic dye donating energy to a small (1.4 - 1.5 nm diameter) gold nanoparticle, termed nanosurface energy transfer (NSET)[15, 16]. This technique allowed changes in conformational distances between 1 - 20 nm to be probed for protein-nucleic acid interactions on double strand DNA (dsDNA) using optical methods. NSET is similar to Forster resonance energy transfer (FRET), however the measurable distances are extended nearly 2-times for optical molecular rulers by following a $1/R^4$ distance dependence. The intensity quenching mechanism *via* coupling of the oscillating electronic dipole of a dye to a metal surface with loss of energy *via* heat is analogous to the theoretical treatment developed by Chance, Prock and Silbey[65] and Persson and Lang[67] for bulk metals. This theoretical treatment can explain the oscillator coupling to a metallic nanoparticle (NP) with surprisingly good agreement to experimental data[15, 16, 17], which is unexpected because a 1.5 nm Au NP has neither a significant core, nor displays strong surface plasmon resonance (SPR) character. The observation of quenching behavior that follows the theoretical treatment of Persson and Lang for a bulk metal is surprising due to the poorly developed surface in materials below 2 nm. While these systems are above the limit where the crystal field levels split, they are not large enough to express a coherent surface plasmon resonance. This may not be critical if the logic of Ruppin is applied, where he has theorized that the primary difference between the rates of energy transfer to a plane and to a sphere is manifest in the loss of lifetime oscillations at large distance in the spherical case, due to reduced reflectivity[81]. This implies that an energy transfer mechanism may not be drastically affected by moving from a plane to the spherical acceptor case. Although the experimental results are consistent with NSET behavior, seemingly contradictory findings for the optical response of molecular dyes interacting with metal NPs have been reported in the literature with both radiative rate enhancement and energy transfer quenching at moderate distances[56, 60, 82]. A common theme for most theories relies upon the existence of a surface plasmon resonance (SPR) band in the metal particle. The lower quantum efficiency of fluorophores near or on metal surfaces has been interpreted in terms of lossy surface waves[83, 84], or by suppression of the radiative rate[60]. Under certain conditions, photoluminescence enhancement has been reported and is described as resulting from wavevector matching and coupling to a plasmon for far-field emission via a classical description of light[56]. An interesting question presents itself, therefore, when inquiring about the behavior of a dipole-emitter when the metal does not exhibit an SPR band, such as occurs when the metal particle is very small, $\leq$2 nm[63]. Because 1.5 nm diameter gold NPs do not display surface plasmon character, the only means by which dye quenching will be observed is limited to either a change in the radiative rate (k_r) of the dye or the introduction of an energy transfer rate k_{ET} to the metal NP. The details of the mechanism can be probed by correlating the photoluminescence (PL) and lifetime (τ) behavior for a set of dyes, spaced at controlled distances The relationship between photoluminescence (PL) intensity and lifetimes is easily shown by considering that:

$$\tau_{obs} = \frac{1}{k_{obs}} = \frac{1}{k_r + k_{nr} + k_{ET}} \tag{2.1}$$

$$\Phi_{em} = \frac{k_r}{k_r + k_{nr} + k_{ET}} = k_r \tau_{obs} \tag{2.2}$$

where Eqns. 2.1 and Eqn. 2.2 state that the observed lifetime, τ_{obs} is the inverse of all rates of decay, k_{obs}; where k_{obs} is the sum of the radiative rate, k_r, the non-radiative rate, k_{nr}, and the rate of energy transfer, k_{ET}. The radiative and non-radiative rates are normally considered constants for a dye under defined conditions, leaving k_{ET} as the major contributor to the shortening of an observed lifetime. The quantum yield (Eqn. 2.2) is a convenient measurement relating PL intensity to k_r and the observed lifetime, τ_{obs}. For a high quantum efficiency dye, k_{nr} is very small and one predicts that a change in k_r will lead to a corresponding change in the observed lifetime of a dye, affecting the measured Φ_{em}. Conversely, energy transfer should lead to a correlated loss in lifetime and intensity for the NP-dye combination. A dilemma is presented by these statements because both a changing k_r and the introduction of an energy transfer pathway (k_{ET}) could lead to the observation of quenched PL and a decreased lifetime. How can one distinguish the true origin of the decreased PL intensity? The purpose of this study is to demonstrate that the mechanism of PL quenching for an organic dye near a small 1.5 nm NP is almost entirely *via* energy transfer to the metal surface and that the quenching efficiency is defined by a $1/R^4$ distance dependence, consistent with the predictions of Persson and Lang in an NSET model.

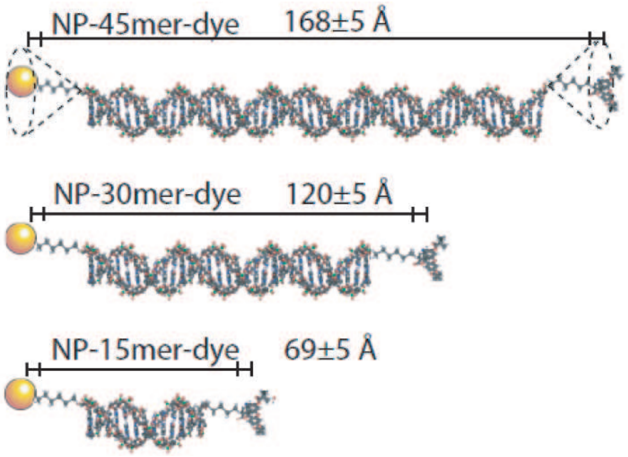

Figure 2.1: Scheme of Au-dsDNA-Dye assembly. Using different lengths of ds-DNA allows to control the separation distance between the Dye and 2 nm Au NP.

2.2 Experimental

2.2.1 Nanoparticle Synthesis

Gold nanoparticles were synthesized as described by literature techniques[85], using the rapid reduction of hydrogen tetrachloroaurate ($AuCl_4 \cdot 3H_2O$) in the presence of tetraoctylammonium bromide by sodium borohydride in an argon-sparged water/toluene mixture. TEM measurements displayed particles with an average diameter of 1.5 ± 0.5 nm. The particles were washed thoroughly with a variety of solvents including hexanes, sodium nitrite solution, and MeOH-H_2O. Ligand exchange was accomplished using 400 mg Bis-(*p*-sulfonatophenyl)phenylphosphine dihydrate (SPP) in 30 mL nanopure H_2O to 32 mg purified nanocrystal in 32 mL methylene chloride. The two phases were stirred overnight resulting in extraction of the organically-soluble NP to the aqueous phase through ligand exchange. Aqueous NP was lyophilized into small aliquots of ~20 nmol/vial and stored at 4°C.

2.2.2 ds-DNA Nanoparticle Coupling

Complementary DNA strands were purchased with either $5'$-C_6-dye or $5'$-C$-$6-SH already HPLC-purified from IDT DNA Technologies. All strands were engineered to minimize secondary structures using mFold. Purity for Cy5-labeled DNA was verified *via* HPLC analysis (C-4, 300Å, 10-80% acetonitrile in 45 minutes). Purity for FAM and thiol-labeled DNA was verified on FPLC, (30-90% 1M NaCl in 0.1M NaOH over 30 minutes ($\geq$30mer) or 60 minutes ($>$30mer)). A standard assembly of double-stranded DNA (dsDNA) with the NP was accomplished by first deprotecting 1 nmol of the single-stranded $5'$-SH DNA with 50 mM Tris(2-carboxyethyl)phosphine hydrochloride (TCEP) in 20 mM PBS buffer pH 7.5 at RT for *geq* 45 minutes. The freshly deprotected DNA-thiol was desalted with a NAP-5 column, collecting the first 500 μL elute which contained 75% (750 pmol) of the total DNA loaded onto the column. The dye-containing complementary strand (590 pmol) was immediately added and the strands were annealed at 95°C for 2 minutes, cooled to RT for 2 minutes and then added to 20 nmol of dry H_2O-soluble NP. The mixture was vortexed and placed at 4°C in the dark for conjugation >24 hours. Successive ($\geq$2) ethanol precipitations were performed to purify unbound NP from the dsDNA-NP conjugate. The purified dsDNA-NP conjugate was reconstituted in 20 mM PBS pH 7.5 buffer and stored at 4°C in the dark.

2.2.3 Absorption and Photoluminescence

Absorption measurements were acquired on a Varian Cary 50 UV-vis spectrophotometer and photoluminescence measurements were acquired on a Varian Cary Eclipse Fluorescence spectrophotometer using Z-matched 50 μL quartz cuvettes. A typical quantum yield was calculated by measuring the absorption over the 200-800 nm range for both the sample described above and a control (dsDNA-dye without NP), keeping the peak of the dye absorption $\leq$0.1 A.U. Concentrations were kept very dilute (300 nM) to minimize effects due to self-absorption or Stern-Vollmer quenching. Continuous-wave photoluminescence (cw- PL) was first measured on the control strand, adjusting the sensitivity to maximize the PL signal. Under identical settings the PL intensity of the dsDNA-NP sample was then measured. Quantum efficiencies of quenching were determined *via* the following calculation:

$$E(I) = 1 - \frac{I_{sample}}{I_{control}} \cdot \frac{A_{control}}{A_{sample}} \tag{2.3}$$

where $E(I)$ is the quantum efficiency of energy transfer, $I_{sample,control}$ is the integrated intensity under the curve for the PL peak in energy, $A_{control}$ is the absorption of the sample at its absorption peak, and A_{sample} is the corrected absorption of the dye after subtracting out the contribution absorbed by the NP.

2.2.4 Lifetime Measurements

Lifetimes are acquired on dilute ($\sim$300 nM) samples using the output of a Nd:VO_4-pumped (Spectra-Physics Vanguard, 2 W, 532 nm, 76 MHz, 10 ps) R6G dye laser (Coherent 702-1). Cavity dumping of the dye laser to 1.9 MHz drops the pulse train to 1 pulse every 2 s. In the case of FAM the laser is frequency doubled for $\lambda_{ex} = 300$ nm, and used as is at $\lambda_{ex} = 600$ nm for Cy5. Samples were excited with <1 mW at a right angle geometry relative to a Chromex 500is 0.5 m imaging monochromator with 50 g/mm grating, 0.5 nm resolution. Output of the monochromator is focused into a Hamamatsu C5680 streak camera operating at 20 ns window (FAM) or 10 ns window (Cy5). Lifetimes are measured by binning intensity *vs* time for a 20 nm spectral range about the λ_{em} maximum for the dye. Lifetime quenching calculated

$$E(\tau) = 1 - \frac{\tau'}{\tau_{dye}} \tag{2.4}$$

was determined by comparing the measured decay rate for a NP-dsDNA-dye system (τ') vs the observed decay rate for the identical dsDNA-dye in the absence of NP (τ_{dye}).

2.3 Results

Figure 2.1 demonstrates the scheme of separating a donor fluorophore from the surface of a NP using three different lengths of dsDNA as a spacer, hereafter referred to as NP-dsDNAdye. The distance from the center of the molecule to the metal surface is estimated by taking into account the C_6 linkers and the size of the fluorescent dye. The C_6 linkers on either $5'$ end contribute flexibility to the system, but due to the persistence length of dsDNA[77, 78], and the fact that a d=1.5 nm NP is smaller than the 2 nm footprint of dsDNA it is very unlikely that the lengths of dsDNA used here would have the ability wrap around or interact with the gold NP. The C_6 chain on the dye will produce a cone of probability for the separation distance due to chain flexibility and tend to randomize the dipole vector relative to the nanometal surface so that the primary effect of the C_6 linker is insuring an isotropic distribution of electronic dipoles.

2.3.1 Lifetimes of Dyes Near 1.5 nm NPs

Figure 2.2 compares the lifetimes for both fluorescein FAM (2.2a) and Cy5 (2.2b) at all three dsDNA spacer distances from the NP surface. The intensities have all been normalized at the peak and are displayed on a logarithmic graph vertically offset for comparison. The lifetime for each dye clearly decreases with decreasing distance to the surface of the metal sphere, displaying single-exponential decay kinetics fit using a Levenberg-Marquardt algorithm to minimize the residuals about the form $I(t) = y_0 + I_0 e^{-kt}$. This is the first order rate law where y_0 is a linear offset, I_0 is the intensity at t=0, and k is the rate of decay where $1/k = \tau_{obs}$. These observations suggest that not only is the sample purified from free-dye but also that any variation in length caused by the C_6-spacer is not measurable for this system. All samples are compared to the appropriate dsDNA-dye strand in the absence of the NP (ie. FAM-15mer-NP is compared to FAM-15mer) however only a single dsDNA-dye strand is shown (top - blue) for comparison in Figure 2.2a, b. Using Eqn. 2.4 the quenching efficiencies as measured by lifetime are listed in Table 2.1.

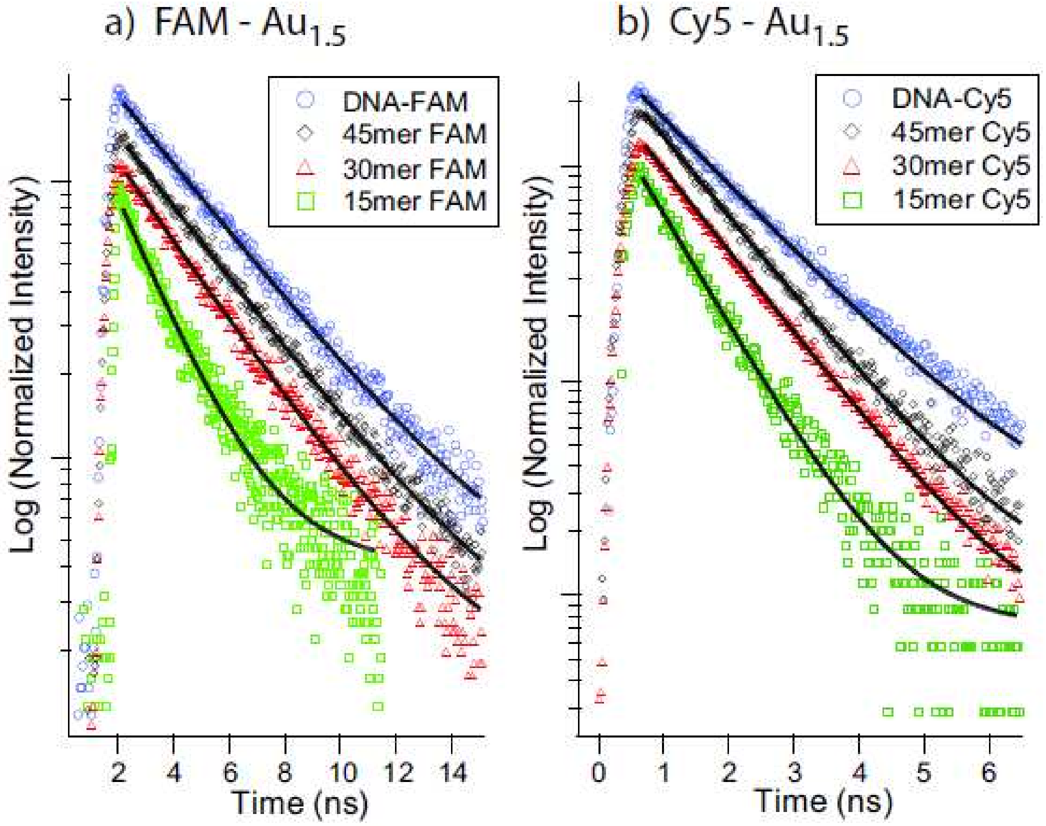

Figure 2.2: Lifetime quenching of (a)FAM and (b)Cy5 near a 2 nm Au NP as a function of distance from the surface .

2.3.2 Photoluminescence Characterization

In Figure 2.3, the cw-PL quenching of FAM (Figure 2.3a) and Cy5 (Figure 2.3b) as a function of dsDNA spacer length are compared. The quantum efficiency of quenching for each sample was measured by comparison against a control dsDNA-dye in the absence of NP, using Eqn. 2.3. Quenching efficiencies based on PL studies are tabulated in Table 2.1 *vs.* different spacer lengths.

2.3.3 Absorption Characterization

Figure 2.4a shows absorption spectra for NP-15mer dsDNA-dye, 15mer dsDNA-dye without NP, and the NP-15mer dsDNA-dye after subtracting the absorption arising from the NP. The absorption for the difference spectra is not well resolved at the higher wavelengths, probably a result of unsatisfactorily corrected scattering.

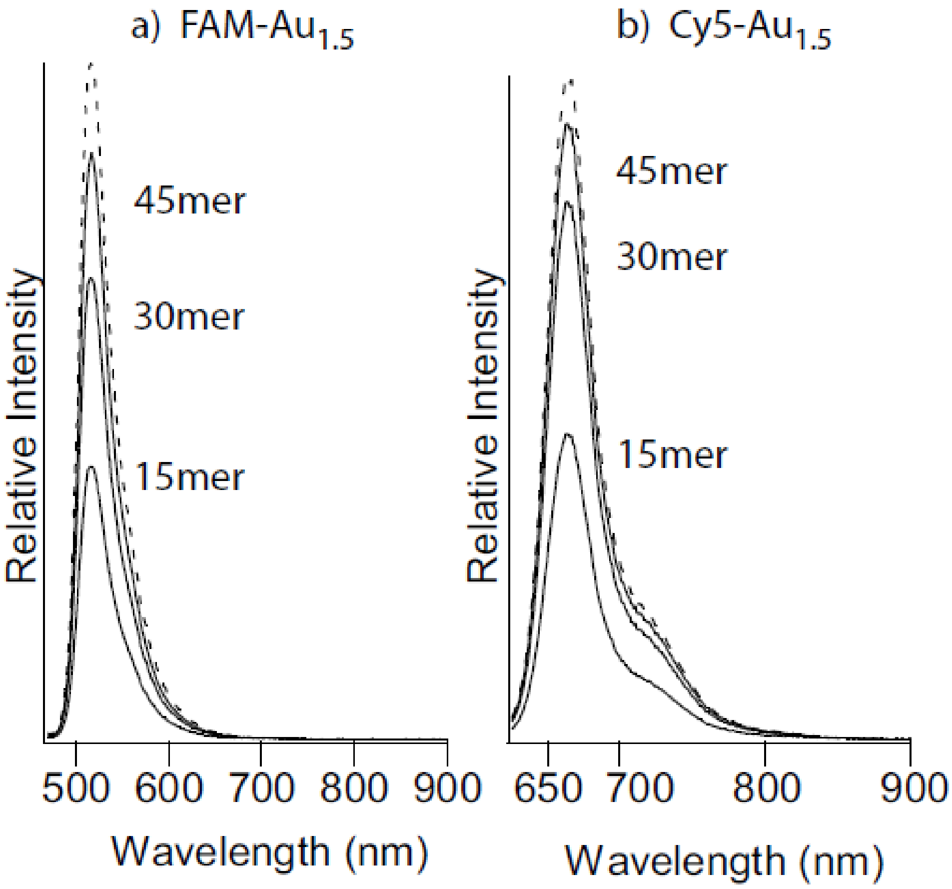

Figure 2.3: Photoluminescence quenching for (a)FAM and (b)Cy5 near a 2 nm Au NP as a function of distance from the surface of Au NP. The dashed line shows the comparative normalized intensity for the *control* strand for (a) FAM and (b) Cy5.

2.4 Discussion

2.4.1 Development of the model

A great deal of theoretical modeling[48, 65, 66, 67, 86, 87] (this list is far from complete) has probed the behavior of a dye in which the molecular dipole is damped by the response of a nearby metal surface. The quenching of the fluorophore intensity must be related to a through-space mechanism involving only the dipole of the donor and some electronic property of the gold NP, likely interactions with free electrons. The lack of an SPR band at the nanometal size used in this study suggests that the coherent behavior of electrons is diminished, negating the resonantly enhanced energy transfer suggested over the plasmon bandwidth[59, 81], but not the ability of a metal

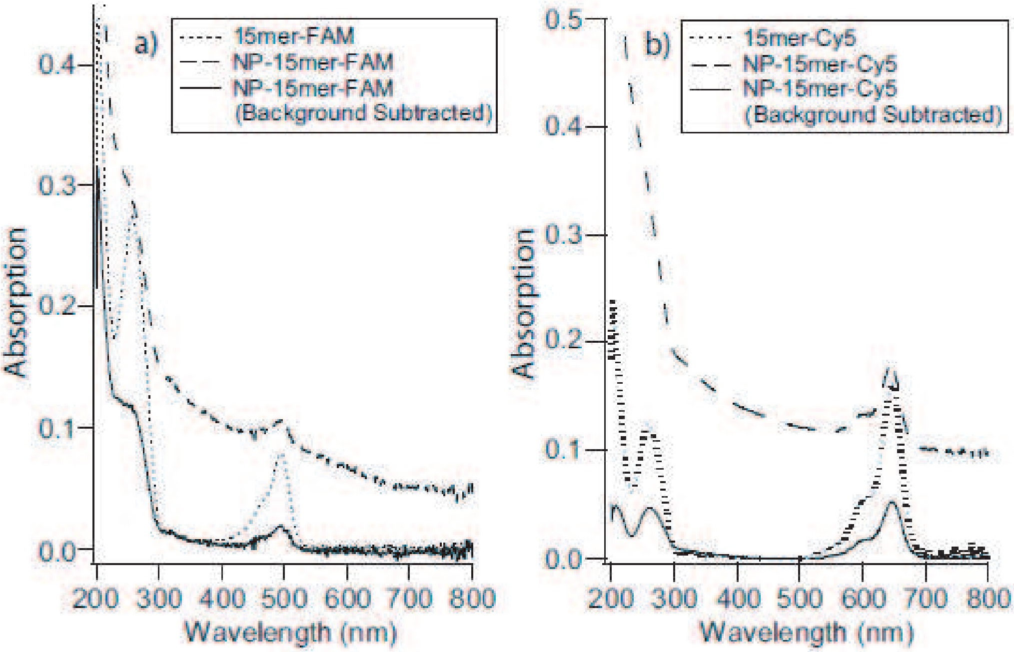

Figure 2.4: (a)Absorption and corrected spectra for the FAM-dsDNA-NP system and (b)Absorption spectra and corrections for Cy5-dsDNA-NP.

to accept energy. This is an important point because, although a larger sized NP may accept energy more efficiently, the smallest NP possible is the least intrusive for use of NSET as a molecular ruler or beacon in biological assays. Another important feature is the high curvature of a 1.5 nm gold NP suggests that all scattering events should be normal to the surface, which relaxes the dependence upon the overlap of projected dipoles. The Gersten-Nitzan models[59] which have been used for modeling dipole-dipole interactions with the plasmon of gold NPs seem to have fallen short in describing both the distance dependence and efficiency of dye-quenching[60, 82]. The model of Persson and Lang, however, concerns itself primarily with momentum and energy conservation in the dipole induced formation of electron-hole pairs and is useful for modeling this system. According to this model, the rate of energy transfer is calculated by performing a *Fermi Golden Rule* calculation for an excited state molecule depopulating with the simultaneous scattering of an electron in the nearby metal to above the Fermi level. However, in considering the conservation of momentum, the excitation of an electron-hole pair must coincide with an electron-electron, electron-phonon, or electron-surface potential scattering event. The Persson model[67] states that the damping rate to a surface of a noble metal may be calculated by:

$$k_{ET} = 0.3\frac{\mu^2}{\hbar}\frac{\omega_{dye}}{\omega_F k_F R^4} \tag{2.5}$$

Table 2.1: Measured values for the quenching efficiency for the 3 strands of dsDNA based on cw-PL spectra, $E(I)$, based on lifetime quenching, $E(\tau)$ and both the calculated and theoretical rates of energy transfer to the metal surface, (k_{ET}).

FAM

dsDNA	15bp	30bp	45bp
Distance(Å)	69	120	167
$E(I)$	0.69±0.07	0.27±0.06	0.22±0.04
$E(\tau)$	0.47±0.04	0.13±0.03	0.04±0.02
k_{ET}(Expt.)	2.55×10^8	4.9×10^7	1.3×10^7
k_{ET}(Theory)	4.3×10^8	4.7×10^7	1.2×10^7

Cy5

dsDNA	15bp	30bp	45bp
Distance(Å)	69	120	167
$E(I)$	0.54±0.06	0.19±0.04	0.07±0.03
$E(\tau)$	0.41±0.05	0.10±0.04	0.02±0.04
k_{ET}(Expt.)	4.87×10^8	8.5×10^7	9.72×10^6
k_{ET}(Theory)	3.3×10^8	3.6×10^7	8.6×10^6

which can be expressed in more measurable parameters through the use of the Einstein A_{21} coefficient[88]:

$$A_{21} = \frac{\omega_{dye}^3}{3\epsilon_0 \hbar \pi c^3}|\mu|^2 \tag{2.6}$$

to give the following rate of energy transfer, in accordance with Coulombs law ($\frac{1}{4\pi\epsilon_0}$):

$$k_{ET} = 0.225\frac{c^3}{\omega_{dye}^2 \omega_F k_F} \cdot \frac{\Phi_{dye}}{\tau_{dye}} \tag{2.7}$$

where c is the speed of light, Φ_{dye} is the quantum yield of the donor (FAM=0.8, Cy5=0.4), ω_{dye} is the angular frequency for the donor (FAM=3.8x10^{15} s^{-1}, Cy5=2.91x10^{15} s^{-1}), ω_F is the angular frequency for bulk gold (8.4x10^{15} s^{-1}), and k_F is the Fermi wavevector for bulk gold (1.2x10^8 cm^{-1}). The R_0 value is a convenient value to calculate for a dye-metal system, yielding the distance at which a dye will display equal probabilities for energy transfer and spontaneous emission. For the Persson model, the R_0 value may be calculated by:

$$R_0 = \left(0.225\frac{c^3 \Phi_{dye}}{\omega_{dye}^2 \omega_F k_F}\right)^{1/4} \tag{2.8}$$

We calculate R_0 values of 76.3 Å and 73.0 Å for FAM and Cy5 dyes, respectively. The theoretical plot overlay of the data in Figure 2.5 is shown for comparison.

It is important to note that this model does not concern itself with the reflected field from the surface, which makes it convenient for the case of a metal NP where, in accordance with Ruppins model[81], it is assumed that the reflected field is negligible and does not interfere with the dipole field. For the validity of this model, we assume that the dipole is a point dipole separated from a metal sphere by a rigid distance and that every fluorophore has an acceptor NP associated with it. This assumption is made practical in the material conjugation by saturating the dsDNA with acceptor NP and using less than a stoichiometric amount of donor-labeled strand. Monoexponential lifetimes support the assumption that every donor is located at a rigid distance from the acceptor. Alivisatos was successful in adapting the Persson model to describe energy transfer from biacetyl donors to a Ag(111) surface with good agreement to experimental data[89]. For their system, it was concluded that the dipole damping as a result of both bulk and surface electron scattering were important. However, a metal particle on the scale of 1.5 nm, being well below the electron mean-free path (∼430Å for gold[90]), will not show bulk electron scattering effects. Instead it is expected that the overwhelming majority of electron scattering events are associated with the surface potential. Figure 2.5 compares the experimentally observed quenching efficiencies of a 1.5 nm NP as measured by PL and calculated using Eqn. 2.3 and also as measured by luminescence lifetime using Eqn. 2.4. A theoretical curve calculated using Eqn. 2.8 is overlaid for comparison to theory. Although Eqns. 2.7 and 2.8 use bulk gold parameters, the model fits surprisingly well with the experimentally measured values, and particularly with the rates of energy transfer reported in Table 2.1. The photoluminescence characterization seems to overestimate slightly the theoretical quenching values, whereas the lifetimes are in excellent agreement with the model. Because the measurement of relative quantum efficiencies *via* PL spectra is prone to error in the form of fluctuations in lamp intensity or the ability to accurately measure absorption, the PL quenching efficiencies are considered less reliable than lifetime measurements. Fluorescence lifetimes avoid the accumulated error associated with the use of multiple instruments, which increases our confidence in their measurement. Lifetimes are very sensitive to the presence of quenching processes and give insight into the number of quenching processes taking place. The lifetimes measured here not only suggest that quenching is occurring due to a single energy transfer event, (decreased single-exponential lifetime), but also suggest that the slope of the theoretical curve may be correct. The absorption characteristics of gold NPs have been studied extensively and attempts to fit theory with experimental data have furnished a rich description of the electronic and optical properties of metal NPs. Attempts to model the absorption for gold NPs below 20 nm diameter, in particular the bandwidth and position of the SPR band, requires the incorporation of an enhanced surface potential scattering term in the Drude dipole approximation[75, 91]. Whetten was successful in adapting this model to calculate the absorption spectra of gold NPs from d = 1.4 - 3.2 nm where they advance the theory that thiol ligands donate electron density into the NP[63]. In this regard, the use of NPs as energy acceptors may actually enhance the quenching efficiency of a metal surface and explain the somewhat unexpected efficiency of quenching by a 1.5 nm NP. The increased electron density and surface scattering enhances the probability of energy transfer via the Persson model, accounting for the good agreement between the data shown here and the theoretical model.

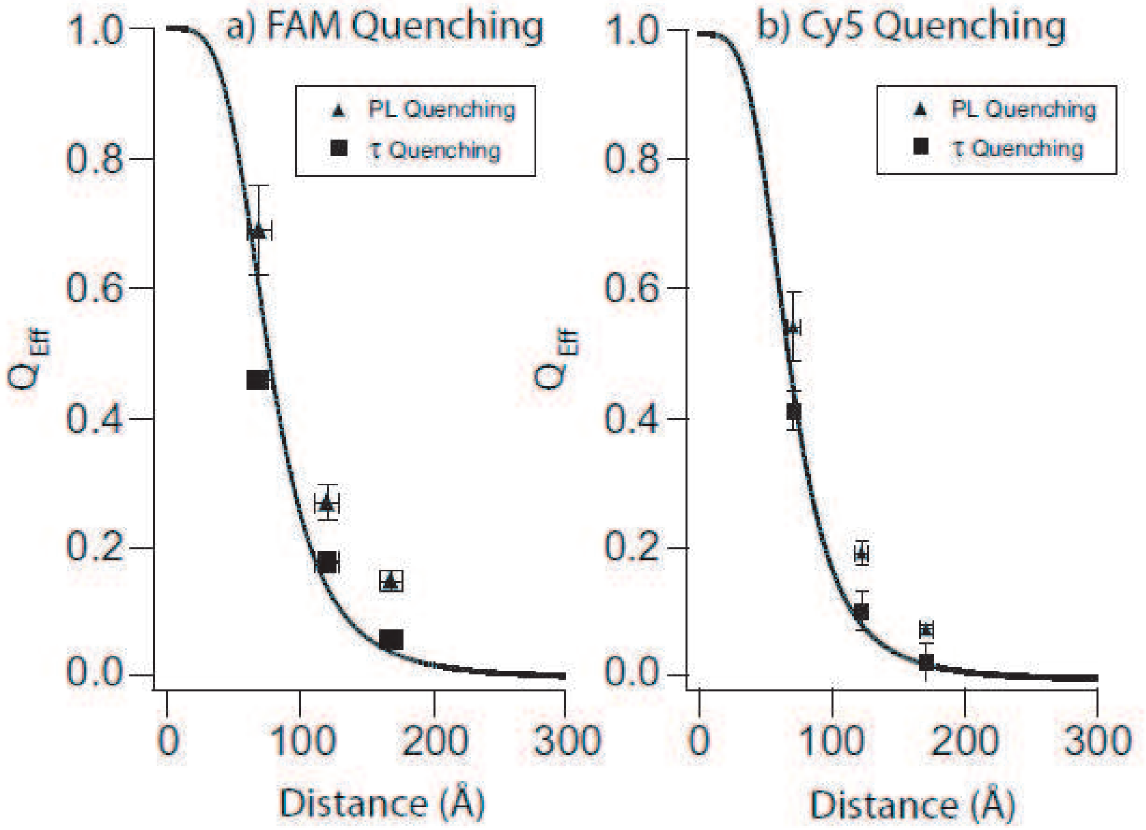

Figure 2.5: Quenching data for (a)FAM and (b)Cy5 based upon photoluminescence and lifetimes overlaid on top of a theoretical curve.

2.4.2 monitoring k_r

The observed quenching behavior of a molecular dye at a specified distance above a metal surface has been explained previously by a perturbed radiative rate[60]. Neither lifetime nor PL data alone will give evidence toward the true origin of the observed quenching because both can be explained by either the radiative rate or energy transfer models. An absorption experiment, however, will give insight toward the origins of this quenching phenomenon. Exclusion of the possibility of radiative rate (k_r) changes is garnered by considering the changes in the absorption intensity or oscillator strength (f) for the dye molecule upon binding the gold NP, since $k_r \propto f$[88]. The transition probability between states by the Einstein A_{21} and B_{12} coefficients relates the experimental absorption of an electronic transition to the oscillator strength and radiative rate for that molecule[73, 88]. Oscillator strength, f is directly related to the radiative rate, k_r through the relation[73, 88]:

$$k_r^0 = 3 \times 10^{-9} \overline{\nu_0}^2 \int \varepsilon d\overline{\nu} \cong \overline{\nu_0}^2 f \tag{2.9}$$

where $\overline{\nu_0}$ is the energy in wavenumbers corresponding to the maximum absorption, and ε is the experimental extinction coefficient. A controlled absorption experiment, therefore, gives the oscillator strength (f) for the dye upon appending the gold NP and is an independent measure of a changing radiative rate. Figure 2.4 shows the absorption for the 15 bp system where the sample absorption has been corrected for scattering at higher wavelengths and the absorptions of dsDNA-dye normalized at A_{260}. Normalization of the difference spectra at 260 nm, which arises predominately from the DNA absorption, allows direct comparison of the oscillator strengths for the FAM and Cy5 dyes at 490 nm and 650 nm, respectively in the absence and the presence of a NP. If the quenching efficiency shown in Figure 2.5 were related to changes in the radiative rate, then the experimental oscillator strength would be directly affected. However, changes in the oscillator strength were calculated to be 5-10% which does not account for the observed 50-70% drop in PL intensity, suggesting that the reduced quantum efficiency must be related to an energy transfer mechanism from the dye to the gold NP and not due to a changing radiative rate for this system.

2.5 Conclusion

In conclusion, three different lengths of dsDNA-dye, using two dyes of different energies were appended to 1.5 nm gold NPs as a means of measuring quenching efficiency of the fluorophore at discrete distances. Absorption data on the fluorophore is forthcoming in proving a mechanism which does not rely upon a changing radiative rate for this system. The quenching was measured by cw-PL and by picosecond lifetime spectroscopy to determine that the process of quenching is an energy transfer event and that it follows a $1/R^4$ distance dependence. The significance of a $1/R^4$ dependence upon energy transfer is realized when using NSET as a molecular ruler, because this means the measureable distance, ($\approx$ 20 nm) *via* this technique has been extended over 2× further than traditional FRET, ($\approx$ 10 nm.) The discrepancy between quenching efficiencies as measured by PL and lifetimes is most likely error due to instrumental inaccuracy in absorption/photoluminescence measurements.

CHAPTER 3

INVOLVEMENT OF THE LSPR SPECTRAL OVERLAP FOR ENERGY TRANSFER BETWEEN A DYE AND AU NANOPARTICLE

3.1 Introduction

During the past decade the development of new donors, acceptors, dark quenchers, and the use of 3-color energy transfer processes has expanded the applicability of optical probe methodologies to a wider range of biological problems [1, 15, 16, 18, 19, 20, 21]. The development of novel acceptors and donors in recent years has focused on the use of metal nanoparticles (NPs) as universal acceptors [28, 29, 30, 31, 32, 33, 34, 35, 36, 37, 38, 39, 40, 41] and quantum dots (QDs) as tunable donors [21, 22, 23, 24] due to the unique properties of these materials. QDs can be envisioned as effectively improved dye molecules that can be modeled as classical point dipoles (FRET-like) in an energy transfer assay and offer a tunable donor spectral range[21, 22, 23, 24]. Metal nanoparticles can act either as a radiative quencher or radiative enhancer depending on the particle size, shape, composition, and the distance between the donor and metal nanoparticle[16, 28, 56, 92, 93]. The competition between enhancement and quenching relates to the magnitude of the electric field at the particle surface and the dielectric dispersion for the materials[59, 66], which gives rise to quenching at small sizes and radiative enhancement at larger sizes[56, 93].

The unique properties of metal nanoparticles can be attributed to the absorption and scattering characteristics of the metal nanoparticle, typically referred to as the extinction cross-section[94]. The individual scattering and absorption terms relate to the real and imaginary components of the dielectric curve, resulting in the well known surface plasmon resonance (SPR) at 525 nm in gold nanoparticles. The SPR describes an induced oscillation of electrons at the surface of the metal nanoparticle. For ultra small metal nanoparticles the SPR will localize at the surface of the gold nanoparticle[95], resulting in the formation of a localized surface plasmon (LSPR) best described by a skin-depth oscillation of the electric field[62, 63].

Depending on the nature of coupling between the SPR oscillation and a dye in close proximity to the metal surface, the observation of radiative quenching or enhancement has been described by several groups[56, 59, 66, 67]. While substantial effort has been made to look at the enhancement effects, the nature and mathematical understanding of energy transfer quenching of a photo-luminescent dye by small gold nanoparticles has received less attention[60, 61]. Energy transfer leading to quenching of a dye at or near a small gold nanoparticle surface clearly occurs. However, whether the quenching relates to contributions from the interband transitions or the coupling to the LSPR is unclear[56]. Energy transfer processes must follow the *Fermi Golden Rule* and therefore have constraints with respect to the separation distance, orientation, and energy overlap between the donor and acceptor wavefunctions[59, 66, 67] . The spatial orientation terms depend on the description of the donor and acceptor dipole moment and optical properties, while the energy overlap is dependent on the donor photoluminescence (PL) and metal acceptor extinction spectra. When small Au NPs are used as acceptors, the spectral overlap function of interest is between the donor excited state and the frequency of localized surface plasmon resonance (LSPR) for the metal, which can be very broad[63, 95]. Chance, Prock and Silbey solved the *Fermi Golden Rule* problem for the interaction of an energy donor to a metal acceptor.

Recent results have shown that very efficient quenching of an excited state dipole near a 2 nm Au NP occurs with a R^{-4} distance dependence *via* the empirical nanometal surface energy transfer (NSET) mechanism[15, 16]. The empirical observation of a R^{-4} distance dependence between a dye and a gold nanoparticle (Au NP) is surprising. In fact, although the results have been experimentally reproduced by a large number of groups[29, 30, 31, 32, 33, 34, 35, 36, 37, 38, 39, 40, 41], quantum mechanical descriptions [96] within the postulates of electrodynamics theory for explaining the quenching mechanism have not reproduced the observed R^{-4} distance dependence. Although the theoretical prediction of Persson and Lang for energy transfer at a thin layer in a bulk material has been extrapolated to explain the observation of quenching of the photoluminescence of QDs[28] and molecular dyes[15, 16, 97] by 1.5 and 2.0 nm Au NPs, a full theoretical understanding of the process is still required; as the metal NP energy transfer is finding a broad applicability in biophysics[29, 30, 31, 32, 33, 34, 35, 36, 37, 38, 39, 40, 41] , and thus a more detailed analysis of quenching across the spectral overlap region for the Au LSPR and compilation of the NSET constants (R_0, range) is needed.

In this chapter, we demonstrate a direct correlation between the donor PL energy and the LSPR frequency for a 2 nm Au NP. The 2 nm Au NP is chosen to minimize molecular level contributions for the particle interacting with the DNA spacer, to ensure the LSPR description is appropriate, and to eliminate potential contributions from enhancement[15, 16, 97]. Analysis of the energy transfer efficiency curves for a wide range of molecular dyes with PL overlapping the LSPR frequency for a 2 nm Au NP (520 nm - 720 nm) allows a direct comparison of the experimental results to the theoretical predictions from classical FRET[5], Gersten-Nitzan (GN)[59], CPS-

Kuhn[48], and NSET[15, 16] models for energy transfer between a donor and Au NP. Comparison of the models indicates that the NSET model best describes the observed quenching behavior for a 2 nm Au NP, whereas CPS-Kuhn over-predicts the distance dependence, and FRET and GN under-predict the distance. The agreement of the NSET model may be rationalized if the LSPR oscillation can be approximated by a plane model. The results provide a much needed study to analyze the NSET mechanism for donor-Au NP energy transfer and provide constants for application of NSET as a tool in the biophysics molecular ruler toolbox.

3.2 Experimental

3.2.1 DNA Sequence and Au NP-Dye Conjugates

DNA of four different lengths (15bp (base pair), 22bp, 30bp and 45bp) were purchased from Midland with a 5′ C_6 amine modification for coupling Dye and the complementary strand with a 5′ C_6 disulfide (RSS) for coupling to Au NP surface. The Dye coupled ss-DNA used in the study have the following sequence (5′-3′),
15mer - Dye-C_6-CGTGTGAATTCGTGC
22mer - Dye-C_6-CGCCTACTACCCAGTCATCAGC
30mer - Dye-C_6-CGCCTACTACCGAATTCGATAGTCATCAGC
45mer - Dye-C_6-CGTTCCGTGTGCATACTGAATTCCGTGTTACTCTTGCCAACCTCG
where, Dye at the 5′ end can be AF488, AF555, AF594, AF647 or AF700, depending on the experiment. The respective complementary strands are (5′-3′),
15S - RSS-C_6-GCACGAATTCACACG
22S - RSS-C_6-GCTGACTGGGTAGTAGGCG
30S - RSS-C_6-GCTGATGACTATCGAATTCGGTAGTAGGCG
45S - RSS-C_6-CGAGGTTGGCAAGAGTAACACGGAATTCAGTATGCACACGGAACG
The disulfide at the 5′ of the complementary strand is deprotected using DTT to attach a BSPP stabilized 2 nm Au NP. The Au-Dye separation distance is 68.7Å, 92.5Å, 119.7Å and 170.7Å respectively, based on the Clegg model [79] from the Au NP surface to the center of the donor. Duplex DNA lengths less than 100 nm are assumed to be a rigid rod with only high frequency oscillations[77, 78].

Stoichiometric exchange is carried out on 2 nm BSPP passivated Au NP[16, 97] to promote a 1:1 DNA-dye to Au NP ratio *via* ligand place exchange reactions of the BSPP passivant on the Au NP at a 1:20 mole ratio of Au NP to DNA-dye. The final assemblies were purified by ethanol precipitation and analyzed by polyacrylamide gel electrophoresis (PAGE) to ensure single site modification and unbound dye removal.

3.2.2 Optical Measurements

Absorption and photoluminescence (PL) experiments were conducted on a Varian Cary 50 UV-Vis spectrophotometer and a Varian Cary Eclipse Fluorescence spectrophotometer respectively at 293±2 K in 50 μL cuvettes using 200 pmoles of double strand DNA (ds-DNA) in 20 mM PBS buffer, 0.1 M NaCl, pH7.5. Excited state PL lifetime measurements were carried out at $\lambda_{ex} = 290$ nm ($\leq$1 mW power) by frequency doubling the output of a R6G dye laser (Coherent 702-1), $\lambda = 590$ nm pumped by $NdVO_4$ laser (Spectra-Physics Vanguard, 2 W, 532 nm, 76 MHz, 10 ps) for AF488. The direct output of the R6G dye laser of $\lambda_{ex} = 560$ nm (<1 mW) was used for AF555, $\lambda_{ex} = 590$ nm for AF594 and $\lambda_{ex} = 620$ nm (<1mW) for AF647, AF700 and AF750. The output of the dye laser was cavity dumped at 1.9 MHz to optimize collection. The PL of the dye under excitation was directed to a Chromex 500is 0.5 m imaging monochromator at right angles which is focused into a Hamamatsu C5680 streak camera operating at a 10 ns window or 20 ns window depending on the native lifetime of the dye under observation. The experimental data represents 800,000 collection events. The lifetimes were fit to a single exponential function ($I(t) = Aexp^{-kt} + c$) using a linear least squares fitting routine.

The quenching efficiency (E) at a particular donor-acceptor (D-A) separation distance is calculated by measuring the emission intensity (I') and/or the lifetime (τ') of the dye with the Au NP appended to the ds-DNA (referred to as the *sample*) relative to the intensity (I_0) and/or lifetime (τ_0) of the dye coupled to duplex DNA when the Au NP is not appended at the complementary $5'$ end (referred to as the *control*). Comparisons to the lifetime of the dye on a single-strand DNA to the double strand DNA sequence allows correction for any dye-DNA interactions affecting the observed Φ_{em} or τ[73]. It is to be noted that DNA sequences are identical for each defined dye-Au NP separation distance regardless of the dye used.

3.3 Results

3.3.1 Experimental results for the dye to metal NP energy transfer

The distance dependence for energy transfer from a donor to a 2 nm Au NP was measured for a range of molecular dyes with PL between 520 nm and 780 nm. As shown schematically in Figure 3.1a, the separation distance is controlled by using a duplex DNA spacer (3.4 Å per base pair) in which the Au NP and dye are appended at complimentary $5'$ ends through a C_6 spacer attached to the phosphate backbone. Using the Clegg model[79], the distance of separation was defined from the center of the dye to the surface of the Au NP for all energy transfer models. Contributions from the spacer is included for the C_6 spacer[16, 97].

The dye PL spectra and the extinction spectrum for 2 nm BSPP passivated Au are shown in Figure 3.1b. The Au extinction spectra include contributions from the LSPR, the interband transitions, and ligand absorption at energies >350 nm. The dashed line in Figure 3.1b represents the LSPR contribution calculated by fitting the extinction spectra for a 2 nm Au NP using Mie theory and subtracting the ligand

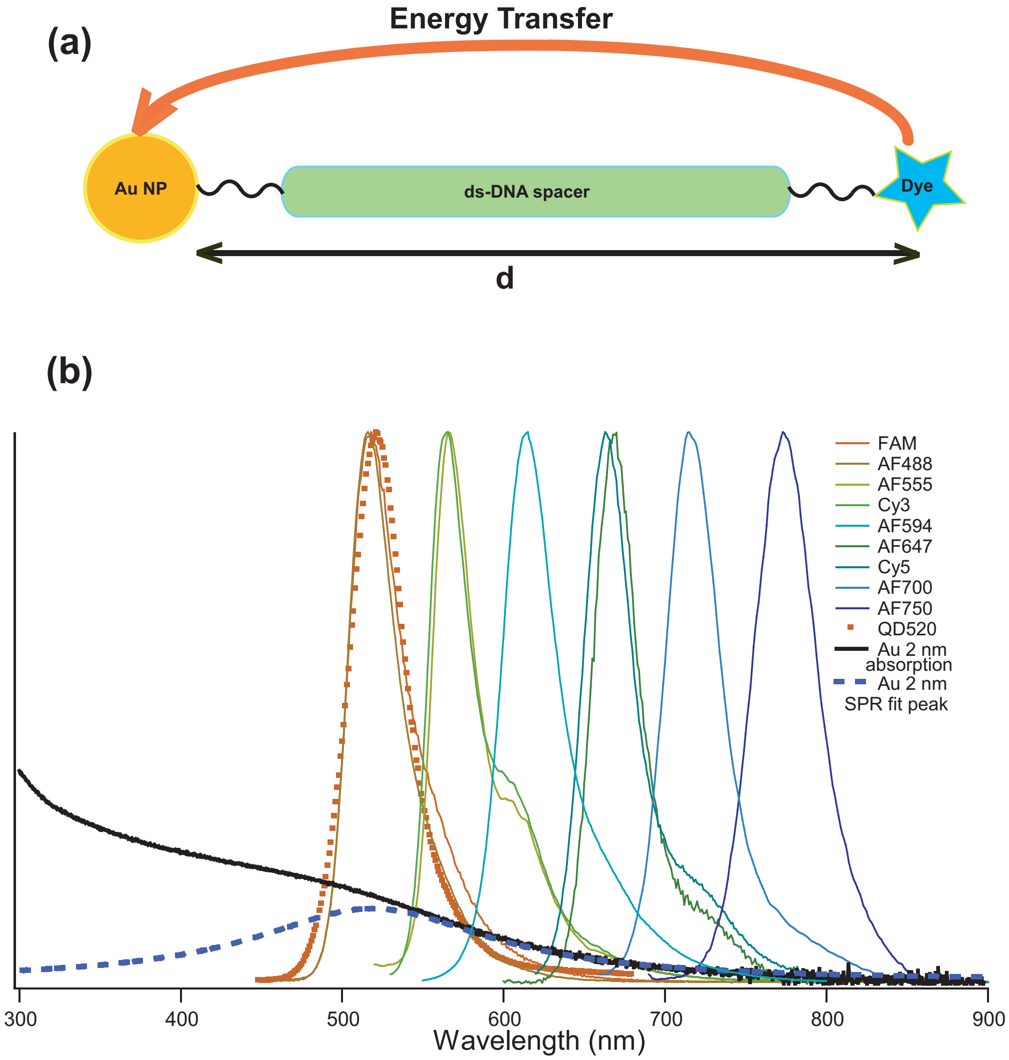

Figure 3.1: **(a)**Energy transfer schematic showing the assembly of DNA with a 2 nm Au NP appended at one end and a photo-luminescent dye at the complementary end, **(b)**Normalized PL spectra of the donors and the extinction of BSPP coated, water soluble 2 nm Au nanoparticles. The dashed line represents the calculated LSPR for a 2 nm Au NP.

absorption and higher order inter-band contributions to the extinction spectra.

The extinction spectra for bare Au NPs can be easily calculated applying the Mie's extinction cross section formula as discussed in Chapter 1. The calculated spectra for Au NPs of three different sizes is shown in Figure 3.2 by taking into account the change in the dielectric function of metal NPs at sizes smaller than $r =$ 10 nm. For a spherical Au NP, the extinction spectra can be interpreted by classical electrodynamics if we treat the Au nanoparticle as a Fermi gas or within the Drude

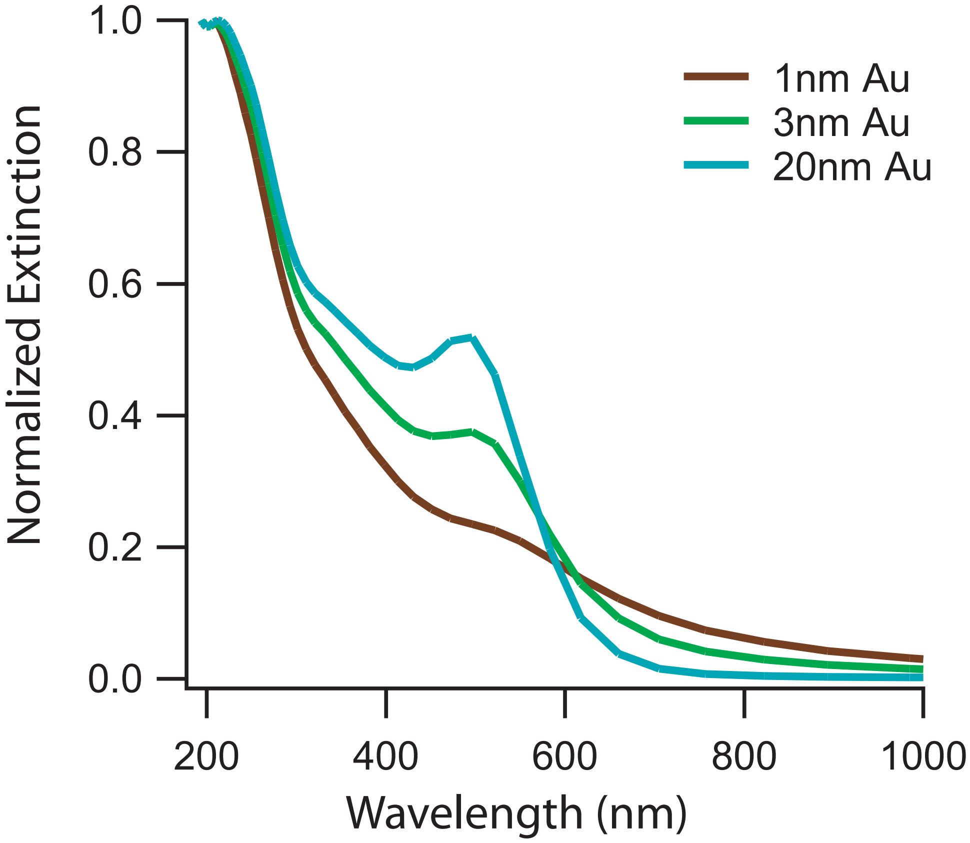

Figure 3.2: Theoretically calculated extinction for Au NPs of radius 1 nm, 3 nm and 20 nm applyng the Mie theory. The plots for 1 nm and 3 nm NPs were calculated by incorporating the size dependent changes in the dielectric function of the metal as described by Kreibig.

approximation by inclusion of the overlapping inter-band transitions (d $\longrightarrow$ sp)[62]. The inter-band transitions are assumed to be invariant with size, while the Drude contribution is size dependent [62, 63] as described in Chapter 1. For a spherical Au NP, the electron scattering term A is assumed to be isotropic and is fixed to a value of 1.0[62, 63]. Although changes in the value of A can lead to damping and frequency shifts in the LSPR, the spectra in Figure 3.1b and Figure 3.2 can be adequately interpreted using $A = 1$[63]. The change in the extinction spectra for a r = 1 nm Au NP by changing the value of A is shown in Figure 3.3. It is very evident from Figure 3.3 that changes in the nature of scattering processes expecially for small nanoparticles can drastically change theie extinction spectra.

The steady state photoluminescence (PL) and lifetime (τ) quenching data for the donors as a function of the distance of separation from the 2 nm Au NP are shown in Figure 3.2 and summarized in Table 3.1. Inspection of the data shows a clear distance dependence for excited state quenching for all measured dyes when the PL

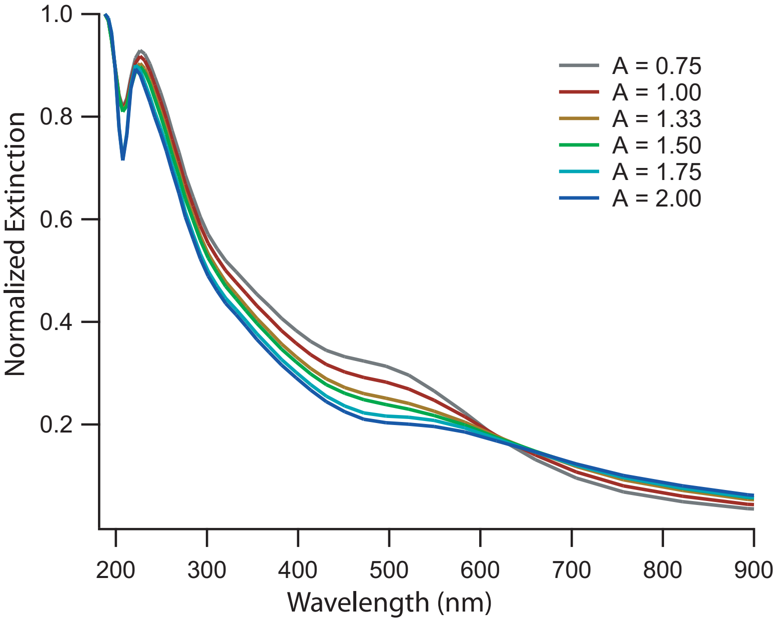

Figure 3.3: Theoretically calculated extinction for Au NP of radius 1 nm and varying the value of A, the scattering term which determines the changes in the total damping of electrons in the metal.

overlaps with the Au NP LSPR band. No quenching is observed for AF750, which lies outside the spectral region for the 2 nm Au NP LSPR. In the experiment, quenching data on AF594 and AF647 are shown at a single distance. The correlation between the observed fluorophore quenching and the energy of the discrete LSPR extinction features suggests that energy transfer from a point dipole to a Au NP surface occurs only within the limit of the LSPR frequency.

3.3.2 Theoretical considerations and comparison to experimental data

In a Au NP, the effect of the change in dielectric dispersion with size has several effects on the properties of the Au NP. In a 2 nm spherical nanoparticle the transverse and longitudinal plasmons lie at identical energies and more importantly, the absorptive cross section dominates the extinction spectra. In addition, due to the size-dependent change in dielectric constants, at 2 nm the scattering contribution is negligible and therefore enhancement should not play a significant role in the excited decay process for a dye near a metal nanoparticle. This implies that radiative quenching due to the absorptive component of the extinction cross-section will dominate the energy relaxation pathway for an excited state dye close to a metal nanoparticle surface[56, 71, 60]. Several energy transfer theories can be used to account for the observed quenching of the photo-luminescent donor by the metal nanoparticle, including

Table 3.1: Experimentally observed distance dependent quenching in normalized PL (I'/I_0) and lifetime τ' for AF488, AF555, AF594, AF647, AF700 and AF750. The PL wavelength (λ_{em}) and the natural lifetime (τ_0) for each dye is listed.

Dye	**Base Pairs**	**Distance (Å)**	I'/I_0	τ' **(ns)**
AF488	15	68.75	0.41	1.12±0.2
τ_0=2.6±0.03 ns	22	93.08	0.57	1.56±0.03
λ_{em} = 519 nm	30	118.1	0.73	2.00±0.02
	45	170.0	0.95	2.39±0.01
AF555	15	68.75	0.46	0.53±0.02
τ_0=0.94±0.01 ns	30	118.1	0.90	0.80±0.01
λ_{em} = 565 nm	45	170.0	0.99	0.89±0.2
AF594				
τ_0=4.45±0.02 ns	30	118.1	0.75	3.07±0.02
λ_{em} = 612 nm				
AF647				
τ_0=1.36±0.01 ns	30	118.1	0.88	1.19±0.02
λ_{em} = 668 nm				
AF700	15	68.75	0.70	0.70±0.02
τ_0=1.1±0.02 ns	22	93.08	0.90	0.97±0.01
λ_{em} = 719 nm	30	118.1	0.99	1.1±0.01
	45	170.0	0.99	1.1±0.02
AF750	24	77.3	0.95	0.56±0.02
τ_0=0.61±0.01 ns	35	94.3	0.93	0.58±0.01
λ_{em} = 780 nm				

FRET[1, 5, 6], NSET[15, 16, 20, 29, 30, 31, 32, 33, 34, 35, 36, 37, 38, 39, 40, 41], GN[59, 60], DMPET (Dipole to metal particle energy transfer)[28] and CPS-Kuhn [48, 66, 74] models. Each model has a set of limitations imposed upon it to account

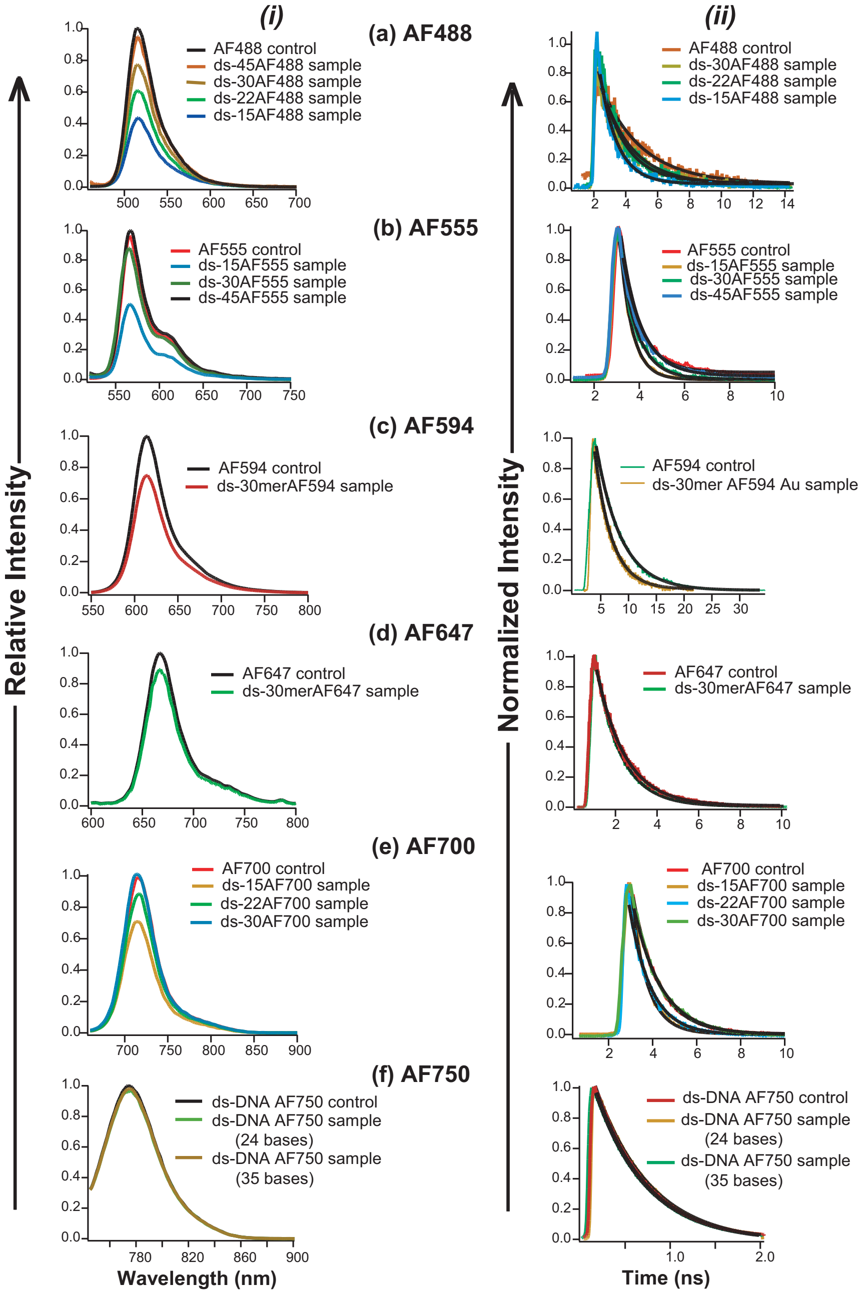

Figure 3.4: Distance dependent quenching of donor dyes by ***(i)***PL intensity and ***(ii)***lifetime analysis for **(a)**AF488, **(b)**AF555, **(c)**AF594, **(d)**AF647, **(e)**AF700, and **(f)**AF750.

for changes in the dielectric properties as the metal is reduced in dimension.

To fully interrogate the energy transfer quenching mechanism between a dye and a 2 nm Au nanoparticle, the properties of Au in the 2 nm size regime must be considered. For sizes approaching molecular clusters[62, 68], the metal is expected to lose its metallic properties, lose its ideal mirror behavior, localize the electron density at the surface of the NP and may be expected to behave as a single point dipole[68, 98]. Ideal mirror behavior depends on the metal's optical properties *viz* its complex refractive index, $\overline{n} = n_r + ik$ and the dielectric function, $\epsilon = \epsilon_1 + i\epsilon_2$. For a bulk metal, the perfect mirror behavior breaks down at frequencies close to the plasma frequency ω_p where the real part of the dielectric constant, ϵ_1 becomes positive and large and the imaginary component of the refractive index, k approaches zero. For very small clusters the ideal mirror behavior breaks down due to the size dependent nature of the dielectric function[62]. This is seen by solving the Kreibig expression for a 2 nm Au NP where a very large value of ϵ_1 and a near zero value of k results in the loss of the metal reflectivity[62, 64] and the breakdown of an ideal mirror assumption. It should be noted that the breakdown of the ideal mirror assumption does not imply loss of metallic behavior (i.e. Ohmic loss, polariton formation and strong dipole coupling within the metal)[68, 98]. Therefore, at small Au NP sizes the change in dielectric function will impact the nature of energy transfer between a Au NP and a dye.

The simplest mechanism to describe resonant energy transfer is Forster resonance energy transfer (FRET). FRET is a molecular level approximation treating the donor and acceptor as zero-dimensional resonantly coupled oscillators operating within the limit of weak coupling over distances in excess of the length of the dipole[5]. For Au NPs, the FRET approximation assumes the Au NP is molecular and no perturbation of the donor occurs by the Au NP. In the theory proposed by Gersten-Nitzan (GN), the Au NP has a strong electric field and the response of a single point dipole (donor) placed close to a metal nanoparticle is reflected in changes in the radiative and non-radiative rates of decay due to coupling of the donor to the metal's local electric field[59]. NSET assumes coupling between a point dipole and applies a thin film approximation to describe the 2-dimensional LSPR at the surface of the metal NP. In NSET, the metal oscillators are considered to be strongly coupled[67] as predicted by the Drude model, rather than a collection of independent oscillating dipoles or a single dipole in analogy to the FRET model. In CPS-Kuhn the dye molecule is treated as a classical linear harmonic oscillator which casts an image dipole onto the metal surface. The CPS-Kuhn model assumes the metal to be a perfect mirror in order to account for the behavior of a point dipole near the metal surface[48, 66]. The coupling of the donor dipole to the metal, which is described by treating the metal NP as an ideal mirror, leads to the potential for both enhancement and quenching depending on the projection of the electric field from the NP surface, which will be size dependent[56, 62, 99]. DMPET is a combination of FRET and NSET, and experimental results on a 2 nm Au NP indicates the NSET component dominates the experimental observation[28] and therefore is not discussed further as a separate theory. Although all these mechanisms can be used to approximate the energy transfer efficiency, each mechanism exhibits a limitation with respect to the accuracy of the fit.

For comparison of theory to experiment three terms will be important to extract the 50% quenching distance R_0, the power law (n) for quenching efficiency (E) and the total quenching range (10 - 90% quenching efficiency) for each theory. FRET, NSET, GN, and CPS-Kuhn mechanisms will have distinct distances over which they operate, size regimes for the metal that would be applicable, and constraints with respect to the nature of the dipoles involved.

The R_0 values for a specific dye-metal pair can be calculated for each theory. The R_0^{FRET} is[5]

$$R_0^{FRET} = \left[\frac{9000(ln10)\kappa^2 \Phi_{dye}}{128\pi^5 N_A n_m^4} J(\lambda) \right]^{1/6} \tag{3.1}$$

where, κ is the orientation factor, Φ_{dye} is the quantum yield of the donor, N_A is the Avogadro's number, n_m is the refractive index of the medium, and $J(\lambda)$ is the overlap integral between the donor emission and the acceptor absorption.

The value R_0^{GN} for a small metal nanoparticle can be expressed in terms of[59]

$$R_0^{GN} = \left[2.25 \cdot \frac{c^3}{\omega_{dye}^3} \cdot \Phi_{dye} \cdot r^3 \cdot \frac{(\epsilon_1 + 2)^2 + \epsilon_2^2}{|\epsilon_2|^2} \right]^{1/6} \tag{3.2}$$

where, ω_{dye} is the frequency of the donor dye, Φ_{dye} is the quantum yield of the donor, r is the radius of the metal nanoparticle, ϵ_1 and ϵ_2 are the real and imaginary components of the dielectric constant of the metal and c is the speed of light. This equation is derived under the assumptions that there is no change in the radiative rate of the dye molecule in the presence of the metal NP and therefore no enhancement effects.

The $R_0^{CPS-Kuhn}$ for the CPS-Kuhn model is described as[48, 66, 74],

$$R_0^{CPS-Kuhn} = \frac{\alpha\lambda}{n_m} (\overline{A}q)^{1/4} \left[\frac{n_r}{2n_m} \left(1 + \frac{\epsilon_1^2}{\mid \epsilon_2 \mid^2} \right) \right]^{1/4} \tag{3.3}$$

where, $\overline{A}$ is the absorptivity of the mirror $\overline{A} = \frac{4\pi kd}{\lambda}$ and $\alpha = (\frac{1}{4\pi})(9)^{1/4}$ for a dipole oriented perpendicularly to the metal surface while it takes a value of $(\frac{1}{4\pi})(\frac{9}{2})^{1/4}$ when the dipole is aligned parallel to the metal surface, λ is the emission wavelength of the donor dipole; ϵ_1, ϵ_2, and n_r, k are the real and imaginary components of the dielectric constant and the refractive index of the metal respectively, n_m is the refractive index of the medium; and d is the thickness of the mirror which in this case will be the diameter of the metal nanoparticle. In CPS-Kuhn, it is assumed that the dielectric constants are not size-dependent. However, as shown by Kreibig[62], a modification to the CPS-Kuhn theory incorporating the size dependence of the dielectric constants can be accounted for by substituting a size dependent term for the dielectric constants[62, 64, 99].

The theoretical value for the NSET R_0^{NSET} value is calculated using the NSET expression[16, 65, 66, 67]

$$R_0^{NSET} = \left(0.225 \cdot \frac{\Phi_{dye}}{\omega_{dye}^2} \cdot \frac{1}{\omega_F k_F} \cdot c^3\right)^{1/4} \tag{3.4}$$

where $k_F = 1.2 \times 10^8 cm^{-1}$ and $\omega_F = 8.4 \times 10^{15} rad/s$ are the constants for the metal acceptor derived from bulk gold; ω_{dye} and Φ_{dye} represent the angular frequency of donor emission and the quantum yield of the donor respectively and $c = 3.0 \times 10^8 m/s$ is the speed of light.

The efficiency of quenching (E) for steady state PL quenching can be related to the intensity efficiency, $E(I)$

$$E(I) = 1 - \left(\frac{I'}{I_0}\right) \tag{3.5}$$

or the efficiency for quenching of the excited state donor lifetime $E(\tau)$ the relationship can be written as,

$$E(\tau) = 1 - \left(\frac{\tau'}{\tau_0}\right) \tag{3.6}$$

A generic form of the efficiency of quenching allows the distance of separation between the donor and acceptor (R) and the R_0 value to be solved, leading to a power law distance dependence where,

$$E = \frac{1}{1 + (R/R_0)^n} \tag{3.7}$$

and the exponent n is dependent on the nature of energy transfer. The FRET and GN models predict a $n = 6$ distance dependent quenching efficiency, while NSET and CPS-Kuhn are expected to follow a $n = 4$ distance dependence. Solving the efficiency and R_0 values with respect to the distance predicts the range of quenching will be greatest for CPS-Kuhn and smallest for FRET.

An emprical fit to Equation 3.7 of the experimental intensity and lifetime quenching data (E_{NSET}^I, E_{NSET}^{τ}) *vs.* distance is presented in Figure 3.5*i* for each dye-Au NP pair. The plotted E curve in Figure 3.5*i* represents the the lifetime quenching data, which is believed to be more accurate as compared to intensity quenching data due to the ability to discriminate subtle changes in lifetime and eliminate unbound dye contributions. The average value observed for all donors that exhibit quenching yields an approximate value of $n = 4$, with experimental values of 3.6, 4.00, and 4.00 for AF488, AF555, and AF700, respectively. The value of $n \approx 4$ was observed previously for FAM ($n = 4.0$), Cy3 ($n = 3.9$), and Cy5 ($n = 3.8$). In Table 2, the values for each of the dyes, their quantum yield (Φ_{dye}), lifetimes (τ_0), angular frequencies (ω_{dye}), and the theoretical R_0 from the NSET theory are tabulated. Only single point distance measurements were carried out for AF647, and AF594 by lifetime analysis and therefore the R_0 values are calculated in the table by assuming a $n = 4$ for efficiency curve. Results for the fluorophores (FAM, Cy3, Cy5, QD520)[16, 20, 28, 97] are not shown in Figure 3.4 or Figure 3.5*i* but are included in Table 2 based on previously reported results.

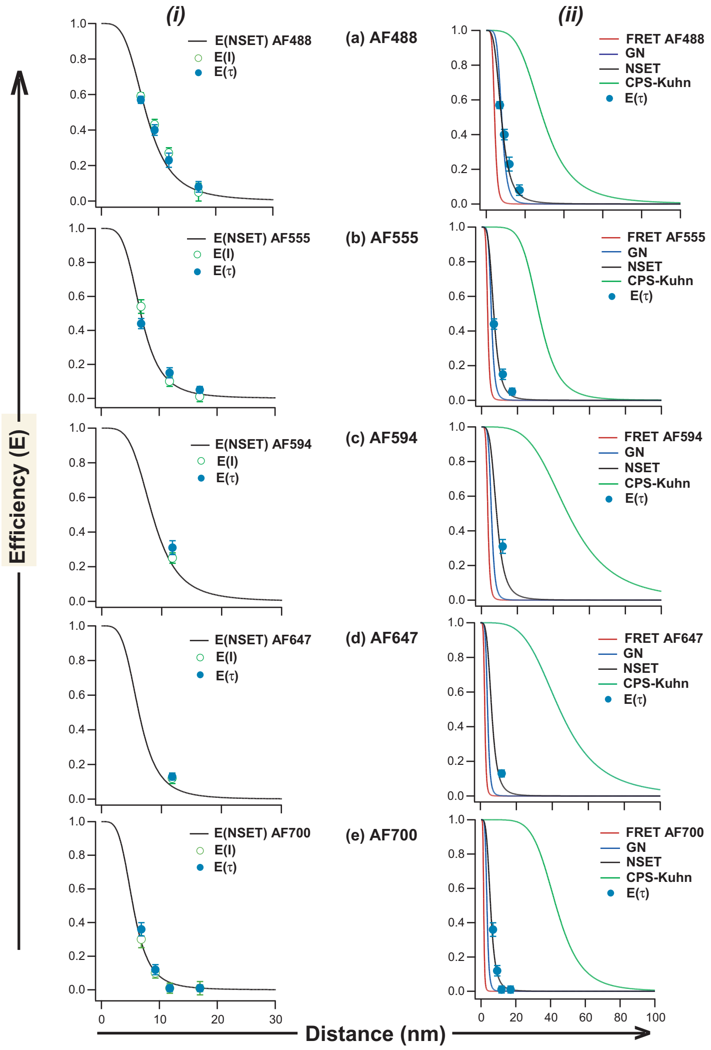

Figure 3.5: ***(i)***Efficiency curve fit of experimental PL and τ data for (**a**)AF488, (**b**)AF555, (**c**)AF594, (**d**)AF647 and (**e**)AF700, ***(ii)***Comparing the theoretical plots for three energy transfer mechanisms FRET, GN, NSET and CPS-Kuhn models for **a**)AF488, (**b**)AF555, (**c**)AF594, (**d**)AF647 and (**e**)AF700.

The results of the distance-dependent lifetime quenching assay can be compared to the theoretical plots (Figure 3.5*ii*, Figure 3.6) generated from the established FRET, GN, NSET, and CPS-Kuhn models by solving Equations 3.1-3.4. Comparison of the slope, R_0 values, and distance over which quenching occurs to the theoretically predicted efficiency (E) curves for FRET, GN, NSET and CPS-Kuhn show that the best experimental fit for the data is to the NSET model for all dyes that exhibit

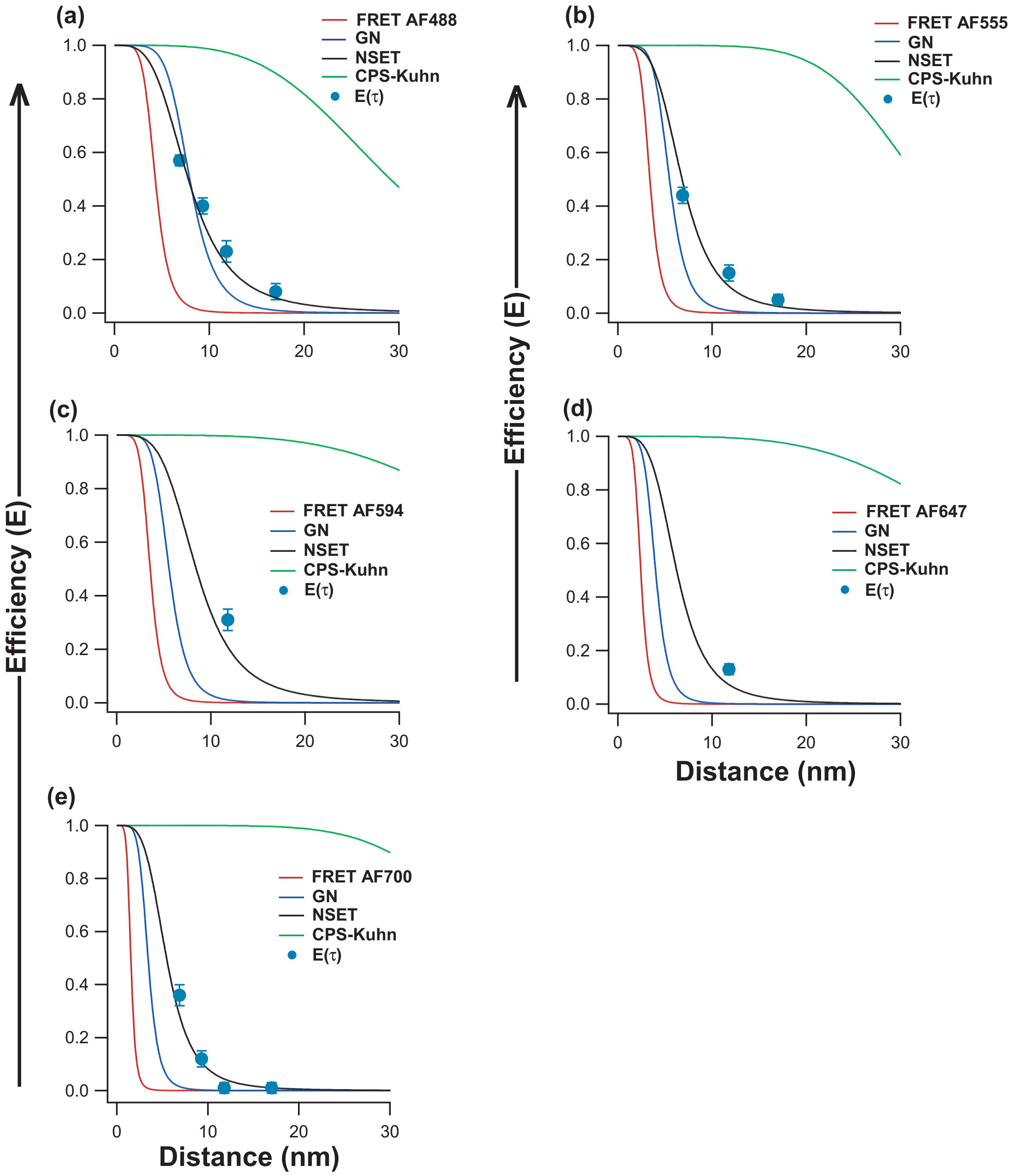

Figure 3.6: A zoom in of the efficiency curves for FRET, GN and NSET for (**a**)AF488, (**b**)AF555, (**c**)AF594, (**d**)AF647 and (**e**)AF700.

quenching. The FRET and GN models generally fail to predict slope, R_0 and range for the reported dyes. The CPS-Kuhn over predicts R_0 and range but accurately predicts the slope. Only NSET is able to fit slope and predict accurate R_0 values as well as the quenching efficiency range.

While the theoretical agreement is strongly supportive of the NSET model, an

Table 3.2: NSET and dye constants for donors to 2 nm Au NP energy transfer.

Dye	λ_{em} nm	ω_{dye} s^{-1}	Φ_{dye}	τ_0 ns	R_0 $(n = 4)$Å
FAM[16, 97]	520	3.63×10^{15}	0.9	3.1	80.2
AF488	519	3.63×10^{15}	0.8	2.6	77.9
AF555	565	3.33×10^{15}	0.4	0.9	68.2
Cy3[20]	570	3.31×10^{15}	0.2	1.9	57.6
AF594	612	3.08×10^{15}	0.8	4.5	84.5
Cy5[16, 97]	670	2.81×10^{15}	0.25	1.4	66.1
AF647[20]	668	2.82×10^{15}	0.2	1.5	62.4
AF700	719	2.61×10^{15}	0.1	1.1	54.6
AF750	775	2.43×10^{15}	0.1	0.4	-
QD520[28]	520	3.63×10^{15}	0.2	-	55.1

alternate explanation for the failure of the models to describe the experimental observation that must be discounted is the propensity for DNA to interact with the Au NP surface, which would modulate the actual experimental distance. DNA with length scales below 100 nm is generally considered to follow a rigid rod approximation for energy transfer studies[77, 78]; however, DNA interaction with large gold particles have been reported[100, 101]. Such molecular level interactions with the large surface area on a Au NP may give rise to an identifiable shift in the LSPR band extinction spectra that correlates with the number and type of molecular interactions present[95]. In addition, changes in the damping constant (A) could also arise if electron scattering is influenced by the DNA binding event. No shift in the experimental spectra is observed upon binding of the DNA to the 2 nm Au nanoparticle as seen in Figure 3.7*i*. The lack of a LSPR shift for the 2 nm Au nanoparticles is not conclusive evidence however, as it has been reported that the magnitude of shift is small for Au nanoparticles below 4 nm[95].

The 2nm Au NP in this study was designed to minimize non-specific interactions throug hthe passivation of the surface with the negatively charged $(2-)$ liagnd BSPP in order to increase electrostatic repulsion between the DNA phosphate backbone and the Au NP surface. Earlier studies have shown the use of BSPP is an effective approach to position the 2 nm Au NP distally on the DNA[102]. Although interactions can still arise *via* van der Waals forces or interactions between the phosphate groups on the DNA and the Au NP surface, it is believed the non-specific interactions are not contributing to the experimental observations. If an interaction with the Au NP surface was strong, then the predicted perturbation to the efficiency curve would be an offset to the distance and not necessarily a change in the slope of the efficiency curve. Alternatively, if we consider the surface curvature for the 2 nm Au NP and include a 1 nm spacer for the BSPP ligand then the length of DNA to wrap around a hemisphere is readily calculated as $l = \pi r$, for a BSPP passivated 2 nm

Au nanometal $l = 6.28$ nm. A strong interaction of DNA with the Au nanometal would therefore result in approximately 15bp interacting with the Au surface and a reduction in the distances calculated from the Clegg model of ≈ 12 nm. The distance is far too extreme for the longest DNA lengths to be accommodated. The presumption of weak Au NP-DNA interactions being the culprit for failure of the models is further supported by our observation that the NSET model is valid whether the dye modification is terminal[16] or internal independent of salt concentration[97], and the experimental agreement observed between optically measured RNA hammerhead structures and crystallographically determined distances when using a sub 2 nm Au NP NSET assay[20]. While it is still possible that a variable degree of interaction with the double strand may reduce this distance offset and produce an apparent slope change, we believe that Au-DNA interactions are minimal due to the size of the Au and negative charge of the passivated Au NP, thus the model failures are unlikely to

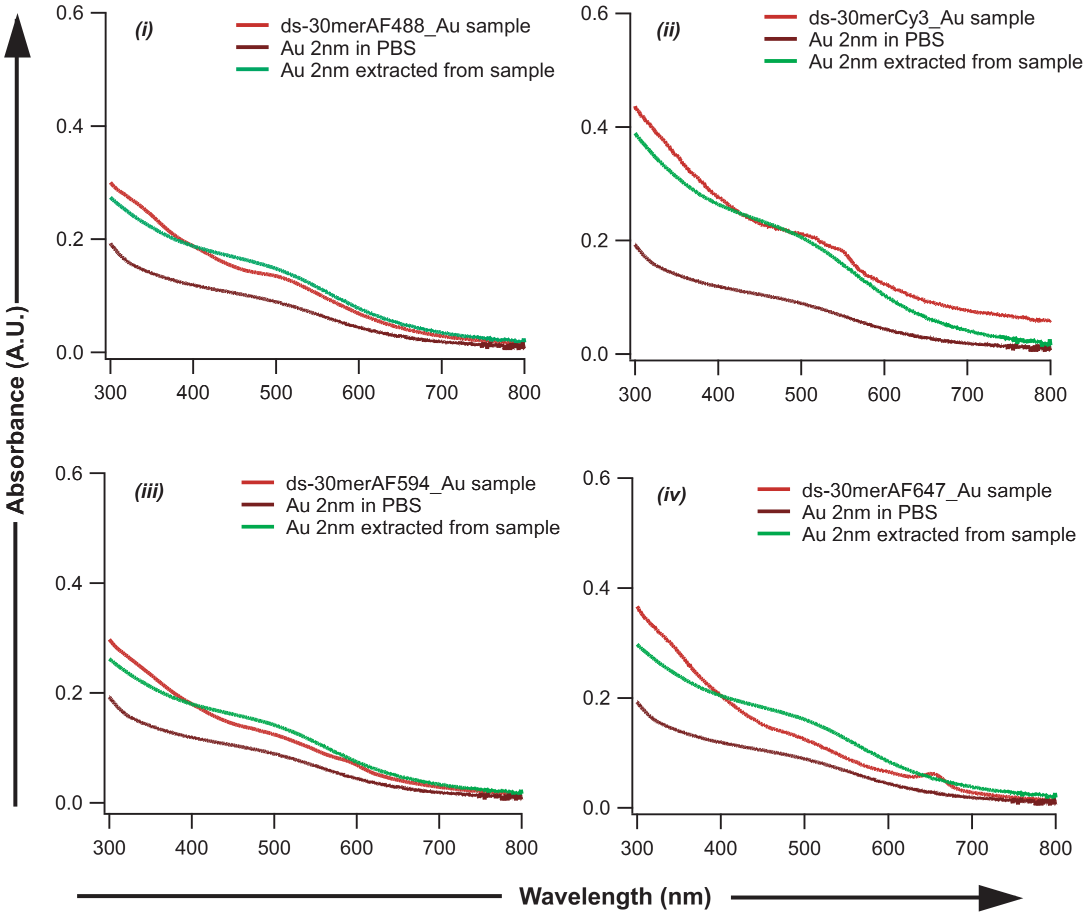

Figure 3.7: Binding of a ds-DNA does not cause any shift in the LSPR of a 2 nm diameter Au nanoparticle for (i)ds-30merAF488, (ii)ds-30merCy3, (iii)ds-30merAF594, and (iv)ds-30merAF647.

arise from non-specific interactions. Thus, the failure of the models to predict both, the observed slope and R_0 values across the whole spectral range must reflect the limits imposed on the mechanism to solve the *Fermi Golden rule* for these models, which do not adequately describe the coupling between a point dipole and a small metal NP.

3.4 Conclusion

Physically, it is not appropriate to define the 2 nm Au NP within the limits of the Persson-Lang SET (surface energy transfer) model, which requires the interface to be represented as an infinite plane of which a spherical metal particle is not. The strong correlation between the experimental measurements and the theoretical fits however suggest the Persson-Lang model adequately predicts the NSET observation. The correlation of theory and experiment may suggest that in general, a metal nanoparticle of a few nanometers in size can be described as a collection of strongly coupled surface localized dipoles that approach a hemi-spherical approximation of a plane, which would be consistent with the description for the LSPR in gold where, the surface of a Au NP consists of a localization of the electron density at skin depth of the nanoparticle[95]. In order to fully integrate the theory and experiment, further understanding of the changes in the quenching properties with Au NP size, and the importance of the admixture of the $d \rightarrow sp$ inter-band transitions needs to be interrogated. Regardless, it is clear a correlation exists between the magnitude of quenching and the spectral overlap for the Au nanoparticle LSPR and the dye photoluminescence energy.

The FRET and CPS-Kuhn models clearly fail to fit the experimental data, while the GN model only adequately fits AF488 but fails as the dye PL wavelength is shifted towards the lower energy of the LSPR. The correlation between the NSET model predictions and the experimental results strongly supports the Persson-Lang model as a basis for describing the energy transfer from the donor to the metal surface of the 2 nm Au NP. The correlation may only be applicable to metal nanoparticles where the absorption cross section dominates the extinction spectra and is expected to fail as the Au nanoparticle size is increased due to increasing contributions from the scattering cross section. Comparison of the experimental and theoretical results delineates the different mechanisms applicability to the experimental system under study and the limitations imposed. FRET assumes a point dipole for both donor and acceptor, which does not adequately describe the strongly coupled limit for dipoles in a Au NP. The limit imposed on the Gersten-Nitzan theory considers enhancement effects that can take place at the surface of a larger metal nanoparticle, where the electric field extends off the surface, thus the failure of the GN model can be attributed to the rapid damping experienced for the electric field at the surface of a 2 nm Au NP. The failure of CPS-Kuhn model can be attributed to the primary assumption that the Au NP can be treated as a perfect mirror.

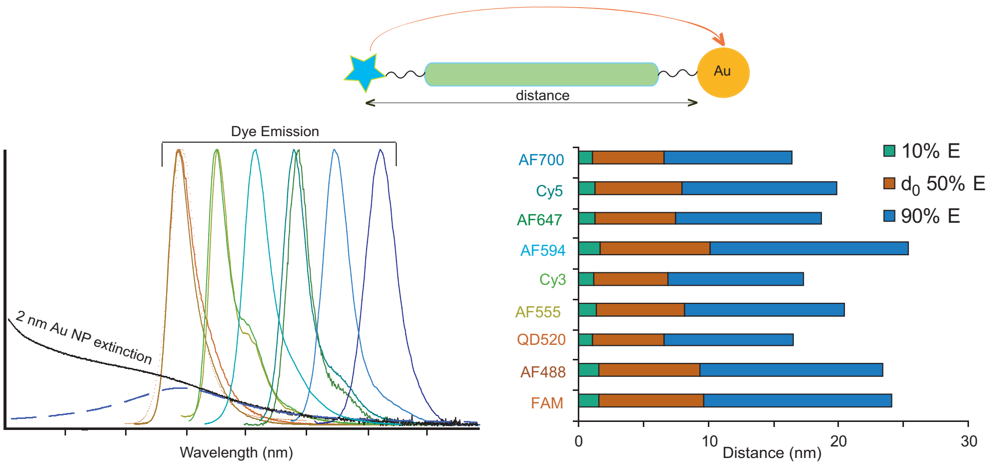

Figure 3.8: Scheme showing the system used to study the effect of LSPR overlap with the dye emission frequency and the respective critical distances and measurable distances(10%-90%E) in NSET for different fluorophores.

The results of this study provide a detailed compilation of experimentally determined R_0 values for dyes that overlap with the 2 nm LSPR band, providing a powerful collection of constants for application of NSET in biophysical studies (Figure 3.8). Although a theoretical basis from the first principles has not been solved, it is clear that the CPS-Persson model coupled to the LSPR frequency restriction inherent in NSET, predicts the R^{-4} distance dependence observed for all dyes within the LSPR frequency. Further studies are underway to mathematically correlate the empirical observation of NSET with the theoretical predictions for energy transfer at small Au NP surfaces.

CHAPTER 4

FLUORESCENCE QUECHING BY $D \rightarrow SP$ INTERBAND LEVELS IN 2NM GOLD NANOMETALS

4.1 Introduction

Au nanometals (Au NM) are a very important tool in the biophysical toolbox with applications ranging from resonant energy transfer (RET) spectroscopy to SERS (surface enhanced Raman spectroscopy), optical sensors, bio-diagnostics, DNA hybridization, SNP detection, and use in drug delivery platforms[51, 52, 53, 54, 55, 103]. The popularity of Au NM for applications in biotechnology stems from their ease of synthesis, surface functionalization, stability over a wide range of conditions, and the presence of a vibrant red color due to the surface plasmon resonance (SPR). The SPR or intraband transition in a Au NM is due to the oscillation of the *sp* electrons producing a strong electric field at the AuNM surface, which is extremely sensitive to chemical binding events, particle aggregation, and coherent wavefunction coupling leading to the observation of a competition between radiative enhancement and radiative quenching depending on the type, size, and shape of the nanometal[56, 95, 104, 105, 106, 107, 108, 109, 110]. Quenching of an excited state fluorophore is attributed to destructive interference between the excited state wavefunction and the size dependent intraband localized surface plasmon (LSPR) and the higher energy, size-independent interband ($d \rightarrow sp$) transition in Au[56, 62, 63, 105, 111]. The importance of the LSPR for quenching has already been studied in detail for a 2 nm Au NP and the quenching behavior has been found to follow the energy of the LSPR transition in this size regime[15, 16, 17, 20, 28, 105, 106]. Fluorophores whose emission does not overlap with the LSPR peak did not show any quenching while the one whose emission overlaps with the LSPR show a quenching behavior with a $1/R^4$ distance dependence as predicted by the NSET model[15, 16, 20].The interband transitions ($d \rightarrow sp$) which lie above the SPR band are strongly absorptive in nature and likely a major contributor to quenching of molecular PL for dyes in the far field. The quenching behavior of molecular dyes with PL at energies that overlap the interband transition is important since coherent coupling with the interband transition should be destructive leading to strong quenching of the excited state intensity, but has received only limited attention[105, 112].

In this chapter, the distance dependent quenching behavior for Alexafluor 350 (AF350) and Cascade blue (CCB) is probed by the $d \rightarrow sp$ interband transition in BSPP passivated 2 nm Au Figure (4.1). The photoluminescence (PL) of AF350 (λ_{em} = 440 nm) and CCB (λ_{em} = 420 nm) overlaps strongly with the interband transition and is higher in energy than the intraband transition in 2 nm Au (λ_{LSPR} = 525 nm). The use of 2 nm Au allows the interband effect to be probed without interference from the large scattering enhancement contribution from the intraband (SPR) that may be present in larger Au NMs, since 2 nm Au NM exhibits a weak, intraband contribution with no significant radiative enhancement observed[17].

4.2 Experimental

The AF350 coupled ss-DNA used in the study have the following sequence (5′-3′),
15mer - Dye-C_6-CGTGTGAATTCGTGC
22mer - Dye-C_6-CGCCTACTACCCAGTCATCAGC
30mer - Dye-C_6-CGCCTACTACCGAATTCGATAGTCATCAGC
45mer - Dye-C_6-CGTTCCGTGTGCATACTGAATTCCGTGTTACTCTTGCCAACCTCG
where, Dye = AF350 at the 5′ end. The respective complementary strands are (5′-3′),
15S - RSS-C_6-GCACGAATTCACACG
22S - RSS-C_6-GCTGACTGGGTAGTAGGCG
30S - RSS-C_6-GCTGATGACTATCGAATTCGGTAGTAGGCG
45S - RSS-C_6-CGAGGTTGGCAAGAGTAACACGGAATTCAGTATGCACACGGAACG

The Dye-dsDNA-Au assembly was prepared and purified as mentioned earlier. The complementary strands were annealed together by heating them in 20 mM PBS 100 mM NaCl pH7.5 buffer to >95˙C for 2 min and then cooling to room temperature. The annealed ds-DNA was treated with DTT to deprotect the thiol bond ans passed thorugh a NAP-V column to reomove the excess DTT. The deprotected ds-DNA is instantly mixed with a solution of BSPP coated 2 nm Au nanoparticles such that the DNA:Au ratio was 1:20. The unreacted Au was removed by ethanol precipitation.

The steady state experiments were conducted on a Varian Cary Eclipse Fluorescence spectrophotometer respectively at 293K±2 K in 20 mM PBS buffer, 0.1 M NaCl, pH7.5 with λ_{ex} = 350 nm for both AF350 and Cascade blue. The lifetime for the dyes was measured by using λ_{ex} = 290 nm ($\leq$1 mW power) by frequency doubling the output of a R6G dye laser (Coherent 702-1), λ = 590 nm pumped by $NdVO_4$ laser (Spectra-Physics Vanguard, 2 W, 532 nm, 76 MHz, 10 ps.

4.3 Results and Discussion

The coherent coupling of the wavefunction for a dye excited state with the dispersion curve for the scattering and absorption cross sections of a metal can be understood by considering the phase and energy of the electronic transitions of a metal (Figure 4.1). The optical properties of the dye-AuNM complexes are shown in Figure 4.2. AF350 has an absorption maxima $\lambda_{abs} = 350$ nm, an emission maxima $\lambda_{em} = 440$ nm and CCB has $\lambda_{abs} = 400$ nm and $\lambda_{em} = 420$ nm. The extinction spectra in Au is comprised of a size dependent SPR band (intraband transitions) and a size independent $d \rightarrow sp$ (interband) transitions. The interband and intraband contributions to the extinction spectra for a 2nm AuNM is shown in Figure 4.2. Using a Mie scattering approximation for a spherical AuNM, the extinction spectra can be divided into scattering and absorption terms reflecting the real and imaginary dielectric dispersion curves for the transitions. The observation of enhancement *vs.* quenching depends on the coherent coupling (destructive *vs.* constructive) of the excited state of the dye molecule to the nanometal interband and intraband transitions[16, 20, 56, 105]. The interaction will be coherent for coupling with the scattering (real) component of

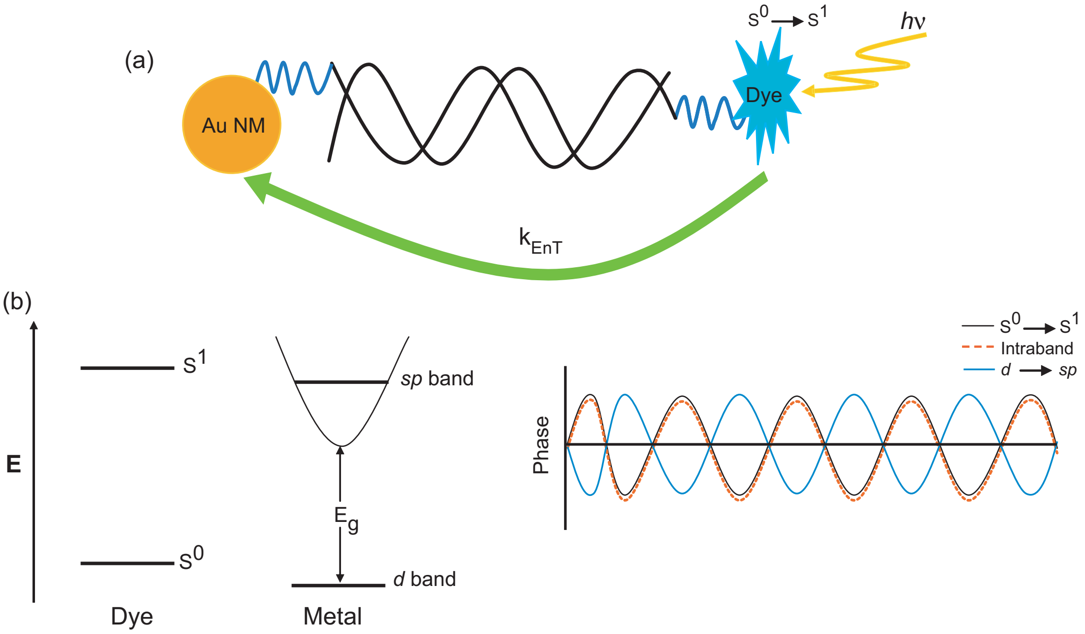

Figure 4.1: Schematic showing the contruction of the material and the energy levels in the donor dye and acceptor metal. The interaction between the donor dye oscillation and the intraband SPR is of contructive nature. The interbad term shows a destructive interaction with the dye oscillation and hence a complete quenching is observed.

the extinction spectra and destructive for the absorption (imaginary) component in the extinction spectra[105]. Ignoring the ligand contributions ($\lambda_{BSPP} = 250$ nm) to the observed extinction spectra for a AuNM, the intraband ($\lambda_{SPR} = 525$ nm) and higher lying interband contribution to the total dielectric function of the metal, can be written in terms of the real and imaginary contribution, such that, [62, 63]

$$\epsilon = \epsilon^{intra} + \epsilon^{inter} = [(\epsilon_1^{intra} + i\epsilon_2^{intra}) + (\epsilon_1^{inter} + i\epsilon_2^{inter})] \tag{4.1}$$

The real component, ϵ_1 is scattering while the imaginary component, ϵ_2 is absorptive. The value of ϵ^{intra} is calculated for a spherical particle using the Mie approximation assuming the Drude model where the free conduction electron cloud vibrates resonantly with the incident field against a positive background allowing ϵ^{intra} to be written as[105, 111],

$$\epsilon^{intra} = 1 - \frac{\omega_{p,eff}}{\omega(\omega + i\gamma_{eff})} \tag{4.2}$$

where $\omega_{p,eff}$ is the effective plasma frequency and γ_{eff} is the damping rate for the collective oscillations (plasmon). The ϵ^{intra} equation can be expressed in terms of a size dependent function following the approach of Kreibig, as described previously[17, 62]. Kreibig showed γ_{eff} is size dependent resulting in broadening of the SPR band and not loss of the SPR feature for a 2 nm Au (Figure 4.2)[17, 62, 63]. The intraband is highlighted in Figure 4.2 fit as a Lorentzian function (dotted red line).

The dielectric function for the interband transitions can be expressed such that[105, 111]

$$\epsilon^{inter} = K \int_0^\infty dx \frac{\sqrt{\hbar x - E_g}}{x} \left[1 - \mathbf{F}(x, \Theta)\right] \frac{(\omega^2 - x^2 - \gamma_{ee}^2 - 2i\omega\gamma_{ee})}{(\omega^2 - x^2 - \gamma_{ee}^2)^2 + 4\omega^2\gamma_{ee}^2} \tag{4.3}$$

where γ_{ee} is the interband damping rate, $\mathbf{F}(x, \Theta)$ is a measure of the electron occupation number of the d band, and K is the oscillator strength of the interband transitions. The interband contributions shown in Figure 4.2 in dotted blue line strongly overlap the emission profile for the dyes in the study. Projection of the d and sp atomic levels in k-space indicate the d levels are dispersionless, while the sp orbitals form a parabolic conduction band with E_g being defined as the energy gap between the d and sp dispersion curves Figure 4.1. The dispersionless inner-shell d-atomic levels leads to a size independent behavior in AuNMs for systems >1 nm.

In Figure 4.3, the time resolved lifetime and steady-state intensity quenching for the AF350 Au-DNA conjugate for 15bp (68.75Å), 22bp (93.08Å), 30bp (118.1Å), and 45bp (170.0Å)) is shown. In addition, the lifetime and intensity quenching is also shown for 30bp (118.1Å) for the CCB Au-DNA conjugate. The choice of only one length for CCB reflects the observation of no substantial distance dependence over the DNA lengths measured for the AF350 sequences. The measured lifetimes and intensity quenching data are compiled in Table 4.1. Control over the dye to AuNM separation distance is achieved by appending the dye to the distal end of double stranded DNA through a 5′-phosphate modification. For the studies, DNA is assumed to conform to a rigid rod approximation over the experimental length scale, allowing the separation distance to be calculated from the 2 nm Au NM surface to the center of the dye using the Clegg model (assuming no tilt of the DNA relative to the Au NM surface)[79].

The experimental results on AF350 and CCB in Figure 4.3 show >90% quenching in both the time-resolved and steady state results irrespective of the dye-AuNM separation distance. The experimental quenching analysis is compiled in Table 4.1 and generated by comparison of the steady state emission intensity and time-resolved lifetime of the complete assembly, *sample* (Au-dsDNA-Dye) with dsDNA-Dye, *control* to calculate the efficiency of energy transfer by emission ($E(I)$) and lifetime ($E(\tau)$). The steady state and time resolved experiments were conducted in dilute solutions to eliminate the effects of self-quenching. The measured lifetimes from the time-resolved data are single exponential and have no contribution from free dye based on the lifetime analysis. The observed quenching is not due to free gold in the solution since

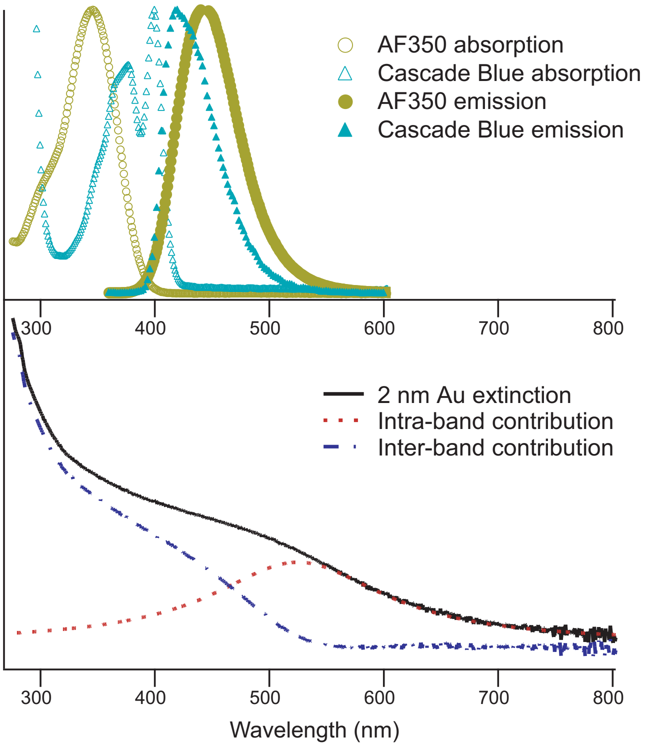

Figure 4.2: Absorption and emission spectra of AF350 and Cascade Blue (CCB) with a overlapping extinction of a 2 nm Au nanometal. The intraband SPR and the interband $d \rightarrow sp$ fits are also shown. Both the dyes exhibit have their λ_{abs} and λ_{em} higher than the LSPR frequency for Au NP which is at 525 nm.

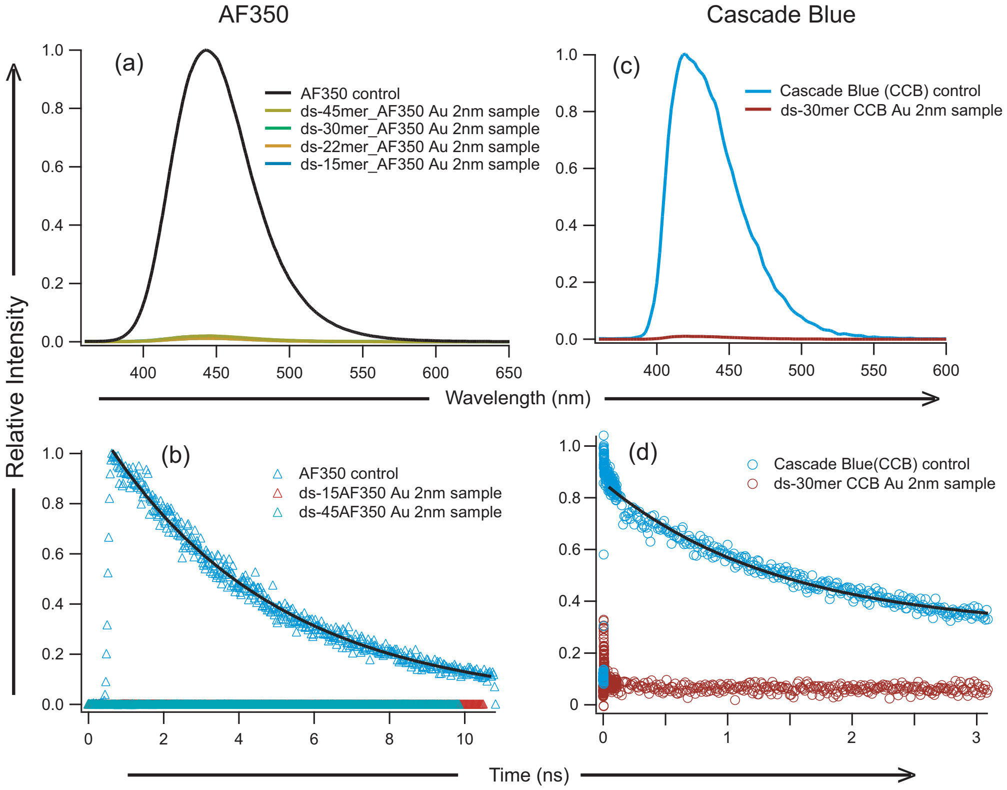

Figure 4.3: Distance dependent quenching of AF350 and Cascade Blue by a 2nm Au NP. A >90% quenching is observed at all distances for both the dyes in the steady state as well as the lifetime experiments.

addition of 2 nm Au to a solution containing the ds-DNA with the dye molecule appended produces no observable effect on the measured lifetime when the DNA is not coupled to the AuNM surface. The strong quenching observed in both the time-resolved and steady state plots indicates radiative enhancement does not contribute to the experimental measurements for AF350 and CCB for the 2 nm AuNM. Comparison of the results to our earlier study on LSPR intraband effects on quenching indicate the >90% quenching at all experimentally measured distances is surprising and likely imply coupling of the excited state wavefunction of the dye and interband transitions are different than coupling to the intraband transition.

A plot of the quenching data for AF350 and CCB versus distance is shown in Figure4.4 along with the theoretical NSET and the Kuhn model predictions confirm the failure of the NSET model to predict quenching behavior for dyes that overlap the interband transition in the Au NM. The experimental observation of >90% quenching is inconsistent with the NSET model, but lie within the expected quenching behavior for the Kuhn-model. The lack of agreement with the NSET model for AF350 and CCB is not surprising as the NSET theory is based upon Persson and Lang's model[67],

Table 4.1: Experimentally observed distance dependent quenching in normalized PL (I'/I_0) and lifetime τ' for AF350 and Cascade Blue (CCB). The PL wavelength (λ_{em}) and the natural lifetime (τ_0) for each dye is listed.

Dye	**Base Pairs**	**Distance (Å)**	$E(I)$	$E(\tau)$
AF350	15	68.75	0.95±0.01	-
τ_0=4.2±0.2 ns	22	93.08	0.96±0.02	-
λ_{em} = 440 nm	30	118.1	0.94±0.01	-
	45	170.0	0.94±0.03	-
CCB				
τ_0=3.5±0.3 ns	30	118.1	0.95±0.01	-
λ_{em} = 420 nm				

which assumes a Drude behavior for the electrons in the Au NM and therefore is not applicable to the interband coupling problem. The previous observation of NSET behavior for dyes coupled to the LSPR transition is consistent with the NSET model, as the intraband transitions arise from the Drude-like behavior of the conduction electrons[17]. The results are comparable with the Kuhn model[48], which is not Drude limited incorporating both the in-phase and out-of-phase component of the metal extinction spectra. Although the agreement over the limited distance range is good, the distance range measured does not allow absolute confirmation of the fit and further studies are necessary. Due to the limited distance range for maintaining a rigid rod approximation for DNA (<100bp, 360 Å including the C_6 spacers) coupled to the ability to prepare synthetic DNA above 60bp, the lengths required to map the full Kuhn-like behavior exceed the experimental range for DNA based distance control in this study.

4.4 Conclusion

The results of the study elucidate the contribution of the interband $d \rightarrow sp$ transitions on the experimental observation of excited state quenching of dyes near the surface of a nanometal. The significant increase in quenching range for dyes overlapping the interband transitions corroborates the suggestion that quenching behavior at metal surfaces may be attributed to destructive interference between the dye oscillator and the metal interband transition and not contributions from the intraband[56, 105, 113]. For molecular dyes coupled to a 2 nm AuNM that overlap the interband transition, it is clear the quenching behavior is predicted by the Kuhn model and exhibits different quenching characteristics than the intraband which follows the NSET model. Alternative explanations for the observation may include photo-induced electron transfer from the dye to the Au NM[114], although the distances over which these experiments were conducted do not support such a mecha-

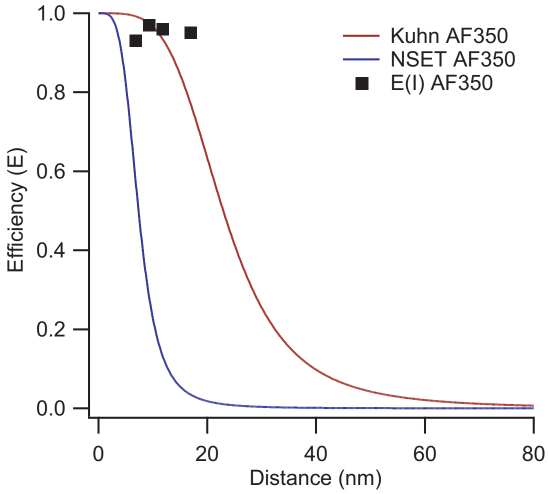

Figure 4.4: Comparison of the Kuhn and NSET theories with the experimental data $E(I)$.

nism, or bending of the DNA to shorten the experimental separation distance for the dye to the Au NM, although this has not been observed in our previous studies[17].

The study expands the understanding of phase-dependent coherent coupling of excited state wave packet to predict the quenching behavior for a molecular dye wavefunction in the far-field of a nanometal and will impact applications of Au NMs to radiative engineering in nanometal systems. The results provide a much needed analysis of the contributions of the interband coupling to a dye over controlled separation distances. The experimental observation of $> 90\%$ quenching of dye PL up to 170Å suggests that molecular beacons can be constructed from dyes overlapping the interband transition of the metal and potentially W (tryptophan)[37, 40] for structural analysis in large proteins or bio-complexes. Extrapolating the study to larger metal sizes and longer separation distances using PEG spacers are underway. As a function of nanometal size, it is expected the interband transition will dominate the quenching although enhancement effects for dyes lying close to the onset of the SPR may arise.

CHAPTER 5

SIZE DEPENDENCE OF ENERGY TRANSFER FROM FLUORESCENT DYE TO AU NANOPARTICLE

5.1 Introduction

Forster resonance energy transfer (FRET) describes a 0-d point dipole / point dipole problem. The debate over whether or not it is accurate to refer to a NP at 2 nm diameter as a "metal" is ongoing[63, 75, 92, 115], however the effect of bringing such a particle into the proximity of an excited dye molecule is clear: the NP affects the quantum efficiency of emission by introducing a competetive rate of energy transfer into the NP. Because the quenching process is most likely a direct result of free electron interactions with the dipole field of the emitter, we realize immediately that by changing various parameters of either the dye or the NP we should be able to "fine tune" the efficiency of NSET. As shown from the NSET rate equation:

$$k_{ET} = 0.225 \frac{c^3}{\omega_{dye}^2 \omega_F k_F d^4} \frac{\Phi_{dye}}{\tau_{dye}} \tag{5.1}$$

the rate of energy transfer is dependent upon properties of the metal (ω_F, k_F) and upon the frequency, quantum yield, and lifetime of the donor dye. We may anticipate that, aside from varying properties associated with the dye, changes to the NP acceptor in terms of metal type, NP shape, or especially size should also have a drastic effect upon the behavior of the system. Figure 5.1 demonstrates the size scale of differently sized gold nanoparticles as compared to DNA.

The smallest particle at 2 nm, is minimally invasive when considering integration with biological systems, containing ≈250 atoms and a Molar Mass of 20,500 g/mol. A 6 nm gold particle, however, is four times larger with ≈6700 atoms and a Molar Mass of 1.3x10^6 g/mol. At a diameter of 6 nm, a particle has become the size and mass of a medium sized protein which means that it is no longer a passive observer, but is better considered as a very dense beach ball dominating the movements of any appended bio-molecules. In terms of NSET efficiency, however, the move to 6 nm diameter means significant increase in the density of free electrons and thus its interactions with light. As has been discussed earlier[62, 17], nanometal size plays an important role in terms of enhanced density of free electrons, scattering atinterfaces and coherent plasmon formation over a diameter of 2 nm. As such, the increased density of states and polarizability of such a nanoparticle suggests that it should behave as a much more efficient energy sink for a nearby oscillating electric field.

Considering the same issue from a geometric point of view, the increased cone angle swept out by a 6 nm sphere relative to a point dipole at a fixed distance has also changed drastically, which can be viewed using Förster terminology as an increased dipole projection operator, κ^2. For example, a point in space at a separation distance of 7 nm (15 bp dsDNA) from a 2 nm diameter particle carves out an angle of approximately 24°, (see Figure 5.2). If the height of the NP changes to 6 nm at the same distance, the angle θ now becomes $\approx$81°, or an increase of almost four times. At 13 nm diameter, the angle becomes $\approx$124°, or an increase of 5 times, which is starting to give a good approximation to a planar surface, ($\approx$90°). Figure 5.2 demonstrates the effect that different NP sizes will have in terms of geometry for a dipole at a fixed separation distance.In this study, we will examine the effects that a changing NP size will have upon the efficiency of energy transfer from organic dyes.

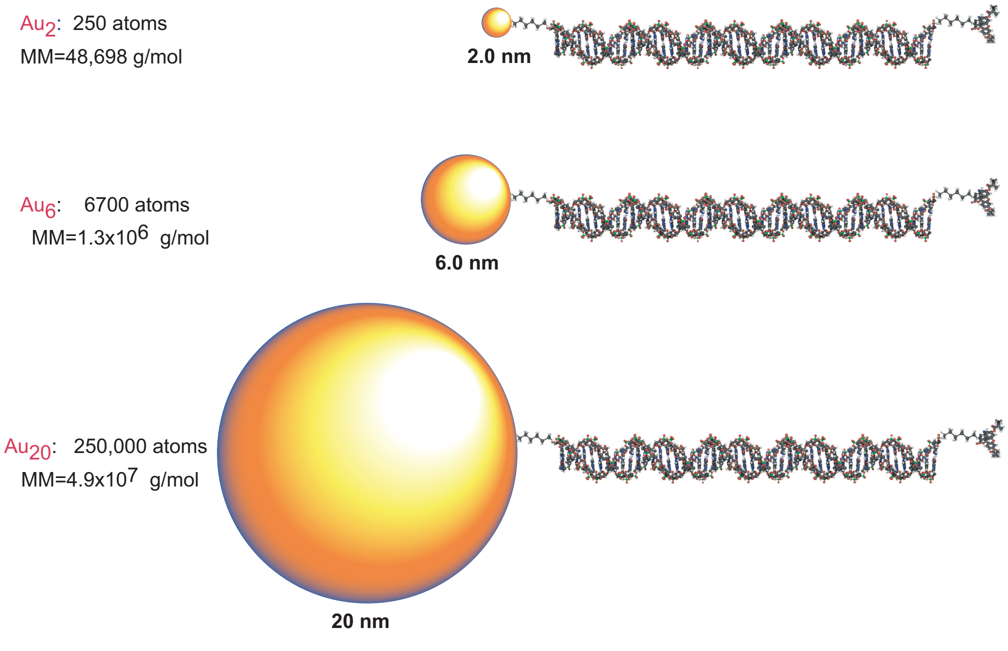

Figure 5.1: Graphic illustration of 45 bp dsDNA (∼17 nm) appended to gold NPs of various sizes. The 2 nm NP is the smallest and least invasive. The 6.0 nm NP is a force to be reckoned with and the 20 nm NP begins to approximate a surface.

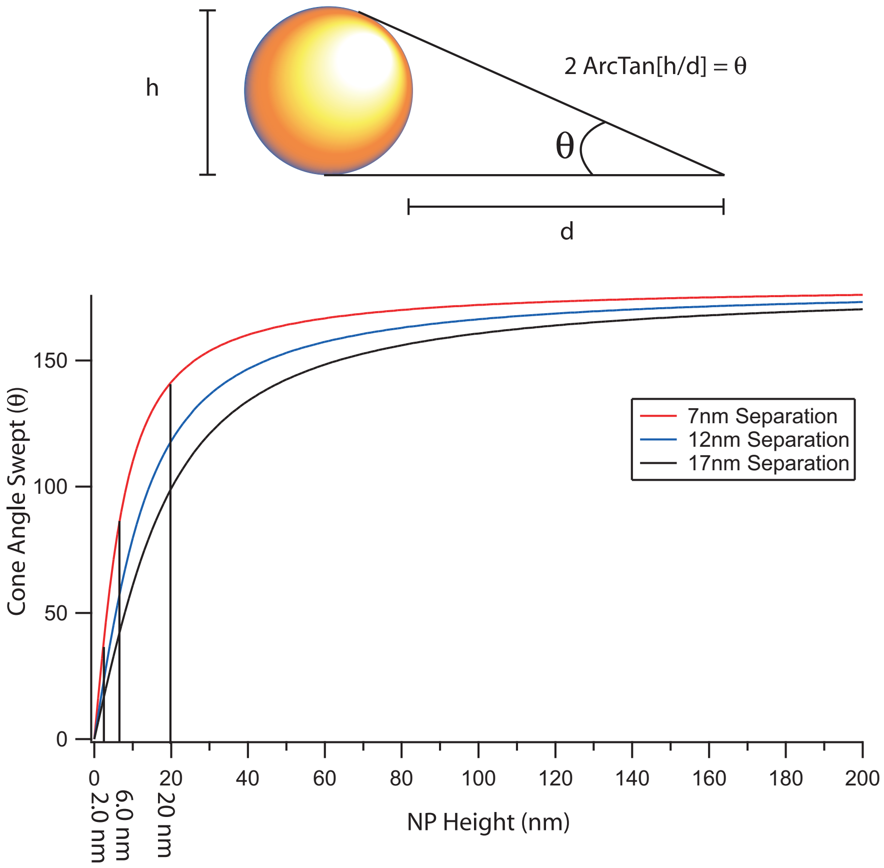

Figure 5.2: NPs of different diameters will sweep out a varying cone angle relative to a fixed point dipole. The effect of NP size on dipole projection can be estimated in this manner. The above calculations were performed for fixed separation distances of 7, 12 and 17 nm, which corresponds to 15, 30, and 45 bp dsDNA spacer lengths, respectively. The cone angles swept out by 2, 6, and 20 nm nanoparticles are shown.

5.2 Experimental

5.2.1 Au Nanoparticle Synthesis

Citrate capped gold nanoparticles (Au NPs) with an average diameter of 4 nm and 6nm were synthesized by standard literature techinques[50] following a reduction of $HAuCl_4$ using tri-sodium citrate and tannic acid. Citrate capped Au nanoparticles with an average diameter of 20 nm were purchased from Sigma-Aldrich. All the citrate capped colloidal Au NPs were ligand exchanged with Bis(p-sulfonatophenyl)phenylphosphine dihydrate (BSPP) by stirring them overnight with BSPP. Purification of the 4 nm and 6 nm colloidal NPs is accomplished by adding dropwise an aqueous solution of 6 M NaCl until the solution begins to turn a dark purple. The salt concentration screens repulsive charge between NPs inducing a Van der Waal's attraction between neighboring particles and causing an aggregation of NPs accompanied by a massive red-shift of the SPR band to lower energy. Once the mixture has begun to precipitate, centrifugation for 1-2 minutes allows easy decanting of the supernatant. Successive precipitations ($\geq$3 times) effectively purifies the solution from BSPP ligand, which can be qualified based on a strong absorption peak near 290 nm. Purification of 20 nm dots did not require addition of NaCl. Centrifuging the colloidal solution at 13000 rpm for $\sim$10 minutes settles the dots at the bottom and the excess ligand can thus be reomoved. The 20 nm dots easily go back in solution.

TEM measurements (Figure 5.3) displays particles with an average diameter of 4.36±0.66 nm (4 nm), 5.99±0.41 nm (6 nm) and 19.7±1.09 nm (20 nm). A UV-Vis of all the different sized Au NPs is presented in Figure 5.3d.

Once the NP diameter is known, it is possible to calculate an extinction coefficient by the following equation, which is based upon the emperically obtained relationship published by El-Sayed *et al.*[92]:

$$\varepsilon(d) = 10^{1.0643 \cdot Log_{10}[3/2\pi d^3]+4.0935} \tag{5.2}$$

In this equation, d is the diameter of the gold NP in nanometers and the extinction is given in M^{-1} cm^{-1} at the peak of the plasmon resonance, (typically 525 nm). The molar mass for a particle can also be obtained by incorporating the molar volume of gold (V_m=10.215 cm^3 mol^{-1}) into the geometrical equation:

$$MM_{NP}(d) = \frac{0.5\pi}{3}\frac{N_A \cdot d^3}{V_m} \cdot MM \tag{5.3}$$

where N_A is Avogadro's number, MM is the molar mass of the pure metal element, (Au=197 g/mol), and d is the diameter of the diameter of the NP in cm. It should be noted that this equation has been expressed in generalized terms and can therefore apply to any pure metal NP. Note also that by using the root form of the equation, one can calculate the number of atoms contained in the particle volume as a function of NP diameter:

$$Atoms(d) = \frac{0.5\pi}{3}\frac{N_A \cdot d^3}{V_m} \tag{5.4}$$

Using Eqns. 5.2,5.3, and 5.4 the molar extinction coefficient, molar mass and the number of atoms in each of the nanoparticles can be calculated (Table 5.1).

5.2.2 dsDNA - Nanoparticle Coupling:

Complementary DNA strands were purchased with either 5′-C_6-Dye (Dye = FAM)or 5′-C_6-SSR already HPLC-purified from Midland, Certified Reagent Co. The Dye strands have the sequence (5′-3′):
15mer - Dye-C_6-CGTGTGAATTCGTGC

30mer - Dye-C_6-CGCCTACTACCGAATTCGATAGTCATCAGC
45mer - Dye-C_6-CGTTCCGTGTGCATACTGAATTCCGTGTTACTCTTGCCAACCTCG
60mer - Dye-C_6-CGTTCCGTGCACATACTATCCACTCTTAGCGAATTCATCCACATAAT CTCTAGTATCTGC
The resepctive complementary thiol strands have the folowing sequences (5′-3′):

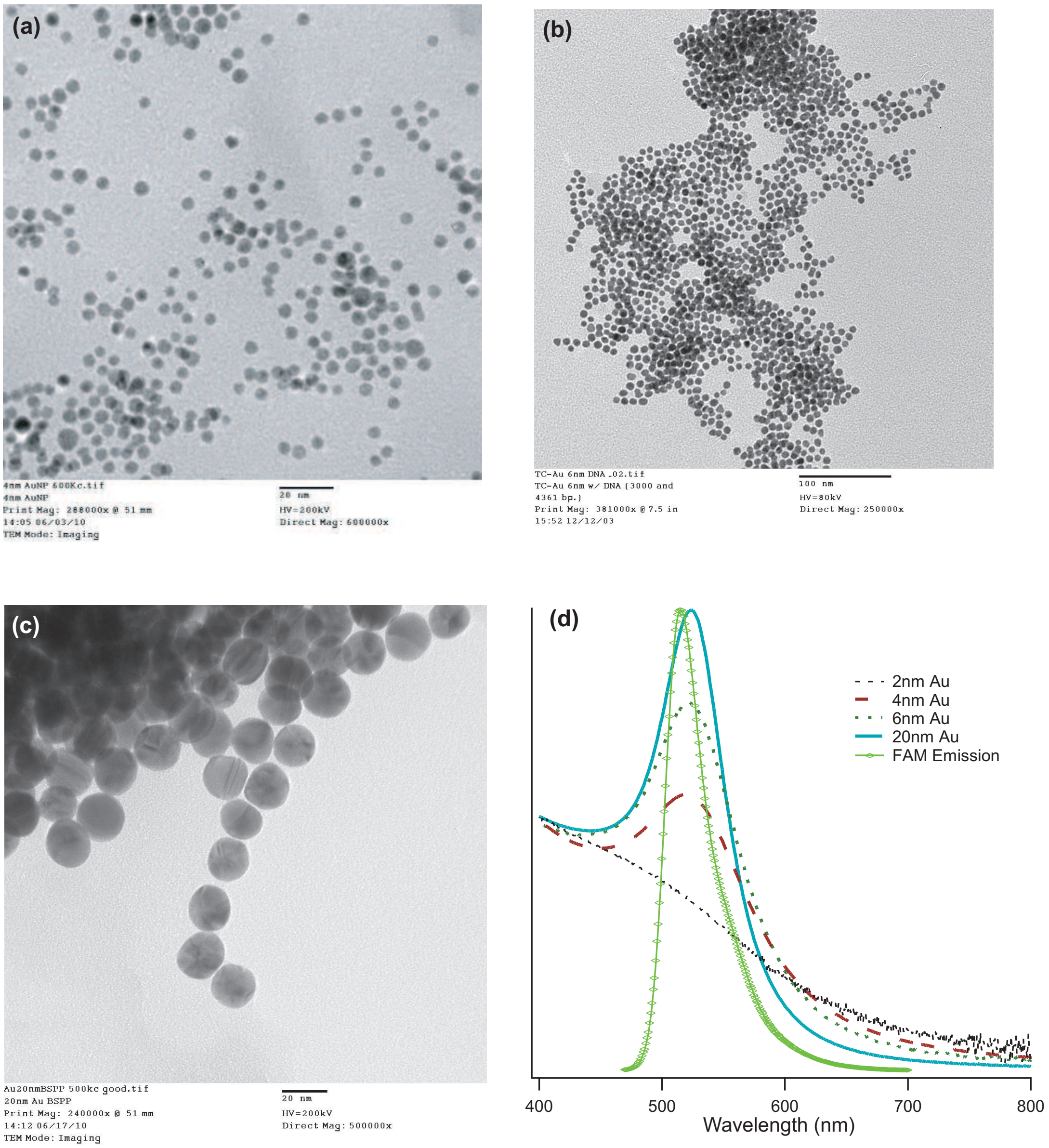

Figure 5.3: TEM image of BSPP capped (a) 4 nm, (b) 6 nm and (c) 20 nm gold NPs; (d) Comparative extinction spectra for the 2nm, 4nm, 6nm and 20nm Au NPs.

Table 5.1: Theoretically calculated extinction coefficient (ε), molar mass (MM_{NP}) and number of atoms ($Atoms_{NP}$) for Au NP of different sizes.

Diameter (nm)	ε ($M^{-1}cm^{-1}$)	MM_{NP} (g/mol)	$Atoms_{NP}$
2	5.5×10^5	4.87×10^4	250
4	5.54×10^6	3.90×10^5	2000
6	1.97×10^7	1.31×10^6	6700
20	9.20×10^8	4.87×10^7	250000

15S - RSS-C_6-GCACGAATTCACACG
30S - RSS-C_6-GCTGATGACTATCGAATTCGGTAGTAGGCG
45S - RSS-C_6-CGAGGTTGGCAAGAGTAACACGGAATTCAGTATGCACACGGAACG
60S - RSS-C_6-GCAGATACTAGAGATTATGTGGATGAATTCGCTAAGAGTGGATAGTAT GTGCACGGAACG
All strands were engineered to minimize secondary structures using mFold.

DNA was assembled onto 4, 6 and 20 nm Au NPs using a 1:1 dsDNA:NP ratio. A standard assembly of double-stranded DNA (dsDNA) with the NP was accomplished by first deprotecting 1 nmol of the single-stranded 5′-SSR DNA in 125 μL buffer with 20 μL of 50 mM Tris(2-carboxyethyl)phosphine hydrochloride (TCEP) in 20 mM PBS buffer pH 7.5 at RT for $\geq$45 minutes. The freshly deprotected DNA-thiol was desalted with a NAP-V column and the dye-containing complementary strand (900 pmol) was immediately added. The strands were annealed at 95°C for 2 minutes, cooled to RT for 2 minutes and then added to 1 nmol purified SPP-capped NP. The mixture was vortexed and placed at 4°C in the dark for conjugation >24 hours. Purification for the 4 nm and 6nm conjugates was accomplished by successive ($\geq$3) salt precipitations by adding 6 M NaCl dropwise to solution to induce aggregation, centrifuging at 13,200 rpm for 2 minutes, decanting the supernatant, and re-suspending in buffer. The 20 nm Au-DNA conjugates were purified by centrifuging the assembly at 13,200 rpm for $\sim$ 20 minutes, decanting the supernantant and redissolving the pellet in the buffer. All the purified dsDNA-NP conjugates were stored in 20 mM PBS pH 7.5 buffer at 4°C in the dark.

5.2.3 Absorption/Photoluminescence:

Absorption measurements were acquired on a Varian Cary 50 UV-vis spectrophotometer and photoluminescence measurements were acquired on a Varian Cary Eclipse Fluorescence spectrophotometer using Z-matched 50 μL quartz cuvettes. A typical quantum yield was calculated by measuring the absorption over the 200-800 nm range for both the sample described above and a control (dsDNA-dye without NP), keeping the peak of the dye absorption $\leq$0.1 A.U. Continuous-wave photoluminescence (cw-PL) was first measured on the control strand, adjusting the sensitivity to maximize the PL signal. *Under identical settings* the PL intensity of the dsDNA-NP sample was then measured. Quenching efficiency by intensity measurements, $E(I)$ were determined *via* the following calculation:

$$E(I) = 1 - \frac{I_{sample}}{I_{control}} \cdot \frac{A_{control}}{A_{sample}} = 1 - \Phi' \tag{5.5}$$

where $E(I)$ is the efficiency of energy transfer, $I_{sample,control}$ is the integrated intensity under the curve for the PL peak, $A_{control}$ is the absorption of the sample at its absorption peak, A_{sample} is the corrected absorption of the dye after subtracting out the contribution absorbed by the NP and $\Phi' = \frac{I_{sample}}{I_{control}} \cdot \frac{A_{control}}{A_{sample}}$ is the quantum yield of the dye in the presence of the bound Au NP.

5.2.4 Lifetime Measurements:

Lifetimes are acquired using the output of a Nd:VO$_4$-pumped (Spectra-Physics Vanguard, 2 W, 532 nm, 76 MHz, 10 ps) R6G dye laser (Coherent 702-1). Cavity dumping of the dye laser to 1.9 MHz drops the pulse train to 1 pulse every ~2 μs. In the case of FAM the laser is frequency doubled for λ_{ex}=290 nm. Samples were excited with <1 μW at a right angle geometry relative to a Chromex 500is 0.5 m imaging monochromator with 50 g/mm grating, 0.5 nm resolution. Output of the monochromator is focused into a Hamamatsu C5680 streak camera operating at 20 ns window for FAM. Lifetimes are measured by binning intensity *vs.* time for a 20 nm spectral range about the λ_{em} maximum for the dye. Lifetime quenching calculated by:

$$E(\tau) = 1 - \frac{\tau'}{\tau_{dye}} \tag{5.6}$$

was determined by comparing the measured decay rate for a NP-dsDNA-dye system (τ') *vs.* the observed decay rate for the identical dsDNA-dye in the absence of NP (τ_{dye}).

5.3 Results and Discussion

Binding of DNA to large gold NPs has been accomplished easily in the literature[116, 117] and various methods of medical[118] or bio-molecular[119] optical techniques have been suggested based upon these structures. The research presented here also takes advantage of DNA-NP architectures in examining the optical properties of organic dyes in the proximity of size-controlled metal surfaces.

5.3.1 Comparison to SERS

A brief discussion at this point is helpful in understanding how the subject of fluorophores proximal to metallic colloids may be approached. The photophysical behavior of organic dyes near metal surfaces has been viewed and modeled not only as a function of distance, but has also been compared to its cousin effect, surface-enhanced Raman scattering (SERS). SERS is a phenomenon first noticed by Fleischmann *et al.* in 1974 [120] for pyridine adsorbed onto roughened metal electrodes in which the Raman signal had been amplified by 10^5-10^6 over predicted calculations. The SERS phenomenon is commonly used for the vibrational characterization of small molecules and has been well-documented when the "rough" metal surface is modified to be a colloidal nanoparticle[121, 122, 123, 124, 125]. Moskovits describes the SERS effect for the electromagnetic mechanism as the resonant coupling of plasmons to electromagnetic plane waves which must follow the dispersion relation[126]:

$$k_{\|}^2 = (\omega/c)^2 Re[\epsilon_0 \epsilon (\epsilon_0 + \epsilon)^{-1}] \tag{5.7}$$

where $\epsilon(\omega)$ is the dielectric function of the metal, ϵ_0 is the dielectric constant of the surrounding medium, and ω is the frequency of the oscillating wave. In the creation of a plasmon by an incident plane wave, both frequency and momentum must be conserved, which is not normally the case for the general range of indices of refraction. However, by making the conductive surface rough, the conditions for the far-field radiation may be relaxed. In this case, Eqn. 5.7 is modified where wavevector matching between the incident wave and the surface plasmon follows $\mathrm{k}_{\|}$ plus integral multiples of $2\pi/\lambda$, where λ is the periodicity of roughness. A rough surface, therefore, allows a portion of the plasmon's energy to be radiated instead of being dissipated as heat. Simply put, an emitting dipole very near to a metal surface can excite any order plasmon and "store" the photon energy as a surface plasmon. The N = 1 (first order) plasmon has the symmetry of a time-varying dipole and can therefore radiate to the far-field. In this sense, SERS is observed due to the non-linear effects induced upon molecules dependent upon local enhancement of the electromagnetic field near rough conducting surfaces. The fluorescence from dyes adsorbed onto metal surfaces is sometimes enhanced by 1-2 orders of magnitude due to the dye's ability to directly excite plasmons without breaking momentum conservation laws at these distances. The ability to enhance photoluminescence quantum yields from dyes near metallic nanosurfaces is another field and the primary research of Lakowicz,[56, 127, 128, 129, 130] but will not be elaborated upon here.

Although the true mechanism behind the SERS phenomenon is still under debate and further experimentation is required to gain a deeper understanding, some very interesting research into molecule-colloid interactions has been acquired. Franzen has studied the absorption properties of dye molecules adsorbed onto gold and silver colloidal NPs near 10 nm diameter in an attempt to explain the relationship between the absorption line-shape and the SERS efficiency[131]. He points out that the additive nature of Beer's Law in absorption spectroscopy assumes optical homogeneity. However, due to the strength with which colloidal metallic NPs interact with light, the absorption spectrum of dye-adsorbed NPs may violate Beer's Law where the dye may be considered to exist, optically speaking, *inside* the NP. In this model, the additive nature of dye-NP absorption breaks down as a function of incident light frequency. The plasmon frequency, which typically represents the frequency above which the metal stops to conduct may be considered the energy at which the NP becomes transparent for dye absorption. Therefore at frequencies higher than $\omega_{Frölich}$, ($\omega_{Frölich} = \omega_p/\sqrt{3}$), the molecule would be free to absorb incident light. At frequencies lower than the plasmon absorption transition, $\omega_{Frölich}$, the absorption strength of an adsorbed molecule, especially in the perpendicular orientation, may be diminished by the much higher response of conduction electrons to the electromagnetic field. This tool developed by Franzen, along with the relationship between absorption line strength and the radiative rate as mentioned in Chapter 2 will give valuable insight into the effect of the metal surface on the photosensitivity and photophysics of the donor dye. Note that the electromagnetic mechanism explaining SERS relies upon the enhanced electric field affecting the dye molecule, whereas NSET relies upon the dye molecule first being excited and then affected by the NP.

A contrast should be made at this point in reference to the work discussed in our earlier publications[16, 17] in which fluorophore properties were investigated in the vicinity of 2 nm NPs. Because these particles are below the size where surface plasmons exist, they would not be expected to participate in a SERS event which relies upon the plasmon band and are therefore ruled out of this discussion. The larger 6 nm and 20 nm particles, however, are large enough that they could contribute to either SERS or NSET, depending upon the conditions.

5.3.2 Photoluminescence and Lifetimes of Dyes Near Au NP

The quantitative optical characterization of a dye molecule luminescence can be expressed in the concept of a quantum yield. A quantum yield, often paraphrased as “photons in divided by photons out,” is a relation between the ability of a molecule to absorb light and its ability to release that stored energy as another photon of light, (always at slightly lower energy). This statement implies that not only the measured photoluminescence intensity for a dye, but also the dye’s ability to absorb light must be measured to accurately determine a quantum yield.

A true quantum yield measure using an integrating sphere will do just this; it will deliver a calibrated amount of electromagnetic energy to an absorbing sample and monitor the amount of energy returned as light. A similar measurement may also be performed, in the absence of an integrating sphere, using a *relative* sample of known quantum yield. The first method of characterizing the efficiency of dye molecules near 6 nm gold spheres is measuring the efficiency of the dye relative to a standard. In these experiments we have a fortunate choice for the standard quantum yield, which is the *identical* sample, only in the absence of a quenching NP.

Because, as was shown earlier[16], neither the oscillator strength of the dye nor the absorption cross-section are altered by the enhanced electric field of the NP, we can be sure that there are no non-linear effects taking place and the relative quantum yield determination is as simple as taking the absorption-PL measurements to compare both sample and control according to Eqn. 5.5.

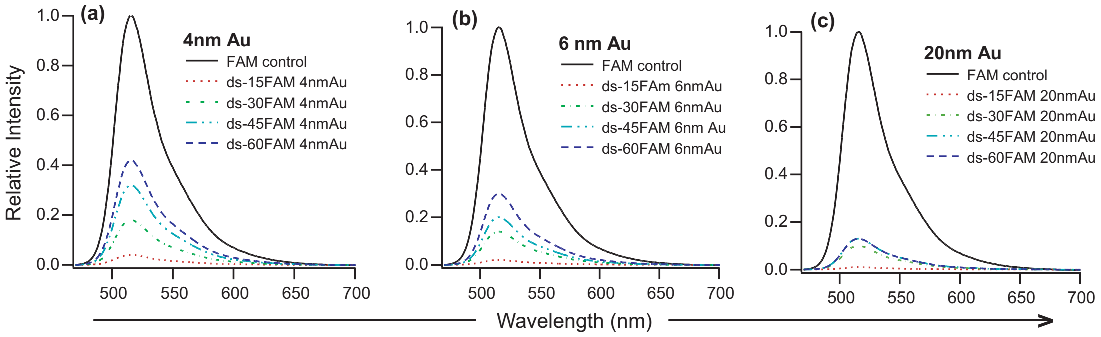

Figure 5.4: Photoluminescence quenching of FAM by (a) 4 nm Au NP, (b) 6nm Au NP and (c) 20nm Au NP.

Figure 5.4 shows the photoluminescence intensities for FAM quenched by 4 nm, 6 nm and 20nm Au NP, where the intensity of the sample has already been adjusted to account for absorption from the NP. This is accomplished by taking the absorption spectra after subtracting the NP absorption and comparing an average of 5 data points at the peak (490 nm - FAM) and multiplying this ratio by the entire PL signal. By exciting at wavelengths higher in energy than the onset of photoluminescence we are able to capture the entire spectrum without contributions from the excitation source.

When inspecting Figure 5.4 the photoluminescence intensity is strongly quenched at short distances and follows an expected trend that longer separation distances quench the fluorophore less. Comparison of the photoluminescence quenching found in these systems to those shown earlier[16, 17] demonstrates a greatly increased efficiency of energy transfer in the case involving a a larger particle. A 4nm particle has a higher quenching efficiency compared to a 2 nm particle. The quenching efficiency increases with the increasing particle size. A 20 nm particle has the highest quenching efficiency. As is already known[17], LSPR plays an important role in the quenching phenomena. LSPR is a result of the free conduction electrons whose density will increase as the size of the particle increases at least up to r=10nm[62].

The lifetimes for FAM are displayed in Figure 5.5. Lifetime of *control* FAM strand is 3.54±0.2 ns. Once again, the trend is clear that as a function of separation distance to the surface of the NP, the decay rate changes in a predictable manner. At short distances a very fast rate of decay is observed, which lengthens considerably at the longest distance measured. The reasons for the quenched lifetime can be easily explained through the equation $k_{obs} = k_r + k_{nr} + k_{et}$. The lifetime data is fit to a bi-exponential function of the form:

$$I(t) = y_0 + I_1 e^{-k_1 t} + I_2 e^{-k_2 t} \tag{5.8}$$

Table 5.2: Experimentally observed distance dependent quenching in normalized PL (Φ') and lifetime τ' (shorter quenched component) for FAM (Φ_{dye}=0.9, τ_{dye}=3.54±0.02 ns) at 4 nm, 6nm, and 20 nm Au NP. Also listed are the contributions from the shorter quenched component (I_2) for each of the NPs at each length.

AuNP size(nm)		15bp 68Å	30bp 120Å	45bp 170Å	60bp 220Å
4	Φ'	0.04±0.02	0.18±0.04	0.32±0.04	0.42±0.03
	τ'	0.23±0.01	0.72±0.02	1.27±0.04	1.33±0.04
	I_2	98%	85%	79%	45%
6	Φ'	0.02±0.02	0.14±0.03	0.20±0.02	0.30±0.04
	τ'	3.54±0.01	0.43±0.03	0.52±0.03	0.86±0.06
	I_2	-	98%	98%	81%
20	Φ'	0.01±0.02	0.10±0.04	0.13±0.03	0.13±0.04
	τ'	3.54±0.03	0.29±0.04	0.48±0.03	0.42±0.06
	I_2	-	99%	97%	97%

where the intensity as a function of time is related to a linear offset, y_0 plus a two exponential terms including the decay rate constants, k_1 and k_2 weighted by pre-exponential factors, I_1 and I_2. The fitting allows the deconvolution of both decay rates and yields values that we may use to interpret a physical meaning. Almost all the strands have a bi-exponential decay with a long component corresponding to free FAM (τ=3.54ns) and the shorter quenched component. The lifetimes for ds-15FAM at 6 nm and 20 nm fit better to a mono-exponential decay corresponding to the free FAM. The dye in this case is heavily quenched (>95%) and hence the signal from the free FAM only was detectable. The photoluminescence and lifetime data is presented in Table 5.2. The lifetime corresponding to free FAM in solution is not reported in Table 5.2 to avoid confusion.

For example, fitting of the FAM-15mer-NP for a 4nm Au sample shown in Figure 5.5 to a bi-exponential function gives two lifetimes, τ_{fast}=230 ps and τ_{slow}= 3.54 ns. Comparison with an unperturbed FAM dye on the $5'$ end of a strand of dsDNA which also has a lifetime of 3.54 ns at pH 7.5, suggests that the slow component of the sample lifetime is the result of some concentration of unperturbed dye molecules in solution. The best explanation for the observation of the 3.54 ns decay rate is that some concentration of *unbound* FAM-dsDNA is found in solution, either as a result of incomplete purification or some equilibrium of dsDNA ligand exchange with the solvent. Further proof for the presence of free DNA-FAM was confirmed by running a 2% agarose gel on ds-30FAM conjugated to 4 nm , 6 nm and 20 nm Au NP. The gel was ethidium bromide stained to visualize the free DNA-FAM. Luckily, further information beyond the rates of decay may also be extracted from a lifetime measurement.

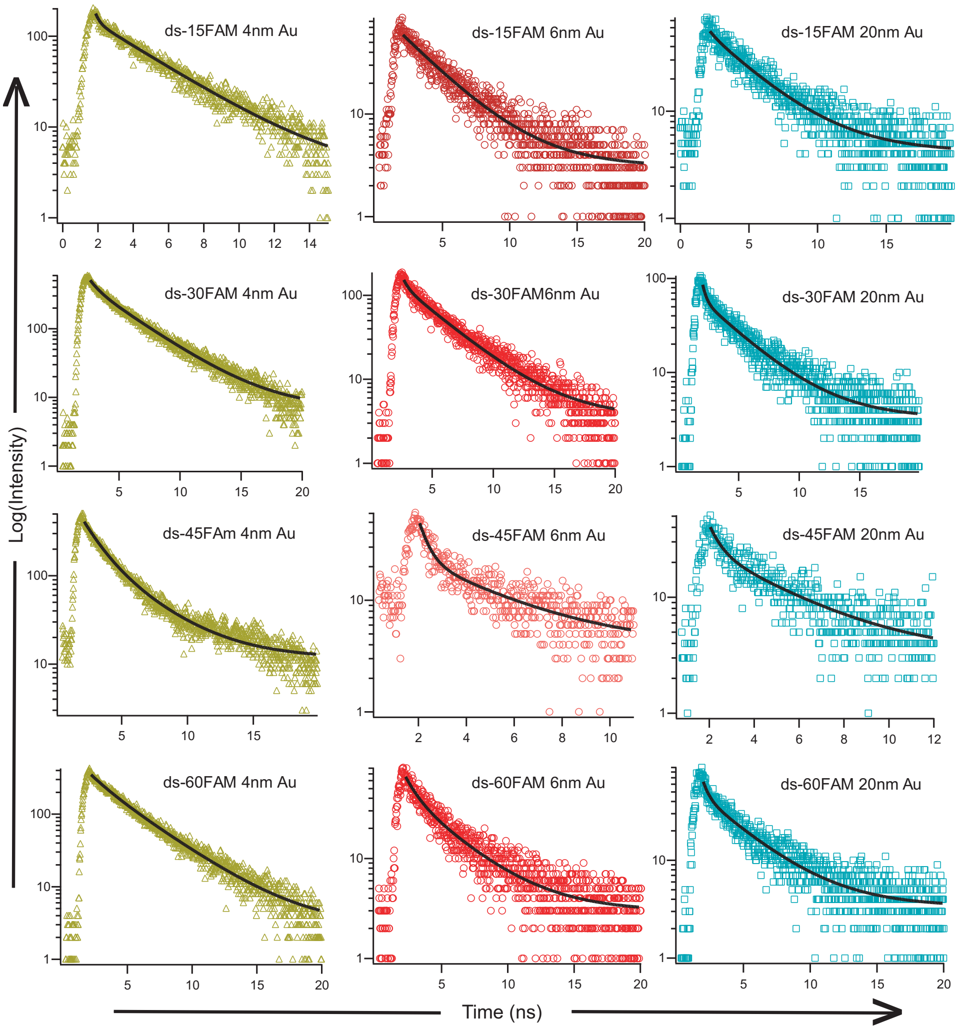

Figure 5.5: Lifetime quenching of FAM by Au NP of diameter 4 nm, 6 nm, and 20 nm separated by 15bp, 30bp, 45bp and 60bp dsDNA.

Equation 5.8 also fits the pre-exponential terms for each decay process which is essentially the relative contribution of each rate to the total signal observed. Therefore, by normalizing and taking the fraction of each pre-exponential term, one can calculate the relative population of bound to unbound dsDNA in solution using the following: $Contribution_1 = I_1/(I_1 + I_2)$. By doing this calculation, we also realize that the contribution to the total intensity under the lifetime is largely (∼90%) related to the bound state (Table 5.1). Only in the case of ds60FAM it can be seen that on a 4nm Au NP only ∼50% of DNA is bound. The ds-15FAM on 6 nm and 20 nm Au shows a single exponential lifetime corresponding to free FAM however the photoluminescence experiment suggests that >95% intensity is quenched. This suggests that only the lifetime of the free FAM is detected by the camera. The reason

Table 5.3: Experimentally calculated quenching efficiencies from photoluminescence quenching, $E(I)$ and lifetime quenching , $E(\tau)$ for FAM at 4 nm, 6nm, and 20 nm Au NP.

AuNP size(nm)		15bp 68Å	30bp 120Å	45bp 170Å	60bp 220Å
4	$E(I)$	0.96±0.02	0.82±0.04	0.68±0.04	0.58±0.03
	$E(\tau)$	0.94±0.01	0.80±0.02	0.64±0.04	0.62±0.04
6	$E(I)$	0.98±0.02	0.86±0.03	0.80±0.02	0.70±0.04
	$E(\tau)$	0.99±0.01	0.88±0.03	0.85±0.03	0.76±0.06
20	$E(I)$	0.99±0.02	0.90±0.04	0.87±0.03	0.87±0.04
	$E(\tau)$	0.99±0.03	0.92±0.04	0.86±0.03	0.88±0.06

that the unbound dye-dsDNA signal exists visibly in the 15mer and is essentially non-existent in the signal for the 45mer is best explained by the relative intensities of these two systems. The intensity of the dye-15mer, being ~90% quenched, means that a good lifetime measurement will require a long period of photon counting for this sample. The intensity of an unquenched population of dye molecules, therefore, will contribute a significant amount to the total signal and become visible. When the photoluminescence efficiency of the bound dye is increased by displacement to further separation distances from the surface, however, the contribution of counts from unbound dye-dsDNA will be "swamped out" by the much higher signal.

Table 5.3 lists the quenching efficiencies based upon photoluminescence and based upon lifetimes for FAM at the three (4, 6 and 20 nm) Au NP sizes for the four (15, 30, 45 and 60bp) DNA separation distances mentioned.

The theories of Persson and Lang[67], Chance, Prock and Silbey[65], and Kuhn[66] all agree that energy transfer from a point dipole to a planar surface will follow a $1/R^4$ dependence, and that energy transfer to a volume will follow a $1/R^3$ distance dependence. The enhanced energy transfer to a larger NP over the 2 nm NP suggests one of two possibilities: either the R_0 value has been extended, or the mechanism of energy transfer has changed. At a NP diameter of only 6 nm, the particle size is still much smaller than the mean-free electron path for gold, suggesting that these materials are still too small to exhibit bulk-like electron-scattering events. This would rule out the R^{-3} dependence under the Persson model in which the transition from R^{-4} to R^{-3} depends upon the introduction of bulk scattering processes. Therefore, we predict that the enhanced efficiency of energy transfer is primarily the product of an increased R_0 value.

Hans Kuhn advanced a theory regarding energy transfer to planes of dipoles, (either a metal surface or a film of dipole acceptors), where energy transfer is treated in a very simple manner[48]. The basis of Kuhn's model assumes the acceptor to be an absorbing body in the field of the emittor dipole where the power absorbed is proportional to the square of the amplitude of the oscillating electric field. Chance, Prock, and Silbey[65] realized the power of such a simple model and extended the theory to account for optical constants of the absorbing media, ie. n_r, k, ϵ_1, and ϵ_2. The final form for calculating the 50% quenching value is:

$$R_0 = \frac{\alpha\lambda}{n_m}(\overline{A}\Phi_{dye})^{1/4}\left[\frac{n_r}{2n_m}\left(1+\frac{\epsilon_1^2}{|\epsilon_2|^2}\right)\right]^{1/4} \tag{5.9}$$

and A is the absorbance of the layer, given by:

$$A = \frac{4\pi k d}{\lambda} \tag{5.10}$$

In Eqn. 5.9, λ is the wavelength of emission for the donor, Φ_{dye} is the quantum yield of the emitter (this meaning is somewhat under dispute), $\alpha = (1/4\pi)(9)^{1/4}$ for a perpendicular dipole and $(1/4\pi)(9/2)^{1/4}$ for a parallel dipole. The term d in the absorption equation is the thickness of the absorbing layer. Conceptually this is very simple and could be useful in calculating energy transfer from a dye molecule when we are concerned about NP size because the absorbing film thickness, which could be construed as NP diameter, is inherent to the model calculations. To adjust these equations and relate them to a metallic nanoparticle, certain terms need to changed.

The distance in Eqn. 5.10 uses d as the thickness of the layer, which can be considered as the thickness of a nanoparticle. Also,we know that geometrically the total quenching rate will be proportional to 1/3 $k_{\perp}$ and 2/3 $k_{\parallel}$, which should be reflected in the final equation. Finally, as demonstrated in Chapters 1 and 2, metals below the mean-free electron path begin to alter their response to light, reflected by the adjusted dielectric constants. The final form for calculating a R_0 value to a NP under Kuhn and the CPS model looks like:

$$R_0 = \frac{1}{3}\left[\frac{1}{4\pi}(9)^{1/4}\frac{\lambda}{n_1}(A_{NP}q)^{1/4}\left[\frac{n_2}{2n_1}\left(1+\frac{\epsilon_{1NP}^2}{|\epsilon_{2NP}|^2}\right)\right]^{1/4}\right]\cdots \tag{5.11}$$

$$\cdots + \frac{2}{3}\left[\frac{1}{4\pi}\left(\frac{9}{2}\right)^{1/4}\frac{\lambda}{n_m}(A_{NP}\Phi)^{1/4}\left[\frac{n_2}{2n_1}\left(1+\frac{\epsilon_{1NP}^2}{|\epsilon_{2NP}|^2}\right)\right]^{1/4}\right] \tag{5.12}$$

where λ is calculated in nm, and the diameter of the NP is also calculated in nm. The final result will therefore be given in nm. For a 6 nm NP quenching the emission of FAM, using the values: λ = 518 nm, Φ = 0.9, n_m = 1.5, n_2 = 0.62, ϵ_1 = -5.12, and ϵ_2 = 6.85 calculates a R_0 of 20.6 nm.

The quenching data listed in Table 5.3 are plotted in Figure 5.6 for FAM and Cy5 as a function of distance *vs.* the theoretical lines calculated using the Persson model and the CPS-Kuhn model. The most marked contrast between the results shown here *vs.* the results of Chapters 2 and 3 is the greatly increased efficiency of quenching by the larger 6 nm particle. In the case of both dyes, the experimentally measured 50% quenching value is somewhere near the 45 bp distance (~17 nm).

Attempts to model the cone-angle dependence, as diagrammed in Figure 5.2 as a function of distance, using a modified quenching efficiency of the form:

$$Q_{Eff}(d) = \frac{2 \cdot \arctan\left(\frac{r}{d}\right)}{\lim_{r\to\infty} 2 \cdot \arctan\left(\frac{r}{d}\right)} \left(\frac{1}{1 + \left(\frac{d}{d_0}\right)^4} \right) \tag{5.13}$$

where r is the particle radius would account for the cone-angle sweep, but predicts a quenching efficiency that goes to 50% near 6 nm separation distance. This means that geometry corrections as applied to the CPS-Kuhn model cannot account for the slightly lower observed efficiency when considering distances and cone angles. The last geometry argument to invoke may originate in the flexibility of the C_6-linkers used to attach the DNA to the NP.

For a nanoparticle of diameter 2 nm, the flexibility of the organic linkers connecting the DNA to the NP were considered insignificant. This is a good assumption because a shift in the C_6-chain would result in very slight changes in distance to the organic dye. However, as Figure 5.7 illustrates, when the NP has grown to 6 nm in size, a shift in the conformation of the C_6-chain could bring one surface of the much larger NP closer in distance to the emitting molecule. In fact, even though the ligand, SPP, is negatively charged and should repel the negative phosphate backbone of the DNA, the surface of the gold particle is likely to be positively charged due to the oxidation

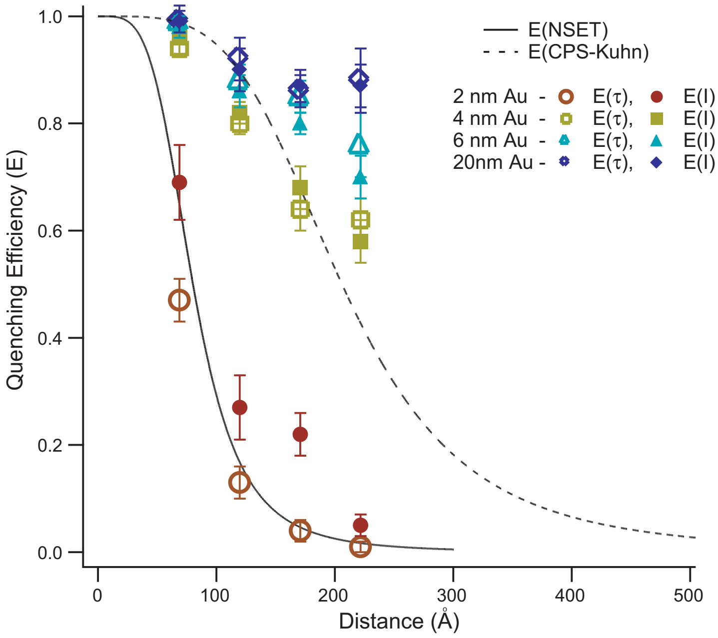

Figure 5.6: Comparison of the experimental data $E(\tau)$ and $E(I)$ with the theoretical NSET and CPS-Kuhn plots.

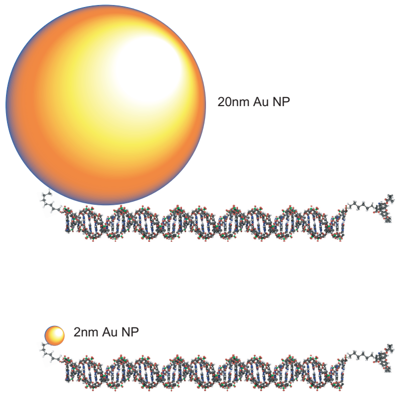

Figure 5.7: Illustration of a 20 nm NP associating with the negatively charged DNA backbone (*Top*) and a 2 nm NP associating with the backbone. Because of the NP size, the distance from the dye to the surface of a 20 nm NP would be vastly different than in the case of the 2 nm NP (*Bottom*) if the particle associates with the backbone.

state of gold(I). This is a driving force for the association of DNA to the gold surface, or at least a pre-disposition to move in that direction, which would indeed bring the dye into closer proximity of the NP surface. The effect is more pronounced for the case of ds-60FAM whihc will also have a higher degree of flexibility as compared to shorter DNA duplex. A much higher degree of quenching for ds-60FAM at all Au sizes is indicative of the flexibility of the C_6 linker as well as the DNA duplex. Such a model could help to explain the increased dye-quenching observed at a predicted distance by changing the actual separation distance by an estimated ~3-6 nm.

5.4 Conclusion

We have shown that the binding of dsDNA-dye ligands to large gold NPs is an efficient reaction with a binding yield of nearly 100% regardless of dsDNA length or dye type. Photoluminescence and lifetime measurements are both supportive and in excellent agreement with each other for a dye with a quenched electronic excited state. The rates of energy transfer are much greater when using a 6 nm NP than when using a 2 nm NP, suggesting an enhanced energy transfer mechanism. The modeling proposed by Kuhn, which takes into account the uptake of energy by an absorbing body within the field of the emitter, gives more realistic values for d_0 but over-estimates the degree of quenching. Massaging the E equation to consider distance-dependent geometry also does not predict the correct quenching behavior. The best fit of experimentally calculated quenching efficiencies to a theoretical model is supplied by considering the flexibility of the C_6-linkers and the induced change upon separation distance for such a large NP. The larger the NP, the less predictable is the distance to the surface when using DNA as a spacer. For confidence in spacer distance from the larger NP sizes, the best technique to measure the optical properties of dyes may be an inert, non-conducting shell of variable thickness to which dye molecules may electrostatically adsorb or be chemically bound through short organic spacers.

CHAPTER 6

TRACKING SPATIAL DISORDER IN AN OPTICAL RULER BY TIME-RESOLVED NSET

6.1 Introduction

RET techniques are an essential tool in biological and bio-physical laboratories, allowing a convenient method to analyze structural conformations of macromolecules or biomolecular interactions in real-time[1, 8, 9, 79, 132, 133, 134, 135, 136]. Unfortunately, as a method that relies upon optically-active probe molecules, the assumption that each probe is a non-interacting bystander is not always correct[137, 138, 139, 140, 141, 142, 143, 144] . If a probe molecule does in fact interact with the system under study, then the optical readout and interpretation of the results will not reflect reality on the molecular scale. With the advent of newer and brighter fluorophores (dyes and quantum dots) for applications in optical rulers and imaging, their interactions with the biomolecules need to be understood prior to application. Especially when using quantum dots which can have a wide variety of surface ligands and can allow for a variety of interactions with their environment and biological molecules[137, 138, 139, 140]. Therefore, techniques capable of detecting and quantifying the degree of molecular-level interactions must be developed to make optical ruler systems truly quantitative.

In this chapter, Nanometal Surface Energy Transfer[15, 16] (NSET) optical ruler is applied to analyze the ratio of the intercalated to the solvent exposed conformation for the common cyanine dye Cy5 and FAM. The cyanine class of dyes are positively charged and have been observed to intercalate along DNA[141, 142, 143, 144], not allowing a randomized κ approximation and thus can lead to errors in the measured D-A separation distance. The intercalation can be influenced by linker length and attachment site (terminal or internal) for the dye on DNA. In this family, Cy5 is a common near IR dye used as an optical probe. Since the Au nanoparticle in NSET acts as a dark quencher and is capable of measuring longer contact distances, it can provide a convenient probe for positional (static or dynamic) conformation of the donor (dye) arising from molecular level interactions within the biological construct. The analysis of dye intercalation is compared between Cy5 and FAM, since FAM is reported to exist exclusively as a solvent exposed donor[145], unlike Cy5. DNA-Cy5 conjugates appended to Au nanometal provide a perfect system to investigate the impact that molecular-level interactions will have upon the results of an optical ruler and the usefulness of a NSET probe to analyze the degree of intercalation for this dye family.

The experimental results support the assumption that the donor dye interaction is directly dependent on the nature and site of appendage of the dye along the DNA duplex but only minimally impacted by spacer length. Through the use of MEM-NLLS (maximum entropy method non-linear least squares)[146, 147, 148, 149, 150] analysis, the equilibrium percentage of occupation and a lower limit of the dynamics of site exchange of the intercalated *vs.* solvent exposed dyes is assessed. The significance of molecular level interactions by fluorescent probes as related to optical ruler technology is demonstrated and emphasize the importance of sensitive techniques like time-resolved photoluminescence is emphasized in optical methods if they are to be widely applied as an optical ruler in the biological tool box.

To accurately use molecular dyes for optical rulers, the equilibration between intercalated and solvent exposed donors must be definitively established. Intercalation of a dye along DNA has two important implications for energy transfer based techniques: (i)the κ value in FRET can no longer be assumed to be 2/3, and, (ii)if the binding affinity for intercalation is not 100%, the measured distance will represent an average of the actual distances convoluted by κ influences, which in FRET goes as κ^2. For Cy5, the degree of error in the FRET based measurement will depend directly on the equilibrium of intercalated versus solvent exposed conformations and the kinetics of exchange between the two conformational sites. While the effects of intercalation have been examined by theoretical modeling[151], NMR[141], and ensemble and single molecule optical experiments[133, 151, 152], the complication of changes in κ coupled to the distribution of intercalated versus solvent exposed Cy5 donors make analysis of FRET distances complex if the percentage of the sites and the dynamics of the site exchange is not discernible.

6.2 Experimental

6.2.1 Optical Measurements

The ratio of intercalated to solvent exposed donor populations was analyzed using NSET to assess the separation distance between the molecular donor (FAM, Cy5) and a 2 nm Au NP (nanoparticle) appended through a terminal $5'$ C_6 spacer. The experimental distance of separation (R) between the donor and nanometal can be extracted from fits of the excited state lifetime decay for the experimental DNA sequences. The distance is extracted from the theoretical NSET curves by calculating the efficiency of quenching, $E(\tau)$,

$$E(\tau) = 1 - \frac{\tau'}{\tau_{dye}} \tag{6.1}$$

where, $E(\tau)$ is the efficiency of energy transfer using lifetime analysis, τ_{dye} is the lifetime of the donor dye with no Au bound to the ds-DNA while τ' is the lifetime of the dye when the Au is bound to the ds-DNA assembly. The experimentally measured distance of separation (R) between the donor and the metal nanoparticle can be solved for by expressing E in terms of R and R_0,

$$E = 1/[1 + (R/R_0)^4] \tag{6.2}$$

where, R_0 is the distance at which 50% energy transfer is observed and is given by the empirical NSET expression,

$$R_0 = \left(0.225 \cdot \frac{\Phi_{dye}}{\omega_{dye}^2} \cdot \frac{1}{\omega_F k_F} \cdot c^3\right)^{1/4} \tag{6.3}$$

As can be seen the contributions to the value of R_0 are from the metal acceptor ($k_F = 1.2 \times 10^8 cm^{-1}$, $\omega_F = 8.4 \times 10^{15} rad/s$) and the donor ($\omega_{dye}$ (Cy5=$2.91 \times 10^{15} s^{-1}$, FAM=$3.8 \times 10^{15} s^{-1}$), ϕ_{dye} (Cy5 = 0.25, FAM = 0.9), where ω_{dye} and Φ_{dye} represent the angular frequency of donor emission, and the quantum yield of the donor respectively and c ($3.0 \times 10^8 m/s$) is the speed of light. This yields value of R_0^{Cy5} = 65.0 Å and R_0^{FAM} = 85.0 Å. It can be seen that no κ term appears in this expression.

The steady state and time-resolved optical measurements were conducted at 293 K±2 K in 50 μL cuvettes using 200 pM DNA samples in 20 mM PBS buffer, 0.1 M NaCl, pH7.5. For the optical energy transfer measurements the dye-only conjugated ds-DNA lacking the appended Au is referred to as the *control* strand, while the *sample* strand signifies the dye and Au conjugated ds-DNA assembly. Absorption data was collected on a Varian Cary 50 UV-Vis spectrophotometer and the steady-state photoluminescence was measured on a Varian Cary Eclipse Fluorescence spectrophotometer (λ_{ex} = 580 nm(Cy5) and λ_{ex} = 410 nm(FAM)).

The photoluminescence lifetimes were measured by exciting the samples with the output of a Nd:VO$_4$ (Spectra-Physics Vanguard, 2 W, 532 nm, 76 MHz, 10 ps) pumped R6G dye laser (Coherent 702-1). The output of the dye laser (600 nm, Rhodamine 6G) was cavity dumped at 1.9 MHz. Samples were excited with <1 mW power and the emission was collected at right angles onto a Chromex 500is 0.5 m imaging monochromator with a 50 g/mm grating and 0.5 nm resolution. Output of the monochromator is focused into a Hamamatsu C5680 streak camera operating at a 10 ns window for Cy5 and at a 20 ns window for FAM. The steady state intensity data is generated by integrating the spectral profile in time from the streak camera.

Lifetime analysis was carried out over 6-7 lifetimes of the dye for the internal dyes, and 3-4 lifetimes for the terminal dyes. The lifetime data was fit using the maximum entropy method (MEM) coupled to non-linear least squares (NLLS), developed by

P.J.Steinbach (MemExp v2.0) where the non-linear least squares fitting was performed *via* coupling of MemExp v2.0 to code in *Mathematica 4.2*[146]. Statistical analysis of the of the raw lifetime data indicates a bi-exponential fit is correct for the Cy5 when internally labeled and is not required to fit the terminal Cy5. For MEM-NLLS, high signal to noise is critical to eliminate artifacts in the MEM-NLLS linewidths since low S/N leads to artificial broadening of MEM-NLLS data. In these studies the S/N was 100:1. The MEM-NLLS analysis was constrained by eliminating contributions from negative exponentials, lifetimes greater than two times the natural lifetime of the dye and processes that occur at times comparable to the excitation pulse (10 ps) or longer than the experimental time window (200 ns). The experimental fits do not show the pulse and noise contributions for clarity. Signal to Noise was improved for the data by binning the photoluminescence intensity collected on the streak camera over a 20nm spectral window at the centroid value of the λ_{em}(dye).

6.2.2 Terminal Dye Appended DNA

Au nanoparticle conjugation and preparation of the Au-DNA-dye construct was carried out as described previously[16, 17]. The terminal sequences (5′-3′) utilized in the study are , (Dye = FAM or Cy5).
15mer - (Dye-C_6-)CGTGTGAATTCGTGC
30mer - (Dye-C_6-)CGCCTACTACCGAATTCGATAGTCATCAGC
45mer - (Dye-C_6-)CGTTCCGTGTGCATACTGAATTCCGTGTTACTCTTGCCAACCTCG
The complementary strands (5′-3′), where Au NP is appended at the 5′ end by reducing the dithiol, are
15S - (RSS-C_6-)GCACGAATTCACACG
30S - (RSS-C_6-)GCTGATGACTATCGAATTCGGTAGTAGGCG
45S - (RSS-C_6-)CGAGGTTGGCAAGAGTAACACGGAATTCAGTATGCACACGGAACG
The complimentary ss-DNA sequences (15, 30 and 45 bases long) were purchased from IDT and are identical to the sequences used in a previous publication[16, 17]. The ss-DNA was modified with either a 5′ dye (Cy5 or FAM) attached through a C_6 linker, or a 5′ disulfide protected thiol modification for coupling to a Au.

6.2.3 Internal Dye Appended base modified DNA

For the internal base pair modification studies, a 60 mer ds-DNA sequence (Figure 6.1) was used for all studies. The ss-DNA strands consisted of a 5′ terminal C_6 thiol (DNA-O-P-O-(C_6-S-SR), and for the compliment ss-DNA, a sequence with an internally dye modified T-base FAM or Cy5 was used (Figure 6.1). This allows local distance to be probed while minimizing DNA conformational changes. For Cy5 (Cyanine 5) labeling was at site T19, T27, T34, T38, and T44 from the 5′ end. For FAM (fluorescien) the labeling was at site T14, T27, T38, T44, T54 and T58. In order to distinguish the sequence used in the optical experiments, the experimental ds-DNA is named with respect to the dye labeling position on the ss-DNA, for instance the 60mer labeled at T38 with Cy5 is termed the 60int38Cy5, while the one with FAM is 60int38FAM. In order to probe the effect of the linker length on the ratio of intercalation for the Cy5 donor, the 60int44Cy5 strand was prepared with both a C_6 and a C_3 linker appended off the T-base. This sequence is identified as C_6-60int44Cy5 or C_3-60int44Cy5, respectively.

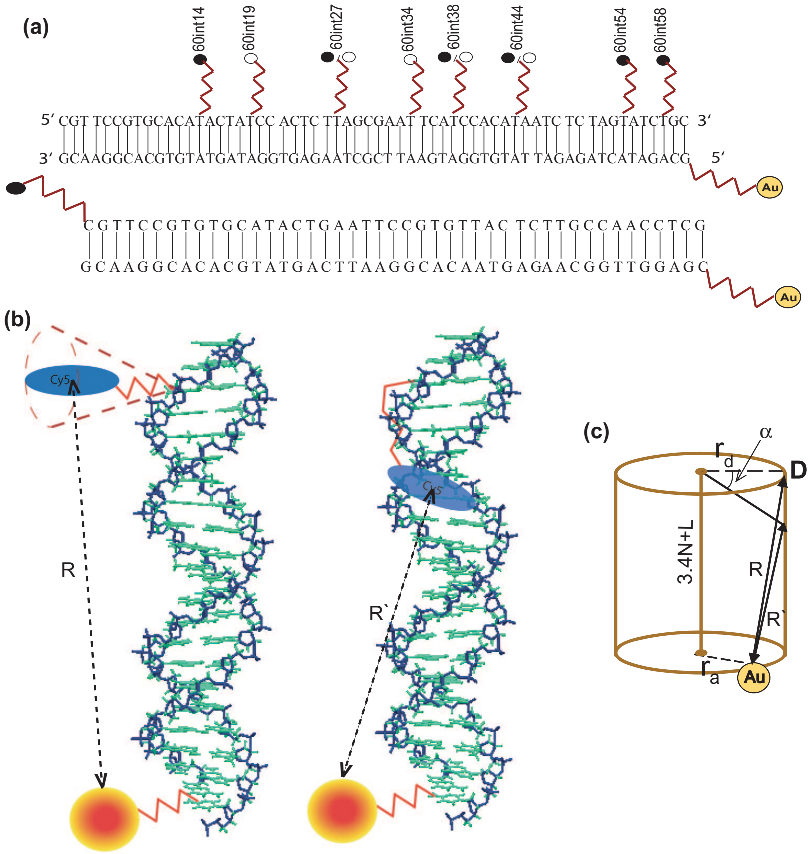

Figure 6.1: **(a)** Scheme showing the sequence of the 60mer ds-DNA and the positions at which Cy5 (○) or FAM (●) is incorporated into the system and also the 45mer ds-DNA with the dye(Cy5) attached to the terminal end. **(b)**The dye when bound to the DNA depending on its nature can be free to rotate or intercalate along the backbone, **(c)**The double strand DNA can also be visualized as a cylinder with the Au NP at one end. The donor is shown as a solvent exposed dye, although the possibility of intercalation exists for Cy5, which will occur in the direction of the nanometal. The quencher (Au) being negatively charged is believed to be repelled by the phosphate backbone and hence is not believed to interact with the ds-DNA.

6.2.4 Measuring average contact distances

Duplex DNA lengths less than 100bp (base pairs) are typically assumed to be adequately modeled by a rigid rod approximation with only high frequency oscillations along the backbone[77]. This allows the separation distance between the appended Au NP at the $5'$ end and the molecular donor appended along the backbone to be readily evaluated using the model introduced by Clegg *et al.*[79] to account for geometric distance corrections arising from the orientation of the donor and acceptor along the nucleic acid backbone. If we assume the Au NP is positioned at the full extent of the C_6 terminal linker at the $5'$ end of the DNA (Figure 6.1) and that the distance of D-A separation is defined from the surface of the Au NP (at the site of attachment) to the center of the donor (Dye), then using the Clegg model the separation distance (R) between the dye (donor) and the 2 nm Au (acceptor) is defined as ,

$$R = \left[(3.4\Delta N + L)^2 + \xi\right]^{1/2} \tag{6.4}$$

where, ΔN is the number of base pairs separating the D-A pair, L is the increased separation distance for a fixed spacer length (C_6, $L = 1.3$ nm) arising between the donor (dye) and acceptor (2 nm Au) due to the DNA helicity for a projection of the donor onto the same plane as the acceptor at zero base pairs, and $\xi = {r_a}^2 + {r_d}^2 - 2r_ar_d[cos(\theta + 36\Delta N)]$ corrects for the projection of the D-A as the length of separation varies. The values r_d and r_a represent the distances of separation of the donor and acceptor from the DNA helical axes arising due to the C_n ($n = 6$ or 3) spacer. The values of r_d and r_a are assumed to be 0 Å for Au and dye when an interaction exists between the DNA and the moiety resulting in a folding back of the linkers, while a value for r_d and r_a of 15 Å for C_6 (or 7.5 Å for C_3 spacer) is used implying a fully elongated linker for both dye and Au. θ is the angle between the D-A at the zero-base projection of the donor onto the plane of the acceptor. Intercalation of the donor dye is accounted for by assuming the interaction occurs in the minor groove along the axis of the DNA. For the intercalated donor a distance R' is defined where $R' = R \pm cos\alpha$. α is the angle subtended by the C_n linker due to the intercalation of the dye.

6.2.5 Conformational Analysis by Maximum Entropy Method - Non Linear Least Squares (MEM-NLLS)

The maximum entropy method (MEM) coupled to a non-linear least squares analysis (NLLS) is a powerful algorithm capable of separating individual decay states from a random population. The MEM-NLLS method allows the lifetime distributions to be accurately analyzed in the absence of a model providing a statistically meaningful approach to assigning the difference between a single exponential, a bi-exponential, or a stretched exponential decay function[146].

The method is particularly useful for energy transfer analysis, where the donor or acceptor may occupy multiple sites along the backbone of a biological molecule. For this case the difference between a single-exponential, a bi-exponential, and a stretched exponential will reflect the dynamic equilibrium of the dye positions. Rapid exchange between two sites will yield a single exponential if the exchange is fast (for a 1 ns lifetime, exchange faster than 1 ps). If the exchange is slow for a 1 ns lifetime (>100 ns exchange rate) then a bi-exponential lifetime is observed. Intermediate exchange rates will give rise to a stretched exponential function. In MEM-NLLS, the single exponential and stretched exponential are observed as a single Gaussian function plotted as intensity (event occurrence) *vs.* $\log(\tau)$. The bi-exponential will give rise to either two distinct Gaussians, or if the lifetimes are close in value an overlapping set of Gaussians is observed (Gaussian with a shoulder). The big difference between the stretched and single exponential is the width of the Gaussian function, a stretched exponential is broad, while a single exponential is sharp. While it would seem that one could extract the distribution function from the width, unfortunately the width is convoluted with the noise.

MEM-NLLS has been utilized to analyze distributions in biophysics in a wide range of experimental probes by allowing the characterization of lifetime distributions as a set of ρ-values (average lifetime), and the associated width of the lifetime distribution, $\Gamma(\rho)$ (95.4% confidence limit).The value of ρ and $\Gamma(\rho)$ can be extracted from the experimental data set by applying the maximum entropy method (MEM) to the time dependent intensity decay data. In MEM-NLLS , the logarithmic distribution of lifetimes, $f(\log\tau)$, can be determined by fitting the decay trace, to the convolution function

$$D(t) = \int_{-\infty}^{\infty} f(log\tau)e^{-t/\tau}d\ log\tau \tag{6.5}$$

Since MEM-NLLS is sensitive to the S/N ratio, the data is binned over the full spectral emission manifold collected in the streak camera, which collects spectrally and temporally resolved intensity data simultaneously.

6.3 Results and Discussion

Dye intercalation into the DNA groove impacts the usefulness of optical rulers and has garnered significant interest in the past few years, particularly when the dye is linked to an internal base. The internal modification positions the dye to intercalate into the DNA helix[151]. Likewise, terminal modification at the 5′ end of the DNA *via* an alkane spacer attached to the terminal phosphate group has also been postulated to allow molecular level interactions[145]. Optical rulers rely on the ability to accurately relate the loss of photoluminescence energy from an excited state molecular donor (D) to the acceptance of that energy by an appended molecular acceptor (A).

While several energy transfer techniques that are ideal for optical ruler techniques exist Nanometal Surface Energy Transfer (NSET)[15, 16] allows long distance optical ruler measurements by probing the energy transfer between a fluorescent donor (D)

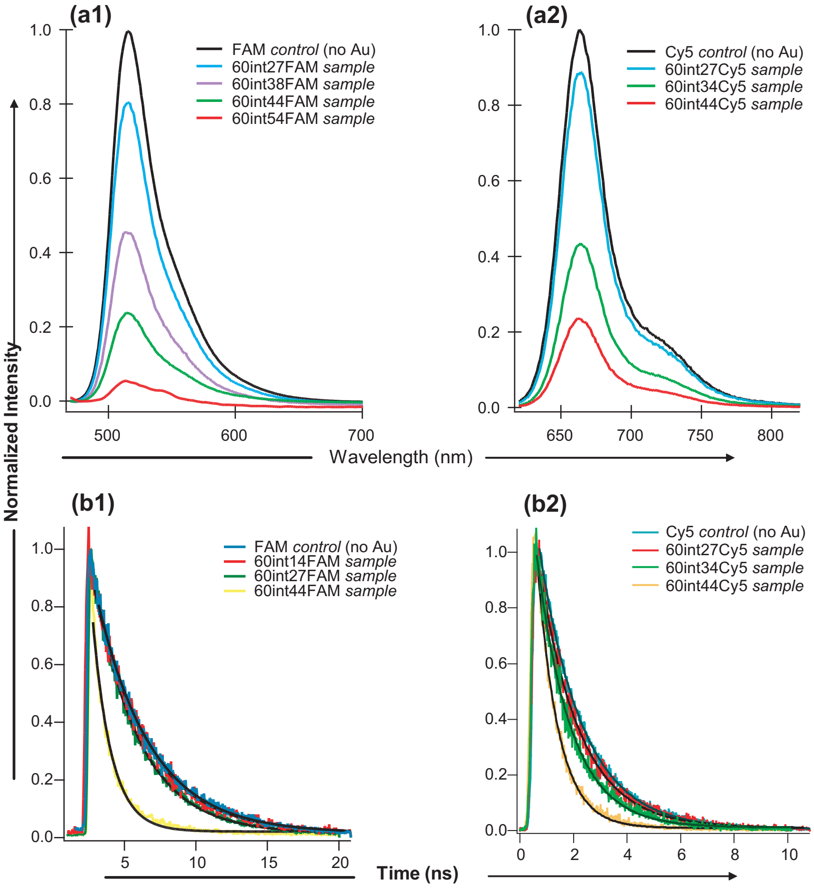

Figure 6.2: Comparative normalized PL intensity for **(a1)**FAM and **(a2)**Cy5 as a function of distance from the Au 2 p;nm quencher. The data is normalized by correcting for the difference in absorption for DNA and donor for the control (no Au) and the various DNA donor positions. **(b1)**Lifetime decay for FAM (λ_{ex} = 410nm, λ_{em} = 520nm) and **(b2)**Cy5(λ_{ex} = 580nm, λ_{em} = 680nm) as a function of different donor-Au separation distances. The exponential fits are calculated as the distributed bi-exponentials from the MEM-NLS treatment for Cy5 and a single exponential fits for FAM.

and a non-emissive metal nanoparticle acceptor (A). The most significant difference between FRET[1, 5] and NSET is that FRET follows a $1/R^6$ distance dependence so that the distance resolution is high but limited to <10 nm, while NSET empirically exhibits a $1/R^4$ distance dependence with lower resolution but a measurement range up to ≈18 nm. While the exact theoretical rationale for the $1/R^4$ distance dependence is still under debate, the empirical observation of a $1/R^4$ dependence has been shown by several groups[20, 28, 153, 154, 155, 156]. In addition NSET has no contribution arising from κ (orientation factor) or $J(\lambda)$ (overlap integral) due to the band structure for a >1.4 nm Au nanoparticle, meaning that the same gold nanoparticle can act

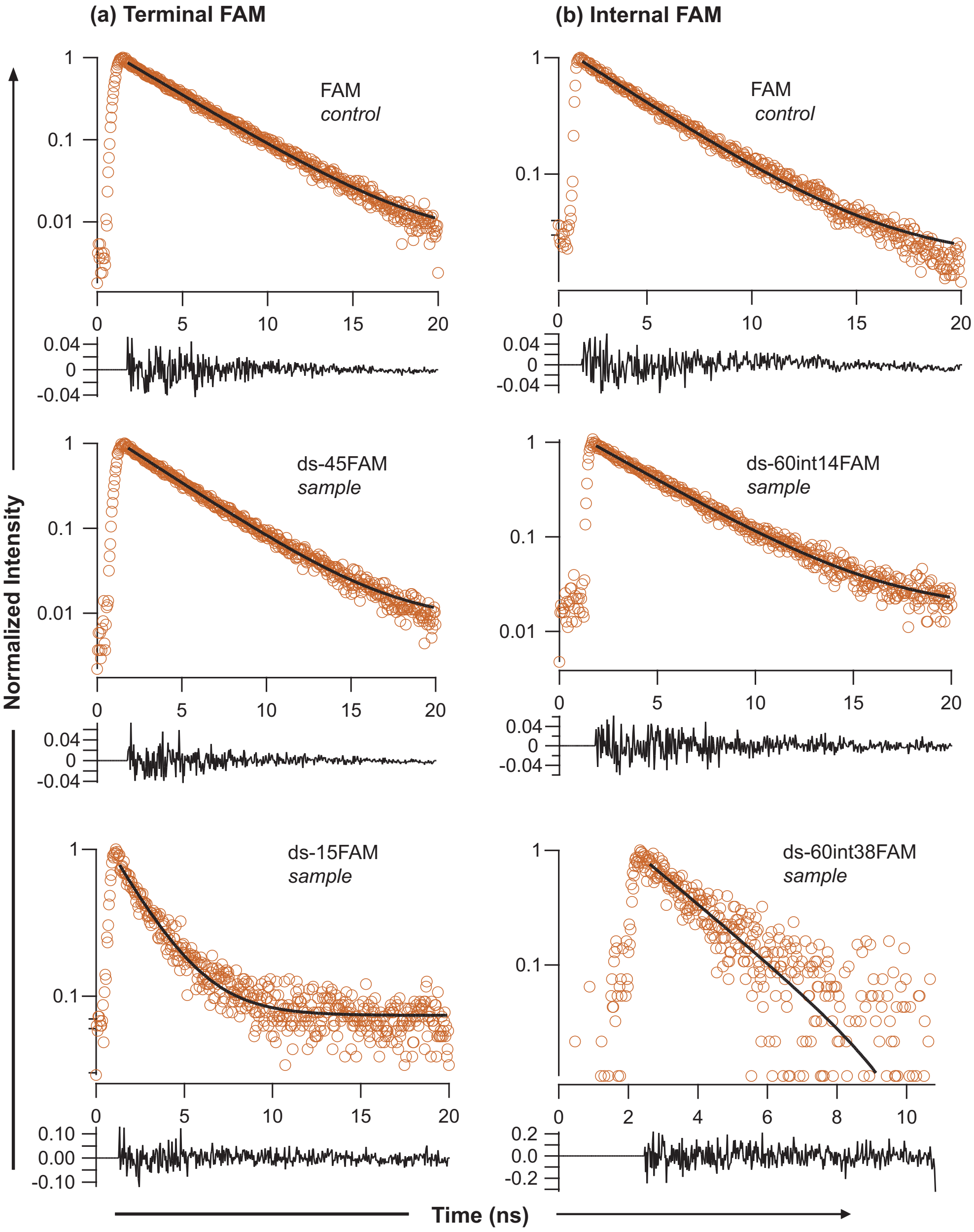

Figure 6.3: A comparison of the mono-exponential fits for various FAM strands when the dye is placed (a)terminal and (b)internal for both *control* and *sample* strands. The residuals are shown for each fit.

as an acceptor for various energetic donor states. By removing the dependence on acceptor orientation and overlap integral dependence of FRET, NSET is best suited for analyzing the importance of donor interactions along biomolecules resulting in errors for positional and orientational factors. This is particularly important as new dyes are developed and implemented for energy transfer studies.

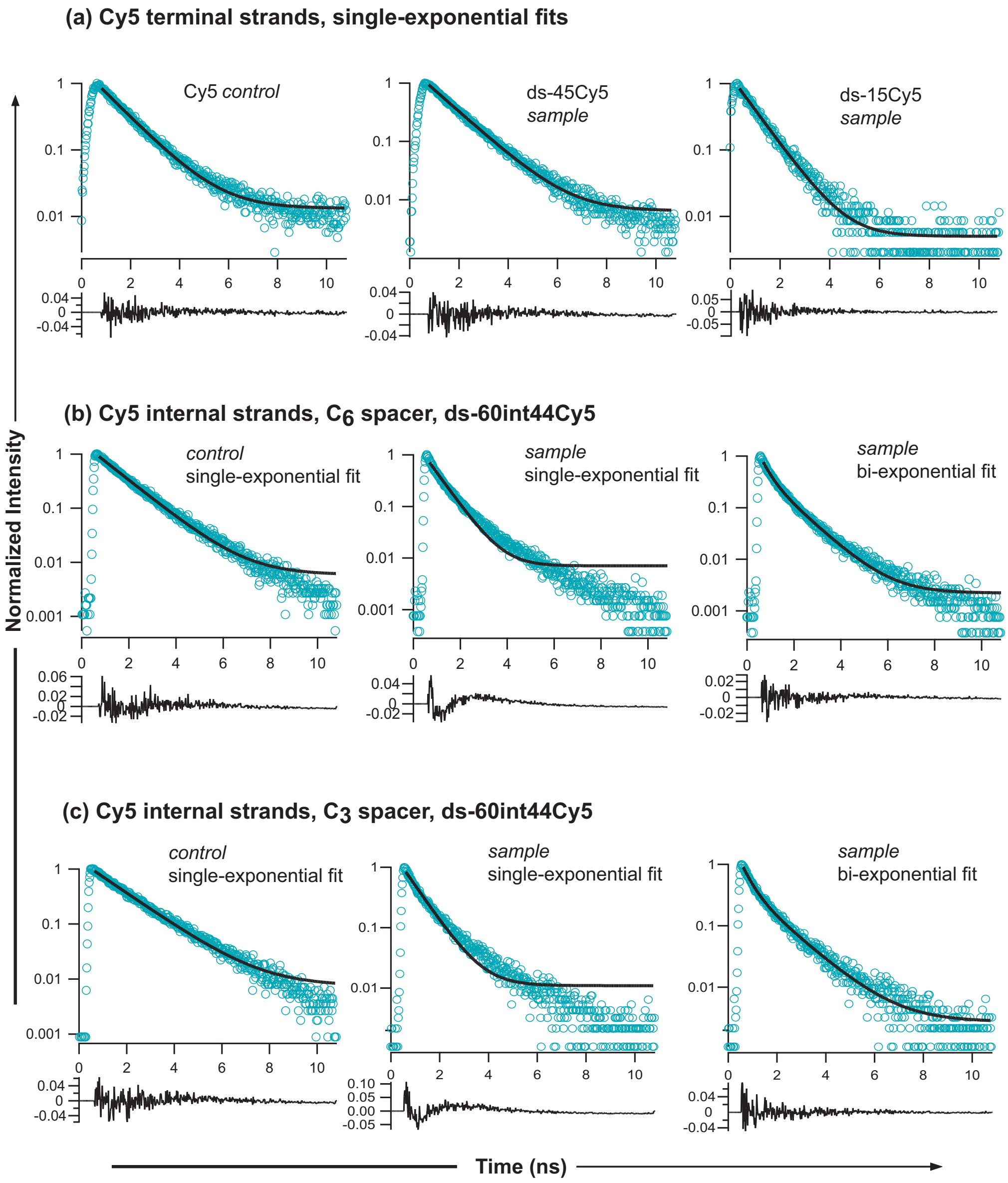

(a) Cy5 terminal strands, single-exponential fits

(b) Cy5 internal strands, C_6 spacer, ds-60int44Cy5

(c) Cy5 internal strands, C_3 spacer, ds-60int44Cy5

Figure 6.4: A comparison of the mono-exponential and bi-exponential fits for various Cy5 strands. The residuals are shown for each fit and the deviation of data from mono-exponentiality is clearly seen for **(b)** and **(c)** when the dye Cy5 is internally labeled on the ds-DNA.

The impact on the donor (Cy5 or FAM) steady state photoluminescence intensity and the time-resolved spectral properties as a function of the position along the

DNA backbone is plotted in Figure 6.2. The lifetime data for FAM and Cy5 *sample* strands is shown in Figure 6.3 and Figure 6.4, respectively with a single-exponential and bi-exponential fit shown. The residuals are also shown with the data. It is clear from the residuals that the internal Cy5 is more appropriately fit to a bi-exponential function, while the terminal Cy5 is adequately fit to a single exponential (Figure 6.4). Likewise, based on residual the FAM data is single exponential for all *control* and *sample* strands (Figure 6.3). Comparison of the lifetimes obtained from MEM-NLLS and non-linear least squares fitting to an exponential function reveal the MEM-NLLS analysis is correct.

6.3.1 Lifetime Analysis by MEM-NLS

MEM-NLLS analysis allows a model to be developed that fits the observed time decays for the NSET results. Fits by MEM-NLLS for the set of FAM and Cy5 sequences are shown in Figure 6.5 and compiled with the calculated and theoretical distances in Table 5.2. Contributions from the pulse are removed but not shown in the fit data in Figure Figure 6.5 or in the compiled data in Table 5.2. If there are no interactions between Au and the dye or Au and the DNA, the Cy5 data is expected to exhibit bi-exponential decay behavior for Cy5 and a single exponential for FAM. For Cy5 data, the *control* strand yields a single Gaussian function. For all the Cy5 *sample* strands a two-component fit is observed when the dye is internal, while for the terminal strands a single exponential fits the data. As the distance between the dye and the Au NP approaches closer to the 50% energy transfer mark (R_0) the bi-exponentiality of the internal Cy5 label becomes more pronounced due to the highest sensitivity of the efficiency curve slope (greatest change in lifetime with distance) around the R_0 region. It is worth noting in the Cy5 internal *sample* strands the area under the curve is analogous to the population statistics between the two lifetime components. This is easily correlated to the population statistics for two positions of the Cy5 along the DNA helix. In the FAM data, the *control* and *sample* strands exhibit single Gaussian functions for both internal and terminal labels. Close inspection of Figure 6.5 shows that the line width of the Gaussian function is broadened between the control strands and the sample strands in both dye experiments. The broadening reflects the conformational disorder about the dye position, but since it is impacted by noise and potentially the Au NP position, the dynamic disorder is not analyzed herein.

The lifetime data is fit using MEM-NLLS analysis coupled to statistical treatment of the data, yielding a single exponential for FAM and a bi-exponential lifetime for internally labeled Cy5 DNA sequences. For terminal appended dyes (FAM and Cy5) only single exponential lifetimes are observed implying a single site occupation on the DNA for both FAM and Cy5. Both Cy5 and FAM exhibit single exponential lifetime for the terminal or internal when the Au NP is absent. Comparison of the single and

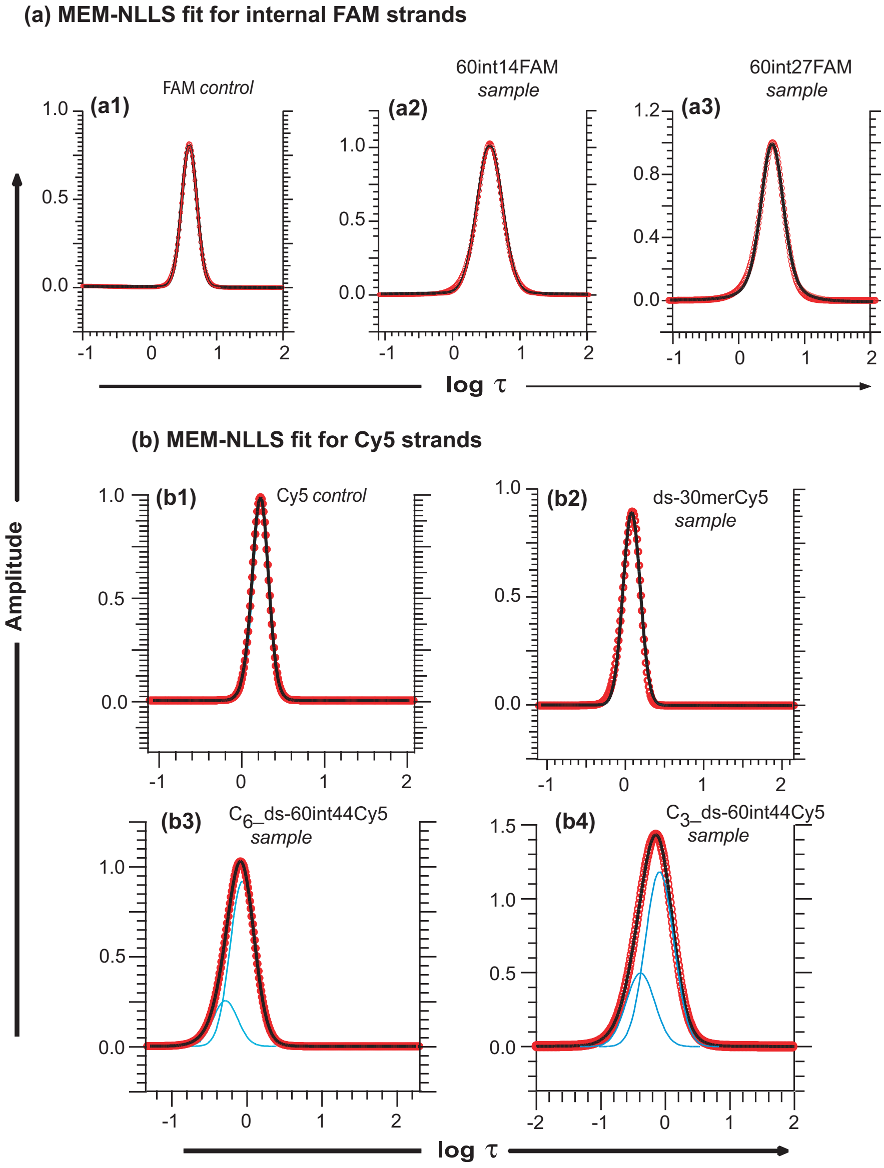

Figure 6.5: MEM-NLLS fit to (a)internal FAM strands and (b)Cy5 strands with (b2)terminal Cy5, (b3)internal C_6 Cy5 and (b4)internal C_3 Cy5.

bi-exponential fits by F-test indicates that a bi-exponential fit is statistically valid for the internal Cy5 *sample* strands with a very high value of the F ratio. The observation of a single-exponential lifetime for FAM is consistent with the literature observation that FAM is solvent exposed, exhibiting no intercalation along the DNA[145]. This also implies that the Au NP is not interacting with the DNA backbone or else a bi-

Table 6.1: A comparison of observed quantum yield (Φ_{obs}^{norm}), average lifetime (τ_{avg}), lifetime extracted from MEM-NLLS (τ_M), and Γ(FWHM), the width of MEM-NLLS peak for all the FAM and Cy5 labeled strands. The Φ_{obs}^{norm} is normalized to the control strand, where $\Phi_{FAM} = 0.9$ and $\Phi_{Cy5} = 0.25$

FAM

Strand	Control	60int14FAM	60int27FAM	60int38FAM	60int44FAM	60int54FAM	60int58FAM
Φ_{obs}^{norm}	1.00	1.00	0.78	0.42	0.28	0.16	0.14
τ_{avg} **(ns)**	3.38±0.06	3.33±0.12	2.78±0.09	1.65±0.14	1.09±0.03	-	-
τ_M **(ns)**	3.8±0.05	3.55±0.03	3.23±0.02	-	1.01±0.03	-	-
Γ	0.16±0.06	0.26±0.01	0.27±0.04	-	0.45±0.04	-	-

Cy5

Strand	**Control**	**60int19Cy5**	**60int27Cy5**	**60int34Cy5**	**60int38Cy5**	**$C_6$60int44Cy5**	**$C_3$60int44Cy5**
Φ_{obs}^{norm}	1.00	0.99	0.95	0.84	0.89	0.60	0.56
τ_M **(ns)**	1.66±0.02	1.66±0.05	1.47±0.03 0.94±0.05	1.30±0.07 0.87±0.07	1.45±0.05 0.11±0.05	0.86±0.04 0.51±0.05	0.97±0.05 0.47±0.04
Γ	0.14±0.03	0.14±0.05	0.22±0.03 0.12±0.05	0.19±0.07 0.17±0.07	0.23±0.05 0.16±0.05	0.23±0.04 0.14±0.05	0.20±0.03 0.19±0.04

Table 6.2: A comparison of the theoretically calculated distance (d_{theory}) ($d = a = 15$Å) with the experimentally measured distance by steady state measurement (E(I)) (d_I), average lifetime measurement (E(τ_{avg})) ($d_{\tau_{avg}}$) and the MEM-NLLS extracted distances (d_{τ_M}). The distances shown assume a fully extended C_6 spacer with FAM not intercalated but Cy5 in an average position or for the discrete solvent exposed and intercalated distances based on literature precedence.

FAM

Strand	Control	60int14FAM	60int27FAM	60int38FAM	60int44FAM	60int54FAM	60int58FAM
d_{theory} **(Å)**	-	170.6	125.4	89.1	70.3	26.8	16.5
d_I **(Å)**	-	-	122.1	81.6	64.0	43.5	41.9
$d_{\tau_{avg}}$ **(Å)**	-	-	124.1	83.9	70.6	-	-
d_{τ_M} **(Å)**	-	172.7	126.6	-	71.9	-	-

Cy5

Strand	**Control**	**60int19Cy5**	**60int27Cy5**	**60int34Cy5**	**60int38Cy5**	**$C_6$60int44Cy5**	**$C_3$60int44Cy5**
d_{theory} **(Å)**	-	156.1 152.4	129.4 80.1	117.3 74.6	109.1 70.1	70.4 52.9	66.7 49.1
d_I **(Å)**	-	158.0	133.3	98.4	109.1	72.9	69.8
d_M **(Å)**	-	155.2	130.1 76.7	120.4 68.4	112.1 66.0	68.9 54.1	71.1 52.2

exponential lifetime for internal FAM and a four component lifetime would have been observed for internal Cy5 strand. The bi-exponential lifetime over all experimental distances for internally appended Cy5 suggests two discrete sites of occupation for Cy5 along the DNA backbone, particularly since in the absence of a Au NP acceptor a single exponential is observed.

If we assume the two component lifetimes observed in the internal Cy5 data reflect two discrete occupation sites associated with intercalated and free rotor positions with respect to the DNA, then the ratio of intercalated to free rotor can be directly extracted. From the pre-exponential factors, which represent the intensity (or fractional composition of the bi-exponential) at t=0, the ratio of short lifetime to the long lifetime component (analogous to intercalated and free rotor) yield a value of 37% of the Cy5 donors are intercalated (short lifetime) for all DNA D-A separation distances on the internal C_6 sequence. The complete steady state intensity and lifetime (τ) data are compiled in Table 1.

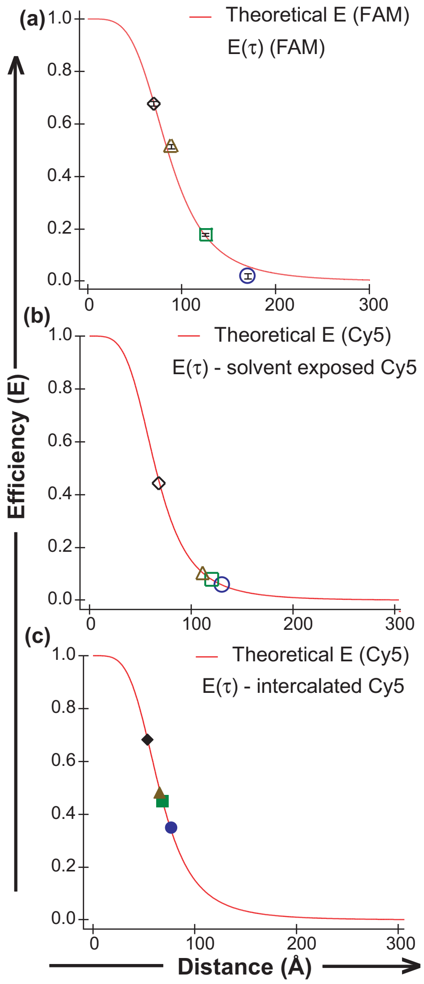

Figure 6.6: Comparison of the theoretical efficiency with the steady-state and τ_{avg} efficiency values for internally labeled (a)FAM, (b)Cy5 when it is solvent exposed and (c)Cy5 when it is intercalated in the DNA duplex.

To extract the discrete distances (R and R') that correlate with the two occupation sites for the D-A along the DNA, and gain insight into the dynamics of the two conformational states in the internally Cy5 labeled DNA, a plot of the theoretical NSET efficiency curve calculted from the empirically fit NSET theory (equation 5.3) with the experimental data points for the individual lifetime components for FAM and Cy5 from Table 5.1 are shown in Figure 6.6. The theoretical and the experimentally measured distances from the steady state intensity and lifetime analyzed data is shown

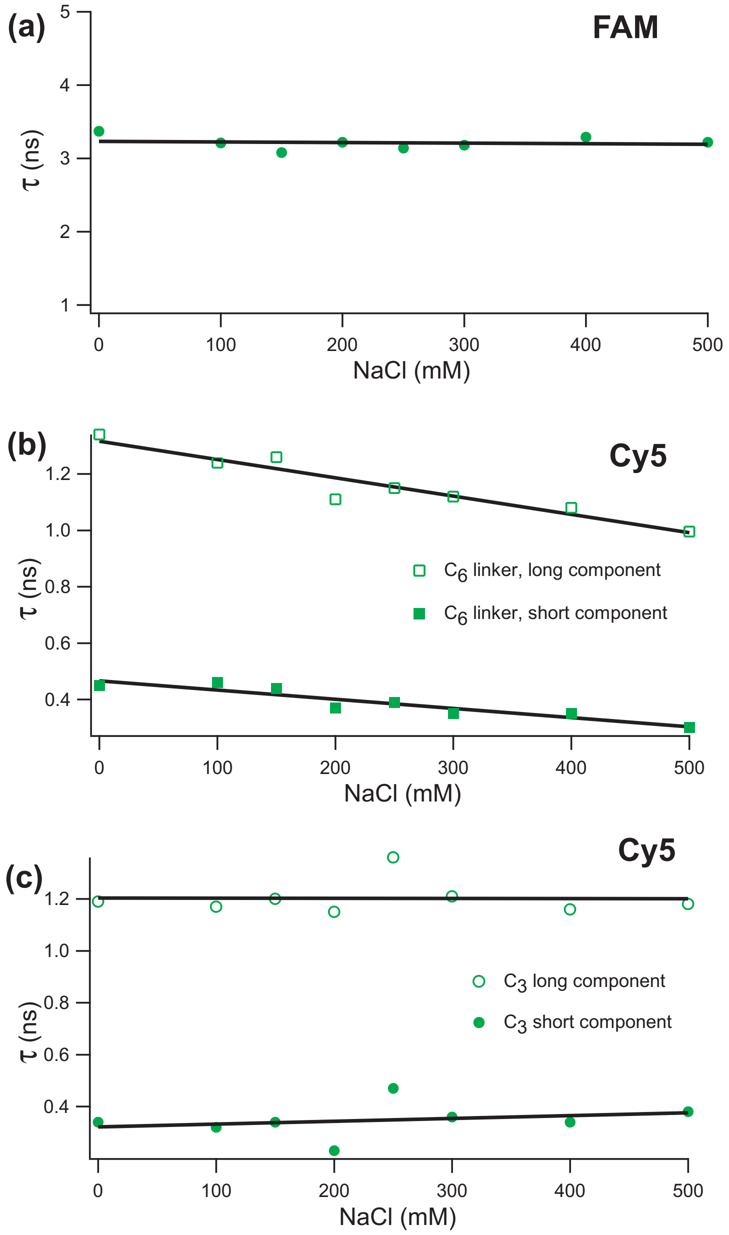

Figure 6.7: Effect of [NaCl] on the lifetime of internally labeled (a)FAM, (b)Cy5 appended through a C_6 linker and (c)Cy5 appended through a C_3

in Table 5.2. Inspection of Table 5.2, indicates the intensity data and lifetime for FAM are in good agreement with the theoretically predicted distances calculated using the Clegg model for a solvent exposed dye thus confirming a single exponential fit. The internal Cy5 steady state intensity data on the other hand is in poor agreement for a single site occupation based upon the theoretical prediction for either solvent exposed or intercalated positions of the Cy5, thus implying a 2-site occupation model is more accurate. The MEMS-NLLS extracted experimental lifetime data produce two independent lifetimes that are in good agreement with the theoretical prediction for these two independent occupation sites. The better agreement for lifetime data is not surprising, as lifetime based energy transfer experiments are more precise than steady state measurements[16].

In order to test whether the ratio of intercalated to solvent exposed for internal Cy5 is impacted by electrostatic contributions, we analyzed the change in the lifetime distribution for C_6-60int38FAM and C_6-60int44Cy5 as a function of [NaCl] over a range 0-500 mM in 20 mM PBS buffer, pH 7.5 (Figure 6.7). The sequences were intentionally chosen to be close to the R_0 value in order to have the highest sensitivity to changes in the population of the unique conformations as the NaCl concentration is varied. In the experimental lifetime for FAM, no dependence on salt concentration is observed consistent with its solvent exposed state. For the Cy5 system, a slight dependence of the lifetime values for both the exposed and intercalated dye is observed. However, no change in the population (pre-exponential values) between the two states is observed, suggesting the ratio of intercalated to solvent exposed is constant and has not been significantly impacted. No salt dependence is observed for the shorter linker, most likely arising from the tighter association of the Cy5 to the poly-anionic backbone of the DNA duplex. The larger slope change in the solvent exposed data implies that at the higher salt concentrations increased electrostatics may play a role in the interaction of Cy5 with the DNA, as might be expected for the positively charged dye; however, the increased association appears only to impact the magnitude of the free rotor approximation (cone of probability, Figure 6.1b) and not the population statistics for the individual conformations. The results support a dependence on linker length at the site of attachment for Cy5 intercalated with DNA. The longer spacer length (C_6) appears to reduce the contribution of intercalated *vs.* solvent exposed (37% for C_6 *vs.* 42% for C_3). The reduction in intercalation most likely reflects the reduced electrostatic interactions and greater degree of freedom in the C_6 spacer. Perturbation of the population statistics can also be observed if the linker length is decreased. By decreasing the linker length on the Cy5, the impact on the population statistics can be assessed. In Figures 6.4 and 6.5, the experimental lifetime data nad a MEM-NLLS fit for C_3-60int44cy5 is shown. Analysis of the lifetime indicates the population of intercalated to solvent exposed increases to a value of 42% (intercalated).

6.4 Conclusions

The strong agreement between the theoretical and experimental data in Cy5 over all length scales, linker lengths, and salt concentrations allows the Cy5 ratio of intercalated to solvent exposed positions on ds-DNA to be conclusively defined using NSET optical methods. Terminal appendage of Cy5 allows the free rotor approximation to be used while an internal appendage results in a percentage of the dye interacting with the ds-DNA. The results support the earlier findings on FRET pairs with Cy5 suggesting an equilibrium exists between defined intercalated and solvent exposed sites. The agreement between the theoretical distances and experimentally determined ones strongly suggests the equilibrium is static on the experimental time scale, as if a dynamic exchange is occurring it must be occurring on a substantially faster timescale than the shortest measured lifetime in the experiment. NSET produces a toolbox for testing the potential interactions of the biomolecules of interest. These results allow FRET experiments to be more accurately interpreted since the equilibrium can be precisely described.

BIBLIOGRAPHY

[1] Selvin, P. R. *Nat. Struct. Biol.* **2000,** *7,* 730-734.

[2] Clapp, A. R.; Medintz, I. L.; Mattoussi, H. *ChemPhysChem* **2006,** *7,* 47-57.

[3] Lakowicz, J. R. *Principles of FLuorescence Spectroscopy* , **2006,** *Springer Science, LLC.*

[4] Van der Meer, B. W.; Coker, G.; Chen, S. Y. S *Resonance Energy Transfer - Theory and Data* , **1994,** *VCH Publishers,Inc.*

[5] Stryer, L.; Haugland, R. P. *Proc. Nat. Acad. Sci.* **1967,** *58,* 719-725.

[6] Clapp, A. R.; Medintz, I. L.; Mauro, J. M.; Fisher, B. R.; Bawendi, M. G.; Mattoussi, H. *J. Am. Chem. Soc.* **2004,** *126,* 301-310.

[7] Eliseeva, S. V.; Bunzli, J. C. G. *Chem. Soc. Rev.* **2010,** *39,* 189-227.

[8] Selvin, P. R.; Hearst, J. E. *P. Natl. Acad. Sci.* **1994,** *91,* 10024-10028.

[9] Selvin, P. R. *Annu. Rev. Bioph. Biom.* **2002,** *31,* 275-302.

[10] Wingert, P. A.; Mizukami, H.; Ostafin, A. E. *Nanotech.* **2007,** *18,* 29570(7pp).

[11] Sapsford, K. E.; Berti, L.; Medintz, I. L *Angew. Chem. Int. Ed.* **2006,** *45,* 4562-4588.

[12] Pfleger, K. D. G.; Eidne, K. A. *Nature Methods* **2006,** *3,* 165-169.

[13] Pons, T.; Medintz, I. L.; Wang, X.; English, D. S.; Mattoussi, H. *J. Am. Chem. Soc.* **2006,** *128,* 15324-15331.

[14] Yasuda, R.; Masaike, T.; Adachi, K. *et. al. Proc. Nat. Acad. Sci.,* **2003,** *100,* 9314-9318.

[15] Yun, C. S.; Javier, A.; Jennings, T.; Fisher, M.; Hira, S.; Peterson, S.; Hopkins, B.; Reich, N. O.; Strouse, G. F. *J. Am. Chem. Soc.* **2005,** *127,* 3115-3119.

[16] Jennings, T. L.; Singh, M. P.; Strouse, G. F. *J. Am. Chem. Soc.* **2006,** *128,* 5462-5467.

[17] Singh, M. P.; Strouse, G. F. *J. Am. Chem. Soc.* **2010,** *132,* 9383-9391.

[18] Ha, T. *Methods* **2001,** *25,* 78-86.

[19] Weiss, S. *Nat. Struc. Biol.,* **2000,** *7,* 724-729.

[20] Jennings, T. L.; Schlatterer, J. C.; Singh, M. P.; Greenbaum, N. L.; Strouse, G. F. *Nano Lett.* **2006,** *6,* 1318-1324.

[21] Medintz, I. L.; Mattoussi, H. *Phys. Chem. Chem. Phys.* **2009,** *11,* 17-45.

[22] Fisher, B. R.; Eisler, H. J.; Scott, N. E; Bawendi, M. G. *J. Phys. Chem. B* **2004,** *108,* 143-148.

[23] Kim, S.; Lim, Y. T.; Soltesz, E. G. *et.al. Nat. Biotech.* **2004,** *22,* 93-97.

[24] Stroh, M.; Zimmer, J. P.; Duda, D. G.; *et.al. Nat. Med.* **2005,** *11,* 678-682.

[25] Geissler, D.; Charbonniere, L. J.; Ziessel, R. F; Loehmannsroeben, H. G.; Hilderbrandt, N. *Angew. Chem. Int. Ed.* **2010,** *49,* 1396-1401.

[26] Bruchez, M.; Moronne, M.; Bentolila, L. A.; Tsay, J. M.; Li, J. J.; Sundaresan, G.; Wu, A. M.; Gambhir, S. S.; Weiss, S. *Science* **2005,** *307,* 538-544.

[27] Fan, C.; Wang, S.; Hong, J. W.; Bazan, G. C.; Plaxco, K. W.; Heeger, A. J. *Proc. Nat. Acad. Sci.* **2003,** *100,* 6297-6301.

[28] Pons, T.; Medintz, I. L.; Sapsford, K. E.; Higashiya, S.; Grimes, A. F.; English, D. S.; Mattoussi, H. *Nano Lett.* **2007,** *7,* 3157-3164.

[29] Sen, T.; Sadhu, S.; Patra, A. *App. Phys. Lett.* **2007,** *91,* 043104(1)-043104(3).

[30] Darbha, G. K; Ray, A.; Ray, P. C. *ACS Nano* **2007,** *2,* 77-84.

[31] Sen, T.; Patra, A. *J. Phys. Chem. C* **2008,** *112,* 3216-3222.

[32] Haldar, K. K; Patra, A. *Chem. Phys. Lett.* **2008,** *462,* 88-91.

[33] Darbha, G. K.; Lee, E.; Anderson, Y. R.; Fowler, P.; Mitchell,K .; Ray, P. C. *IEEE Sensors J.* **2008,** *8,* 693-700.

[34] Huang, S. X; Chen, Y. *Nanolett.* **2008,** *8,* 2829-2833.

[35] Griffin, J.; Ray, P. C; *J. Phys. Chem. B* **2008,** *112,* 11198-11201.

[36] Sen, T.; Haldar, K. K; Patra, A. *J. Phys. Chem. C* **2008,** *112,* 17945-17951.

[37] Kogot, J. M.; England, H. J.; Strouse, G. F.; Logan, T. M. *J. Am. Chem. Soc.* **2008,** *130,* 16156-16157.

[38] Griffin, J.; Singh, A. K.; Senapati, D.; Rhodes, P.; Mitchell, K.; Robinson, B.; Yu, E.; Ray, P. C. *Chemistry - Euro. J.* **2009,** *15,* 342-351.

[39] Chhabra, R.; Sharma, J.; Wang, H. N.; Zou, S. L.; Lin, S.; Yan, H.; Lindsay, S.; Liu, Y. *Nanotech.* **2009,** *20,* 485201(1)-485201(10).

[40] Kogot, J. M.; Parker, A. M.; Lee, J. Blaber, M.; Strouse, G. F.; Logan, T. M. *Bioconj. Chem.* **2009,** *20,* 2106-2113.

[41] Sen, T.; Jana, S.; Koner, S.; Patra, A. *J. Phys. Chem. C* **2010,** *114,* 707-714.

[42] Kagan, C. R.; Murray, C. B. Nirmal, M.; Bawendi, M. G. *Phys. Rev. Lett.* **1996,** *76,* 1517-1520.

[43] Michalet, X.; Pinaud, F. F.; Gin, P.; Weiss, S.; Alivisatos, A. P. *Science* **1998,** *281,* 2013-2016.

[44] Chan, W. C. W.; Nie, S. *Science* **1998,** *281,* 2016-2018.

[45] Clapp, A. R.; Medintz, I. L.; Fisher, B. R.; Anderson, G. P.; Mattoussi, H. *J. Am. Chem. Soc.* **2005,** *127,* 1242-1250.

[46] Charbonniere, L. J.; Hilderbrandt, N. Ziessel, R. F; Loehmannsroeben, H. G.; *J. Am. Chem. Soc.* **2006,** *128,* 12800-12809.

[47] Hilderbrandt, N.; Charbonniere, L. J.; Beck, M.; Ziessel, R. F; Loehmannsroeben, H. G.; *Angew. Chem. Int. Ed.* **2005,** *44,* 7612-7615.

[48] Kuhn, H. *J. Chem. Phys.* **1970,** *53,* 101-108.

[49] Rosi, N. L.; Mirkin, C. A. *Chem. Rev.* **2005,** *105,* 1547-1562.

[50] Hayat, M. A. *Colloidal Gold: Principles, Methods and Applications* vol. 1 **1989,** *Academic Press, Inc.*

[51] Sardar, R.; Funston, A. M.; Mulavaney, P.; Murray, R. W *Langmuir* **2009,** *25,* 13840-13851.

[52] Borisov, S. M.; Wolfbeis, S. M. *Chem. Rev.* **2008,** *108,* 423-461.

[53] Daniel, M. C.; Astruc, D. *Chem. Rev.* **2004,** *104,* 293-346.

[54] Giljohann, D. A.; Seferos, D. S.; Daniel, W. L; Massich, M. D; Patel, P. C.; Mirkin, C. A. *Angew. Chemie-Intl. Ed.* **2010,** *49,* 3280-3294.

[55] Huang, X. H.; Neretina, S.; El-Sayed, M. A. *Adv. Mater.* **2009,** *21,* 4880-4910.

[56] Lakowicz, J. R. *Anal. Biochem.* **2005,** *337,* 171-194.

[57] Zhang, J.; Lakowicz, J. R. *Opt. Exp.* **2007,** *15,* 2598-2606.

[58] Bene, L.; Szentesi, G.; Matyus, L.; Gaspar, R.; Damjanovich, S. *J. Mol. Recog.* **2005,** *18,* 236-253.

[59] Gersten, J.; Nitzan, A. *J. Chem. Phys.* **1981,** *75,* 1139-1152.

[60] Dulkeith, E.; Ringler, M.; Klar, T. A.; Feldman, J. Javier, A. M.; Parak, W. J.; *Nano Lett.* **2005,** *5,* 585-589.

[61] Dubertret, B.; Calame, M.; Libchaber, A. J. *Nat. Biotech.* **2001,** *19,* 365-370.

[62] Kreibig, U.; Vollmer, M. *Optical Properties of Metal Clusters* , **1995,** *Springer-Verlag 25.*

[63] Alvarez, M. M.; Khoury, J. T.; Schaaff, T. G.; Shafigullin, M. N.; Vezmar, I.; Whetten, R. L. *J. Phys. Chem. B* **1997,** *101,* 3706-3712.

[64] Wooten, F. *Optical Properties of Solids* **1972,** *Academic Press,Inc.*

[65] Chance, R. R.; Prock, A.; Silbey, R. *J. Chem. Phys.* **1975,** *62,* 2245-2253.

[66] Chance, R. R.; Prock, A.; Silbey, R. *Adv. Chem. Phys.* **1978,** *37,* 1-65.

[67] Persson, B. N. J.; Lang, N. D. *Phys. Rev. B* **1982,** *26,* 5409-5415.

[68] Zheng, J.; Zhang, C. W.; Dickson, R. M. *Phys. Rev. Lett.* **2004,** *93,* 077421-077424.

[69] Link, S.; El-Sayed, M. A. *Int. Rev. Phys. Chem.* **2000,** *19,* 409-453.

[70] Encina, E. R.; Coronado, E. A. *J. Phys. Chem. C* , **2007,** *111,* 16796-16801.

[71] Jain, P. K.; Lee, K. S.; El-Sayed, I. H.; El-Sayed, M. A. *J. Phys. Chem. B* **2006,** *110,* 7238-7248.

[72] Abeles, F. *Optical Properties of Solids* , **1972,** *North-Holland Publishing Co.*

[73] Turro, N. J. *Modern Molecular Photochemistry* **1978,** *Benjamin/Cummings Pub.Co., Inc.*

[74] Inacker, O.; Kuhn, H. *Chem. Phys. Lett.* **1974,** *27,* 317-321.

[75] Hovel, H.; Fritz, S.; Hilger, A.; Kreibig, U.; Vollmer, M. *Phys. Rev. B* **1993,** *48,* 18178-18188.

[76] Stryer, L. *Biochemistry* , **1995,** *W. H. Freeman Co.*

[77] Hagerman, P. J. *Annu. Rev. Biophys. Bio.* **1988,** *17,* 265-286.

[78] Mathew-Fenn, R. S.; Das, R.; Harbury, P. A. B. *Science* **2008,** *322,* 446-449.

[79] Clegg, R. M.; Murchie, A. I. H.; Zechel, A.; Lilley, D. M. J. *P. Natl. Acad. Sci.* **1993,** *90,* 2994-2998.

[80] Armitage, B. A. *Top. Curr. Chem.* **2005,** *253,* 55-76.

[81] Ruppin, R. *J. Chem. Phys.* **1982,** *76,* 1681-1684.

[82] Dulkeith, E.; Morteani, A. C.; Neidereichholz, T.; Klar, T. A.; Feldman, J.; Levi, S. A.; van Veggel, F. C. J. M.; Reinhoudt, D. N.; Moller, M.; Gittins, D. I. *Phys. Rev. Lett.* **2002,** *89,* 203002-1.

[83] Worthing, P. T.; Amos, R. M.; Barnes, W. L. *Phys. Rev. A* **1999,** *59,* 865-872.

[84] Kalkman, J.; Kuipers, L.; Polman, A.; Gersen, H. *App. Phys. Lett.* **2005,** *86,* 041113(1)-041113(3).

[85] Weare, W. W.; Reed, S. M. Warner, M. G. Hutchison, J. E. *J. Am. Chem. Soc.* **2000,** *122,* 12890-12891.

[86] Chang, R. L. *Opt. Comm.* **2005,** *249,* 329-337.

[87] Leung, P. T. *Phys. Rev. B* **1990,** *42,* 7622-7625.

[88] Sandorfy, C. *Electronic Spectra and Quantum Chemistry* , **1964,** *Prentice-Hall,Inc.*

[89] Alivisatos, A. P.; Waldeck, D. H.; Harris, C. B. *J. Chem. Phys.* **1985,** *82,* 541-547.

[90] Johnson, P. B.; Christy, R. W. *Phys. Rev. B* **1972,** *6,* 4370-4379.

[91] Kreibig, U.; Genzel, L. *Surf. Sci.* **1985,** *156,* 678-700.

[92] Link, S.; El-Sayed, M. A. *J. Phys. Chem. B* **1999,** *103,* 8410-8426.

[93] Jennings, T. L.; Strouse, G. F. *Advances in Experimental Medicine and Biology* **2007,** *620,* 34-47.

[94] Drexhage, K. H. *J. Luminesc.* **1970,** *1.2,* 693-701.

[95] Jensen, T.; Kelly, L.; Lazarides, A.; Schatz, G. C. *J. Cluster Sci.* **1999,** *10,* 295-317.

[96] Swathi, R. S.; Sebastian, K. L. *J. Chem. Phys.* **2007,** *126,* 234701(1)-234701(5).

[97] Singh, M. P.; Jennings, T. L.; Strouse, G. F. *J. Phys. Chem. B* **2001,** *113,* 552-558.

[98] Munoz-Losa, A.; Vukovic, S.; Corni, S.; Mennucci, B. *J. Phys. Chem. C* **2009,** *113,* 16364-16370.

[99] Hovel, H.; Fritz, S.; Hilger, A.; Kreibig, U. *Phys. Rev. B* **1993,** *48,* 18178-18188.

[100] Brewer, S. H.; Glomm, W. R.; Johnson, M. C.; Knag, M. K.; Franzen, S. *Langmuir* **2005,** *21,* 9303-9307.

[101] Asuri, P.; Bale, S. S.; Karajanagi, S. S.; Kane, R. S. *Curr. Opin. Biotech.* **2006,** *17,* 562-568.

[102] Yun, C. S.; Khitrov, G. A.; Vergona, D. E.; Reich, N. O.; Strouse, G. F. *J. Am. Chem. Soc.* **2002,** *124,* 7644-7645.

[103] Anker, J. N.; Hall, W. P.; Lyandres, O.; Shah, N. C; Zhao, J.; van Duyne, R. D. *Nat. Mater.* **2008,** *7,* 442-453.

[104] Chew, H. *J. Chem. Phys.* **1987,** *87,* 1355-1360.

[105] Wiederrecht, G. P.; Wurtz, G. A.; Hranisavljevic, J. *Nano. Lett.* **2004,** *4,* 2121-2125.

[106] Chen, Y.; Munechika, K.; Ginger, D. S. *Nano Lett.* **2007,** *7,* 690-696.

[107] Stiles, P. L.; Dieringer, J. A.; Shah, N. C.; van Duyne, R. R. *Ann. Rev. Anal. Chem.* **2008,** *1,* 601-626.

[108] Haes, A. J.; Zou, S. L.; Zhao, J.; Schatz, G. C.; van Duyne, R. R. *J. Am. Chem. Soc.* **2006,** *128,* 10905-10914.

[109] Das, P.; Metiu, H. *J. Phys. Chem.* **1985,** *89,* 4680-4687.

[110] Larsen, R. E.; Metiu, H. *J. Chem. Phys.* **2001,** *114,* 6851-6860.

[111] Pinchuk, A.; Plessen, G.; Kreibig, U. *J. Phys. D:Appl. Phys.* **2004,** *37,* 3133-3139.

[112] Malicki, M.; Hales, J. M.; Rumi, M.; Barlow, S. McClary, L.; Marder, S. R.; Perry, J. W. *Phys. Chem. Chem. Phys.,* **2010,** *12,* 6267-6277.

[113] Kometani, N.; Tsubonishi, M.; Fujita, T. Asami, K.; Yonezawa, G. F.; Logan, Y. *Langmuir* **2001,** *17,* 578-580.

[114] Thomas, K. G.; Kamat, P. V. *Acc. Chem. Res.,* **2003,** *36,* 888-898.

[115] Smith, B. A.; Zhang, J. Z.; Giebel, U.; Schmid, G. *Chem. Phys. Lett.* **1997,** *270,* 139-144.

[116] Jin, R. C.; Wu, G. S.; Li, Z. Mirkin, C. A.; Schatz, G. C. *J. Am. Chem. Soc.* **2003,** *125,* 1643-1654.

[117] Storhoff, J. J.; Lazarides, A. A.; Mucic, R. C.; Mirkin, C. A.; Letsinger, R. L.; Schatz, G. C. *J. Am. Chem. Soc.* **2000,** *122,* 4640-4650.

[118] Georganopoulou, D. G.; Chang, L.; Nam, J. M.; Thaxton, C. S.; Mufson, E. J.; Klein, W. L.; Mirkin, C. A. *PNAS* **2005,** *102,* 2273-2276.

[119] Sonnichsen, C.; Reinhard, B. M.; Liphard, J.; Alivisatos, A. P. *Nat. Biotech.* **2005,** *23,* 741-745.

[120] Fleischmann, M.; Hendra, P. J.; Mcquillan, A. J. *Chem. Phys. Lett.* **1974,** *26,* 163-166.

[121] Krasser, W.; Kettler, U.; Bechthold, P. S. *Chem. Phys. Lett.* **1982,** *86,* 223-227.

[122] Talley, C. E.; Jackson, J. B.; Oubre, C.; Grady, N. K.; Hollars, C. W.; Lane, S. M.; Huser, T. R.; Nordlander, P.; Halas, N. J. *NanoLett.* **2005,** *5,* 1569-1574.

[123] Laurent, G.; Felidj, N.; Truong, S. L. Aubard, J.; Levi, G.; Krenn, J. R.; Hohenau, A.; Leitner, A.; Aussenegg, F. R. *NanoLett.* **2005,** *5,* 253-258.

[124] Kho, K. W.; Shen, Z. X.; Zeng, H. C.; Soo, K. C.; Olivo, M. *Anal. Chem.* **2005,** *77,* 7462-7471.

[125] Kim, K.; Lee, H. S. *J. Phys. Chem. B* **2005,** *109,* 18929-18934.

[126] Moskovits, M. *Rev. Mod. Phys.* **1985,** *57,* 783-826.

[127] Zhang, J.; Lakowicz, J. R. *J. Phys. Chem. B* **2005,** *109,* 8701-8706.

[128] Malicka, J.; Gryczynski, I.; Gryczynski, Z.; Lakowicz, J. R. *Anal. Biochem.* **2003,** *315,* 57-66.

[129] Malicka, J.; Gryczynski, I.; Gryczynski, Z.; Lakowicz, J. R. *Biopolymers* **2004,** *74,* 263-271.

[130] Aslan, K.; Gryczynski, I.; Malicka, J.; Matveeva, E.; Lakowicz, J. R. Geddes, C. D. *Curr. Op. Biotech.* **2005,** *16,* 55-62.

[131] Franzen, S.; Folmer, J. C. W.; Glomm, W. R.; O'Neal, R. *J. Phys. Chem. A* **2002,** *106,* 6533-6540.

[132] Jares-Erijman, E. A.; Jovin, T. M. *J. Mol. Biol.* **1996,** *257,* 597-617.

[133] Dietrich, A.; Buschmann, V.; Muller, C.; Sauer, M. *Rev. Molec. Biotech.* **2002,** *82,* 211-231.

[134] Weiss, S. *Science* **1999,** *283,* 1676-1683.

[135] Hohng, S.; Joo, C.; Ha, T. *Biophys. J.* **2004,** *87,* 1328-1337.

[136] Murphy, M. C.; Rasnik, I.; Cheng, W.; Lohman, T. M.; Ha, T. J. *Biophys. J.* **2004,** *86,* 2530-2537.

[137] Mahtab, R.; Harden, H. H. Murphy, C. J. *J. Am. Chem. Soc.* **2000,** *122,* 14-17.

[138] You, C. C.; De, M.; Rotello, V. M. *Curr. Opin. Chem. Biol.* **2005,** *9,* 639-646.

[139] Mahtab, R.; Sealey, S. M.; Hunyadi, S. E.; Kinard, B.; Ray, T.; Murphy, C. J. *J. Inorg. Biochem.* **2007,** *101,* 559-564.

[140] You, C. C.; Chompoosor, A.; Rotello, V. M. *Nano Today* **2007,** *2,* 34-43.

[141] Norman, D. G.; Grainger, R. J.; Uhrin, D.; Lilley, D. M. J. *Biochemistry* **2000,** *39,* 6317-6324.

[142] Karlsson, H. J.; Eriksson, M.; Perzon, E.; Akerman, B.; Lincoln, P.; Westman, G. *Nucl. Acids Res.* **2003,** *31,* 6227-6234.

[143] Eriksson, M.; Karlsson, H. J.; Westman, G.; Akerman, B. *Nucl. Acids Res.* **2003,** *31,* 6235-6242.

[144] Biver, J.; De Biasi, A.; Secco, F.; Venturini, M.; Yarmoluk, S. *Biophys. J.* **2005,** *89,* 374-383.

[145] Massey, M.; Algar, W. R.; Krull, U. J. *Anal. Chim. Acta* **2006,** *568,* 181-189.

[146] Steinbach, P. J.; Ionescu, R.; Matthews, C. R. *Biophys. J.* **2002,** *82,* 2244-2255.

[147] Steinbach, P. J. *J. Chem. Info. Comp. Sci.* **2002,** *42,* 1476-1478.

[148] Kim, J.; Lee, M. *Biochem. Biophys. Res. Comm.* **2004,** *316,* 393-397.

[149] Lorenz-Fonfria, V . A.; Kandori, H. *Appl. Spec.* **2006,** *60,* 407-417.

[150] Zhou, Y. Zhuang, X. *Biophys. J.* **2006,** *91,* 4045-4053.

[151] Dolghih, E.; Roitberg, A. E.; Krause, J. L. *J. Photochem. Photobiol. A-Chem.* **2007,** *190,* 321-327.

[152] Deniz, A. A.; Dahan, M.; Grunwell, J. R.; Ha, T. J.; Faulhaber, A. E.; Chemla, D. S.; Weiss, S.; Schultz, P. G. *P. Natl. Acad. Sci. USA* **1999,** *96,* 3670-3675.

[153] Griffin, J.; Ray, P. C. *J. Phys. Chem. C* **2008,** *112,* 11198-11201.

[154] Liu, C. W.; Huang, C. C.; Chang, H. T. *Langmuir* **2008,** *24,* 8346-8350.

[155] Sen, T.; Patra, A. *J. Phys. Chem. C* **2008,** *112,* 3216-3222.

[156] Darbha, G. K.; Ray, A; Ray, P. C. *ACS Nano* **2007,** *1,* 208-214.

[157] Campion, A.; Gallo, A. R.; Harris, C. B.; Robota, H. J.; Whitmore, P. M. *Chem. Phys. Lett.* **1980,** *73,* 447-450.

[158] Millington, M.; Grindlay, G. J; Altenbach, K.; *et.al. Biophysical Chemistry* **2007,** *127,* 155-164.

[159] Yasuda, R. *Curr. Opi. Neurobiol.* **2006,** *16,* 551-561.

BIOGRAPHICAL SKETCH

Education

Ph.D., Chemistry (Physical- Inorganic), Florida State University, Tallahassee, FL
Ph.D. Thesis: *Energy Transfer in Bio-molecules-Mechanism, Validity and Applicability of Nano-metal Surface Energy Transfer (NSET)*
Fall 2010

Master of Science, Chemistry, Indian Institute of Technology Delhi, New Delhi, India
Research: *Synthesis of Perovskites by Solid State Route-Dielectric, Electrical and Magnetic Properties*
April 2004

Bachelor of Science, Chemistry (Honors) Hindu College, University of Delhi, India
April 2002

Appointments

Technical Appointment - NMR Technician, Analyst, Training In-charge (Varian 300MHz and 600MHz, Bruker 400MHz and 500MHz)

Teaching Assistant - General Chemistry CHM1045L, Inorganic Chemistry CHM4610L

Research Assistant - NIH funded research on NSET

Research Experience and Technical Expertise

Biomaterials - Integration of metal nanoparticles, QD, Organic dyes with oligonucleotides (DNA/RNA) Purification (Gel electrophoresis and Ethanol precipitation).

Metal Nanoparticles (Au, Ag and alloy) - Synthesis (One phase and biphasic routes), Characterization (UV-Vis, XRF, TEM), Purification (Gel Electrophoresis).

Enzyme Activity - Effect of metal nanoparticles on Nucleases and their activity.

Energy Transfer studies - FRET, NSET.

Optical Studies - UV-Visible Spectroscopy; Steady State Fluorescence Spectroscopy; Time Resolved Fluorescence Spectroscopy (picosecond timescale).

Doped Oxides - Synthesis by high solid state methods (high and low temperature) and flux method; Characterization by XRD, SEM; Magnetic studies by PPMS; Density measurements; Conductance measurement; Dielectric measurements.

Optical Spectroscopy - UV-Visible and temperature dependent Fluorescence spectroscopy

Picosecond Laser Spectroscopy - Time resolved optical and near-IR spectroscopy

Electrophoresis - PAGE and Agarose

NMR - Varian 300MHz,600MHz (variable temperature) and Bruker 400MHz,500MHz

pXRD - Purity and Phase characterization

Other Instruments and Techniques - Lyophilization, Cyclic Voltammetry, HPLC, XRF, TEM, SEM, IR spectroscopy, Mathematica

Publications

1. 'NSET molecular beacon analysis of hammerhead RNA substrate binding and catalysis' Jennings, T.L.; Schlatterer, J.C.; Singh, M.P.;, Greenbaum, N.L.; Strouse, G.F.; *Nano Lett.*, **6** (*2006*) 1318-1324.

2. 'Fluorescent lifetime quenching near a d=1.5nm gold nanoparticles: Probing NSET validity' Jennings, T.L.; Singh, M.P.; Strouse, G.F.; *J.Am.Chem.Soc.*, **128** (*2006*), 5462-5467.

3. 'Tracking spatial disorder in an optical ruler using time-resolved NSET' Singh, M.P.; Jennings, T.L.; Strouse, G.F.; *J. Phys. Chem. B*, **113** (*2009*) 552-558.

4. 'Involvement of the lSPR Spectral Overlap for Energy Transfer between a Dye and Au Nanoparticle' Singh, M.P.; Strouse GF; *J.Am.Chem.Soc.* **132** (*2010*) 9383-9391.

5. 'C-Lysine Conjugates: pH-Controlled Light-Activated Reagents for Efficient Double-Stranded DNA Cleavage with Implications for Cancer Therapy' Yang, W.Y.; Breiner, B.;, Kovalenko, S.V.;, Ben ,C.; Singh, M.;, LeGrand, S.N.; Sang, Q-X.A .; Strouse, G.F.; Copland, J.A.; Alabugin, I.V.; *J.Am.Chem.Soc.*, **131** (*2009*), 11458-11470.

6. 'Impact of Size of a Metal Nanoparticle on the Energy Transfer Process' Singh, M.P.; Strouse, G.F.; (*J.Am.Chem.Soc.* Pending)

7. 'Fluorescence Queching by $d \rightarrow sp$ Interband Levels in 2nm Gold nanometals' Singh, M.P.; Strouse, G.F. (*Nano Lett.* Submitted)

8. 'Effect of Metal Nanoparticles on the Activity of ECoR1' Singh, M.P.; Yun, C.S.; Strouse, G.F.;(*Biocon.Chem.* Pending)

Presentations

1. ‘Nano-material molecular rulers: Probing distance and orientation in dye labeled bio-molecules’ Singh, M.P.; Strouse, G.F.; Jennings, T.L. *MRS Spring 2006.*

2. ‘Nano-material molecular rulers: Probing distance and orientation in dye labeled bio-molecules’ Singh, M.P.; Strouse, G.F.; Jennings, T.L. *FAME Summer 2006.*

3. ‘A maximum entropy-nonlinear least squares analysis on ds-DNA based Optical molecular rulers’ Singh, M.P.; Strouse, G.F. *MRS Spring 2007.*